

THE DISRUPTION OF BINARY STAR SYSTEMS
BY MASSIVE BLACK HOLES AND THE
RESTRICTED 3-BODY PROBLEM.

Harriet Brown

A thesis submitted in partial fulfilment of the requirements of
Liverpool John Moores University
for the degree of
Doctor of Philosophy.

June, 2019

Declaration

The work presented in this thesis was carried out at the Astrophysics Research Institute, Liverpool John Moores University. Unless otherwise stated, it is the original work of the author.

While registered as a candidate for the degree of Doctor of Philosophy, for which submission is now made, the author has not been registered as a candidate for any other award. This thesis has not been submitted in whole, or in part, for any other degree.

Harriet Brown
Astrophysics Research Institute
Liverpool John Moores University
IC2, Liverpool Science Park
146 Brownlow Hill
Liverpool
L3 5RF
UK

TUESDAY 11TH JUNE, 2019

Abstract

Hyper-velocity stars are stars that have been accelerated to speeds in excess of the escape velocity of the galaxy. The first hyper-velocity star observed was found in 2005 by Brown et al. (2005) and to date we can confirm 25 stars as being hyper-velocity. The small number of these stars discovered is due to the relatively low rate of acceleration events as well as observational methods limiting observations to B type stars. The leading processes by which these stars may be accelerated are binary tidal disruption events in the center of our galaxy. A binary tidal disruption event occurs when a binary star system orbits close to a massive compact object, such as a massive black hole. When this occurs the binary members are separated and one of the binary members gains the orbital energy of its partner, ejecting it at high speeds leaving the partner bound to the black hole. These bound stars, known as S-stars, have been observed and can be used to calculate the mass of the central massive black hole in our galaxy.

In this thesis, I present the result of a series of simulations of binary tidal disruption. These simulations provide insight into the required parameters to trigger a binary tidal disruption event as well as the properties of stars ejected via these events. My simulations utilize a restricted three body model to reduce the parameter space that I need to explore to simply the binary orientation, binary phase angle and the penetration depth D , that being the ratio of the closest distance the binary center of mass approaches to the black hole and the tidal radius. This approximation models binaries as having zero energy parabolic orbits but also allows me to model the binary orbit as radial for binaries that have orbits bringing them extremely close to the massive black hole.

I will firstly show how the disruption rate behaves as a function of the individual initial

conditions of the binary. As the penetration depth shrinks the majority of binaries will be disrupted, however as the penetration depth approaches zero there are still approximately 12% of binaries that survive their orbit around the black hole. The magnitude of velocity gained by the ejected stars is relatively independent of penetration depth with ejected stars having energies of the order of $E \approx (Gm^2/a)(M/m)^{1/3}$ where m is the mass of the binary, M is the black hole mass and a is the binary separation. Hyper-velocity stars seen in my simulations are only rarely ejected with energies greater or less than this order of magnitude. Because of this the distribution of binary properties (binary and black hole masses, and binary separation) is more important to the spectrum of hyper-velocity stars than the distribution of injection parameters (penetration depth, binary orientation binary phase, and eccentricity). While the average disruption rate can be well defined with penetration depth for a given orientation the disruption dependency is more complex with prograde orbits being favoured for disruption in shallow penetrations $D \approx 1 \sim 2$, while binaries oriented with their angular momentum vector toward the black hole are favored in deep penetrations $D \ll 1$.

Secondly I consider the disruption rate in terms of the binary phase at the periapsis of its orbit and attempt to constrain the critical criteria that determine the fate of the binary. By looking at binary disruption in terms of free solutions in the radial approximation I can approximate the range of binary phase angles that will survive their encounter with the black hole.

Thirdly I explore the properties of the former partners of hyper-velocity stars that remain bound to the black hole in terms of their eccentricity. I find that post disruption bound stars have eccentricities close to unity. This is significantly higher than observed S-stars in our galaxy, suggesting stars in the center of our galaxy have undergone relaxation over time.

Finally I discuss the implications of binary interactions for gravitational wave astronomy. Binaries that survive these orbits will have their own internal orbits shifted, gaining significant eccentricity and potentially having their semi-major axis changed. As surviving binaries have their orbits deformed, the inspiral time for binary compact objects can be decreased significantly.

HARRIET BROWN

TUESDAY 11TH JUNE, 2019

Publications

In the course of completing the work presented in this thesis, the following paper has been submitted for publication in a refereed journal:

Brown, H., Kobayashi, S., Rossi, E. M. & Sari, R.

2018. Tidal Disruption of Inclined or Eccentric Binaries by Massive Black Holes, *MNRAS*, 477:5682-5691.

Acknowledgements

I would like to thank my supervisor Shiho Kobayashi, this thesis would not have been possible without his experience and patience over the entity of my studies. I would also like to thank my fellow postgraduate students within the astrophysics research institute for their advice during difficult times. Additional thanks should also go out to advisors Nate Bastian and Matt Darnley who's advice helped me decide what I wanted out of this degree

This thesis would also not have been possible without the funding from the STFC and the LJMU faculty of engineering supporting me and allowing travel to multiple conferences and workshops.

A final personal thanks to the Young Persons Advisory Service for all the work they have done to provide a safe space for me to express myself, without which I would certainly have never completed my thesis

“I look inside myself and I ask: “Do I feel like a man or a woman?” and the answer is that I feel like shit”

- Natalie Parrott

“Build a man a fire, and he’s warm for a day. Set a man on fire and he’s warm for the rest of his life.”

- Terry Pratchett

“Listen. Strange women lying in ponds distributing swords is no basis for a system of government. Supreme executive power derives from a mandate from the masses, not from some farcical aquatic ceremony.”

- Michael Palin

Contents

Declaration	ii
Abstract	iii
Publications	vi
Acknowledgements	vii
Contents	ix
List of Tables	xii
List of Figures	xiii
1 Introduction	1
1.1 Sgr A*	1
1.2 Binary TDE studies	3
1.3 Observations	23
1.3.1 Hyper-Velocity Stars	23
1.3.2 S-Stars	28
2 Binary Exchange collision and the Restricted 3 Body Problem	30

2.1	Conditions required for an exchange collision	30
2.2	The Restricted 3 body problem	35
2.2.1	General Approximation	35
2.2.2	Radial Approximation	41
2.2.3	Free Solutions in the General Solution	42
2.2.4	The $t=0$ Singularity in the Radial solution	47
2.2.5	Time step scaling	50
2.3	Initial Conditions	54
2.3.1	General Case	54
2.3.2	Radial Case	61
2.3.3	Kozai-Lidov Mechanism	62
3	Numerical Simulations	65
3.1	Disruption Probability and Ejection Energy	65
3.1.1	Disruption Probability and energy with Penetration Depth	67
3.1.2	Disruption Probability and Energy with Orientation	74
3.1.3	Disruption Probability and Energy with Binary Phase	82
3.1.4	Deep Encounter Survivors	85
3.1.5	Disruption probability and energy with binary eccentricity	90
3.2	Bound Stars and the conditions of S-Stars	96
3.3	Surviving binaries	99
4	Conclusions and Discussion	105

List of Tables

- 1.1 Table of observed HVSSs. (1) Brown et al. (2005), (2) Edelmann et al. (2005) (3) Brown et al. (2006a) (4) Brown et al. (2006b), (5) Brown et al. (2007b), (6) Brown et al. (2009), (7) Brown et al. (2012), (8) Brown et al. (2014), (9) (Zheng et al., 2014) (10) Huang et al. (2017) . 27

List of Figures

1.1	The probability of an exchange collision as a function of penetration depth as found by Hills (1988). Penetration depth here is taken using Hills normalization $D_{min} \sim 80D$ and binary separation is given in units of AU. Figure is taken from Hills (1988)	5
1.2	The probability of an exchange collision as a function of the periastron distance of the binary orbit as found by Hills (1991) with different black hole mass in terms of the mass of one binary member (M_0) and binary velocity at infinity in terms of the binary internal velocity. Top left panel: black hole mass $10M_0$ with velocities $0.001 < V_\infty/V_{orbital} < 3.004$. Top right panel: black hole mass 10^2M_0 with velocities $0.001 < V_\infty/V_{orbital} < 3.754$. Bottom left panel: black hole mass 10^3M_0 with velocities $0.001 < V_\infty/V_{orbital} < 4.801$. Bottom right panel: black hole mass 10^4M_0 with velocities $0.001 < V_\infty/V_{orbital} < 9.011$. Figure taken from Hills (1991).	7
1.3	Distribution of ejection speeds immediately after disruption for a binary with $m_1 = 4M_\odot$, $M = 3.5 \times 10^6M_\odot$, $a = 0.1\text{AU}$, and $R_p = 5\text{AU}$. This orbit corresponds to a penetration depth of $D \approx 0.5$. Figure taken from Bromley et al. (2006).	12

1.4	Projection of the coordinates of observed HVSs and some structures in the Galactic centre, with open circles being stars with their coordinates centred on the earth and closed circles being the stars' coordinates centred in the Galactic centre. The curves show the projection to infinity of the planes of the counterclockwise disk (yellow), the northern arm (Narm, blue), the bar components of the minispiral (cyan), the circumnuclear disk (green), and the clockwise stellar disk (CWS, magenta) fitted from Paumard et al. (2006) (thick solid line), Lu et al. (2009) (thin dashed line), and Bartko et al. (2009) (thin dotted line). Figure taken from Lu et al. (2010)	14
1.5	The surviving fraction of encounters simulated by Addison et al. (2015) for each initial parameter. Top left: Penetration depth averaged over orientation and binary phase. Top right: Inclination averaged over penetration depth, azimuthal angle, and binary phase. Bottom left: Azimuthal angle averaged over penetration depth, azimuthal angle, and binary phase. Bottom right: Binary phase averaged over penetration depth and orientation. Figure taken from Addison et al. (2015)	17
1.6	2D histogram of disruptions vs. penetration depth ($\beta^{-1} = D$) and inclination ($\cos(i)$) with the solid line marking the range of inclination and penetration depth given by Eqn. 1.12. Figure taken from Addison et al. (2015)	18
1.7	2D histogram of surviving eccentricity $\log(e)$ vs. penetration depth (β^{-1}) and inclination ($\cos(i)$). Contours of constant eccentricity from right to left of $\log(e) = -5.5, -5.0, -4.5, \dots, 0$ from numerical results (white) and analytic solution given by Eqn. 1.10 (black). Figure taken from Addison et al. (2015)	20
1.8	Greyscale maps of change in Peters lifetime $\log(T_{GW}/T_{GW0})$ for different pairs of input parameters averaged over binary phase. Figure taken from Addison et al. (2015)	21

1.9	Galactic rest frame velocity and radius from the Galactic centre of currently observed HVSs as listed in table 1.1 with the LAMOST-HVSs marked by red triangles and HVSs discovered through other surveys marked by blue diamonds. The dashed and dot-dashed lines mark estimates for the escape velocity at given radius given by Brown et al. (2014) and Gnedin et al. (2010) respectively.	26
2.1	Layout of objects in a 3 body interaction with a binary star system (blue crosses) on a parabolic orbit (blue line) around a black hole (black dot at $0, 0$) with instantaneous distance from the central mass of r_m and binary separation of r . The axes are scaled to the distance of closest approach (r_p).	36
2.2	The path of the primary star's orbit relative to its partner integrated from the same initial conditions using the full 3 body model (black), the restricted general case (blue), and the restricted radial case (red). The penetration depth of the three body and general cases is set as 10^{-5} , the black hole mass in the 3 body case is set to $2 \times 10^6 m$ and binary phase at periastron is 0.0 . The distance is scaled to the initial separation a	51
2.3	The path of the primary star's orbit relative to its partner integrated from the same initial conditions using the full 3 body model (black) and the restricted general case (blue) with penetration depth $D = 10^{-2}$ and binary phase at periastron of 0.5π in a co-planar prograde orbit. The full 3 body model is integrated using a range of different black hole masses. The restricted general case has the same form as the free solution for variation in time.	52

2.4	Top: The mean ejection energy of stars in the radial case with $\theta = 0.50\pi, 0.25\pi, 0.10\pi$ in blue solid, dashed red, and dot-dashed black respectively, in units of $Gm_1m_2/a(M/m)^{1/3}$ as a function of the T_{min} . Bottom: The fractional difference in mean energy between $E(T_{min})$ and $E(T_{min} = 10^{-7})$ with $\theta = 0.50\pi, 0.25\pi, 0.10\pi$ in blue solid, dashed red, and dot-dashed black respectively.	53
2.5	Diagram describing the derivation of mean separation of points randomly distributed on the surface of a sphere.	57
2.6	The difference between the mean distance to points generated vis the three orientation sampling methods and the mean distance obtained from a perfect distribution. The Monte Carlo method is shown in black, the regular distribution method is shown in red, and the Deserno (2004) method shown in blue.	58
2.7	The initial circular orbit of a binary (red solid line) and its angular momentum vector (blue solid arrow) with its projection (blue dotted line) on the $Y-Z$ plane. The binary itself orbits the MBH on a parabolic orbit on the $X-Y$ plane. The red dashed line indicates another circular orbit which is symmetric to the red solid orbit with respect to the $X-Y$ plane. The two blue dashed arrows are the angular momenta of the same (red dashed) orbit but one orbiting in the prograde direction and the other in the retrograde.	59
2.8	The angular change in binary orientation as it approaches the black hole using a full three body integration on a highly elliptical outer orbit with $R_p = R_t, R_a = 1000R_t, e = 0, \theta = 0.25\pi,$ and $\phi = 0.5\pi.$	63
2.9	The change in binary eccentricity as it approaches the black hole using a full three body integration on a highly elliptical outer orbit with $R_p = R_t, R_a = 1000R_t, e = 0, \theta = 0.25\pi,$ and $\phi = 0.5\pi$	64

3.1	Probability of disruption as a function of the inclination angle θ in the radial approximation, with disruption probability measured using the energy oscillation method (blue) and eccentricity method (red).	67
3.2	Probability of disruption as a function of the penetration factor D . Disruption probability is averaged over all: binary orientations (black solid), coplanar prograde orbits (blue dashed), and coplanar retrograde orbits (red dot-dashed). The vertical dotted line marks the penetration limit for binaries of solar-type stars with $a = 1\text{AU}$ where the individual stars undergo tidal disruption.	68
3.3	Probability of disruption as a function of the penetration factor D averaged over all orientations (blue crosses) with the 5th order polynomial fit eqn. 3.1 (blue line) and the linear fit (red line).	70
3.4	Top panel: Ejection energy averaged over binary phase and orientation as a function of D . Bottom panel: Characteristic maximum ejection energy as a function of D . For a given D , the top 1% have ejection energy higher than the characteristic maximum energy E_{max} . Results for general binary orientations are given by the black solid line, coplanar prograde orbits are given by the blue dashed line, and coplanar retrograde orbits are given by the red dot-dashed line. The average and characteristic maximum energies are in units of $(Gm_1m_2/a)(M/m)^{1/3}$, and they are evaluated for the absolute value of the energy $ E $	71
3.5	The final energy of the primary star post disruption by a massive black hole starting from co-planar prograde orbits with penetration depth of $D = 10^{-1}$ with energy in units of $Gm_1m_2/a(M/m)^{1/3}$	73

3.6	Probability of disruption for a given D as a function of the inclination angle θ . Upper panel: deeper penetrators, the radial approximation (blue circles) and the general approximation with $D = 10^{-5}$ (blue solid), 10^{-2} (red dashed), 10^{-1} (green dot-dashed), and 0.3 (black dotted). Bottom panel: shallower penetrators, the general approximation with $D = 0.5$ (blue solid), 1.0 (red dashed), 1.5 (green dot-dashed) and 2.0 (black dotted).	75
3.7	Ejection energy averaged over binary phase and azimuth angle for a given D as a function of the inclination angle θ . Upper panel: deeper penetrators, radial solution (blue crosses), $D = 10^{-5}$ (blue solid), 10^{-2} (red dashed), 10^{-1} (green dot-dashed), and 0.3 (black dotted). Bottom panel, shallower penetrators $D = 0.5$ (blue solid), 1.0 (red dashed), 1.5 (green dot-dashed) and 2.0 (black dotted). The average energy is in units of $(Gm_1m_2/a)(M/m)^{1/3}$	77
3.8	Probability of disruption for a given D as a function of the inclination from prograde coplanar orientation. Upper panel: deeper penetrators, $D = 10^{-5}$ (blue solid), 10^{-2} (red dashed), 10^{-1} (green dot-dashed), and 0.3 (black dotted). Bottom panel, shallower penetrators $D = 0.5$ (blue solid), 1.0 (red dashed), 1.5 (green dot-dashed) and 2.0 (black dotted).	78
3.9	Ejection energy averaged over binary phase and inclination angle θ for a given D as a function of the inclination from prograde coplanar orientation. Upper panel: deeper penetrators, radial solution (blue crosses), $D = 10^{-5}$ (blue solid), 10^{-2} (red dashed), 10^{-1} (green dot-dashed), and 0.3 (black dotted). Bottom panel, shallower penetrators $D = 0.5$ (blue solid), 1.0 (red dashed), 1.5 (green dot-dashed) and 2.0 (black dotted). The average energy is in units of $(Gm_1m_2/a)(M/m)^{1/3}$. . .	80

3.10	The binary disruption probability P_{dis} averaged over all binary phase angles and orientations with penetration depth $D = 10^{-3}$ and different total sample sizes. The points on the blue line are samples with 2000 orientations and 50 – 800 binary phase angles, while the red line points are samples with 200 binary phase angles and 500 – 8000 orientation angles. There is no significant difference in disruption probability when increasing total sample size beyond 4×10^5	81
3.11	The final energy of the primary star post disruption by a massive black hole starting from co-planar prograde orbits with penetration depth of $D = 1$ (solid blue), 1.25 (dashed red), 1.75 (dot-dashed black), and 2 (dotted green) with energy in units of $Gm_1m_2/a(M/m)^{1/3}$	83
3.12	The final energy of the primary star post disruption by a massive black hole starting from co-planar prograde orbits with penetration depth of $D = 10^{-4}$ (solid blue), 10^{-3} (dashed red), 10^{-2} (dot-dashed black), and 3×10^{-2} (dotted green) with energy in units of $Gm_1m_2/a(M/m)^{1/3}$	84
3.13	The coefficients of the free solutions as functions of the initial binary phase: A_x (blue dashed) and B_x (red solid), along with the ejection energy of disrupted binaries (solid black line) rescaled by $Gm_1m_2/a(M/m)^{1/3}5(2/9)^{2/3}$, thus normalizing it to the same scale as B_x . The binary inclination $\theta = 0.3\pi$ is chosen for this plot as it best demonstrates the link between free solution coefficients and the surviving range. Binaries survive the deep tidal encounter if the initial binary phase is in a narrow range indicated by the vertical black dot-dashed lines.	86
3.14	The loci of positions in the parameter space for which the coefficients of the free solution A_x (blue solid) and B_x (red solid) are equal to zero, the energy of binary stars ejected from disrupted binaries goes to zero (black solid), and the range of binary phase for which binaries survive the deep tidal encounter (green area). The lower boundary of $E = 0$ and the A_x lines overlap.	88

3.15	The evolution of primary star energy with time for a binary on a radial orbit with $\theta = 0.3\pi$, and binary phase at periapsis of 0.17π . These initial conditions are on the surviving side of the A_x boundary in Fig. 3.14	89
3.16	Probability of disruption of eccentric binaries with respect to penetration depth for coplanar prograde (solid) and retrograde (dashed) orbits with $e = 0, 0.3, 0.6, \& 0.9$ (black, blue, red, & green, respectively). . .	92
3.17	Top panel: Ejection energy averaged over binary phase and the orientation of the semi-major axis. Bottom panel: Characteristic maximum ejection energy. These quantities are plotted as a function of the penetration factor D for coplanar prograde (solid) and retrograde (dashed) orbits with $e = 0, 0.3, 0.6 \& 0.9$ (black, blue, red & green, respectively). The average and characteristic maximum energies are in units of $(Gm_1m_2/a)(M/m)^{1/3}$, and they are evaluated for the absolute value of the energy $ E $	93
3.18	Radial approximation results for the inclination angle $\theta = \pi/2$. Top panel: Probability of disruption as a function of eccentricity. Middle panel: Ejection energy averaged over binary phase and the direction of the semi-major axis as a function of eccentricity. Bottom panel: Characteristic maximum ejection energy as a function of eccentricity. The average and characteristic maximum energy are in units of $(Gm_1m_2/a)(M/m)^{1/3}$, and they are evaluated for the absolute value of the energy $ E $	95

3.19	Top panel: Mean eccentricity difference from a parabolic orbit in bound stars as a function of D . Bottom panel: Maximum eccentricity difference from a parabolic orbit in bound stars as a function of D , where the bottom 1% have eccentricity lower than the characteristic minimum eccentricity e_{min} . Lines shown correspond to the general binary orientation (black solid), coplanar prograde orbits (blue dashed), and coplanar retrograde orbits (red dot-dashed). $m_1 = m_2$ and $M/m = 10^6$ are assumed.	97
3.20	Distribution of final semi-major axis of the surviving binary, in terms of the initial binary separation, as a function of penetration depth. The median semi-major axis is shown as the black line. The largest 15% of final semi-major axis values lie above the red line, while the smallest 15% are below the blue line.	100
3.21	Distribution of final eccentricities of the surviving binary as a function of penetration depth. The median eccentricity is shown as the black line, the largest 15% of final eccentricities lie above the red line, while the smallest 15% are below the blue line.	101
3.22	The cumulative frequency of binary merger timescales post massive black hole orbit in terms of their pre-orbit timescale for varying penetration depths. $D = 2$ (black), $D = 1$ (blue), $D = 0.5$ (red), $D = 0.2$ (yellow), $D = 0.1$ (green), $D = 10^{-2}$ (magenta).	103

Chapter 1

Introduction

1.1 Sgr A*

In the early 1960's the first optical detections of quasars were made by Schmidt (1963) and Matthews and Sandage (1963). These sources had redshift placing them within distant galaxies with an absolute magnitude brighter than any other galaxy discovered at that point. The luminosity of these sources could be explained as the result of matter falling onto a massive black holes within their host galaxy (Lynden-Bell, 1969). Lynden-Bell and Rees (1971) would go on to suggest that massive black holes could exist within most galaxies including our own Milky Way. In 1974 a radio source was detected from the centre of our galaxy around Sagittarius A by Balick and Brown (1974). This source would not be properly named until a 1982 paper wherein it was referred to as Sgr A* (Brown, 1982).

Ghez et al. (1998) made observations of the motions of stars within the central 25arcsec^2 of our galaxy. These findings placed strong constraints on the composition of the central mass within our galaxy with a massive black hole with mass $2.6 \pm 0.2 \times 10^6 M_{\odot}$ being the most likely with other options being too unstable to collapse in the form of a cluster of low mass dim stars, neutron stars, or stellar black holes, or simply not having any feasible formation method in the form of a dense ball of bosons which would have

a radius only slightly larger than that of the Schwarzschild radius of the predicted black hole.

These results would later be supported by Schödel et al. (2002) who came to the same conclusion based on in depth observations of S0-2, one of the S stars orbiting in close proximity around Sgr A*, with periapsis $R_p = 124\text{AU}$. These observations were made using high resolution near-IR imaging and spectroscopy over the course of ten years covering a the majority of S0-2's 15.2 year orbital period. They found that S0-2's orbit is associated with a central mass of $(3.5 \pm 1.5) \times 10^6 M_\odot$.

With the presence of massive black holes in the centre of galaxies Hills (1975) proposed a method by which gas could be transported to the Schwarzschild radius of them, fueling the quasars that had been previously detected. Hills proposed that stars in the nuclear cluster would be ripped apart by the massive black hole if their orbits brought them within the stars' Roche limit $(6M/\pi\rho)^{1/3}$, where M is the mass of the black hole, and ρ is the density of the star. This is called a tidal disruption event (TDE), where the matter that comprised the star is pulled apart with part of the gas accreting onto the massive black hole. The luminosity expected from galaxies based on this method is dependent on the density of stars in the nuclear cluster with larger densities producing faster orbital diffusion, the highest densities leading to accretion at the Eddington limit ($L_E = 3.2 \times 10^4 (M/M_\odot)L_\odot$). Accretion at this rate will either grow the black hole mass until the Schwarzschild radius grows larger than the Roche limit of the star; this occurs at around $M = 3.2 \times 10^8 M_\odot$. Alternatively the disruption of these stars depletes the nuclear cluster until the luminosity falls below the Eddington limit.

In the case of our own galaxy the stellar density around the black hole is low enough that the rate of stellar disruption via TDEs is far slower than the initial accretion rate with a predicted stellar disruption rate of approximately one star every 10^4 years (Rees, 1988). The radio emission observed from our own galaxy would therefore come from the last remnant of a long ago disrupted star or gas cloud in a low level accretion flow.

1.2 Binary TDE studies

Expanding on their work on TDEs by a massive black hole Hills (1988) considered the potential for binary star systems on a close orbit around a massive black hole. These binaries would undergo a similar form of disruption to that of a single star if their orbit brought them within the binary's tidal radius,

$$R_T = \left(\frac{M}{m}\right)^{\frac{1}{3}} a, \quad (1.1)$$

where m is the total mass of the binary and a is the binary semi-major axis. In this case instead of the comprising matter being spread out with a distribution of orbital energies with approximately 50% being ejected, the result is the two binary partners on independent orbits with the total orbital energy of the binary split between them. This can result in one of the disrupted partners gaining a significant amount of energy from its partner and being ejected from the nuclear cluster at high speed.

The term Hyper-Velocity Stars (HVS) was coined by Hills (1988) to describe stars with a velocity greater than the escape velocity of the galaxy (of the order of 1000km s^{-1} at the Galactic centre, Rossi et al., 2017) that would be produced as a result of these interactions. Hills argued that observation of such a HVS would be evidence of a massive compact object present in our own Galaxy, that being the then theorized super massive black hole (SMBH) known as Sgr A*. These HVS's have sufficient velocity to not only escape from the pull of the SMBH but potentially also escape the Milky Way itself while their former partners remain bound in tight orbits around the SMBH. This mechanism for the production of HVS's is known as the Hills mechanism. These stars would be recognizable by both their high velocity and by their relatively young age and high metallicity in comparison to the stars in their local areas, as hypervelocity stars would have a similar population to that of the Galactic centre.

Hills (1988) also models the disruption of equal mass ($m_1 = m_2 = 1M_{\odot}$) binary systems with a perturbing mass of $M_{bh} = 10^4, 10^5, 10^6, 10^7M_{\odot}$. These binaries all begin with a semi-major axis of $a = 0.01\text{AU}$ except for two data sets with $a = 0.02\text{AU}$ &

0.1AU which were run only for a perturbing mass of $M_{bh} = 10^6 M_{\odot}$. With a binary centre of mass velocity at infinity of 250 m s^{-1} these orbits were all hyperbolic with the total energy of the three body system being positive, however the initial velocity was much smaller than the velocity of the binary at the tidal radius and so results of interactions were only weakly dependent on the binary centre of mass velocity at infinity. Hills' simulations found that the probability of the ejection of a HVS through an exchange collision (where one binary partner becomes bound to the SMBH while the other is ejected, a specific case of a binary TDE) is strongly dependent on the triple system's initial conditions. However the probability averaged over binary phase and with random binary angular momentum orientation is approximately the same for a given value of the dimensionless parameter $D \equiv (R_p/a)(M/m)^{-1/3}$ where R_p is the periapsis of the binary's orbit around the black hole (note that Hills measured penetration depth with a normalizing factor $D_{min} = (R_p/a)(2M/10^6 m)^{-1/3}$, see Fig. 1.1). In some literature this parameter is characterized by its inverse, $\beta = D^{-1}$. The same is true for the average energy of the ejected binary which is also relatively invariant for a given value of D . These simulations were run using point particles as the three bodies, however obviously there is a minimum limit on the value of R_p beyond which you enter the Roche limit of the individual star placing a lower limit in terms of the dimensionless penetration factor D beyond which solar type stars cannot survive an orbit. For an equal mass binary this limit is:

$$D_{crit} \approx \frac{R_{\odot}}{a}, \quad (1.2)$$

where R_{\odot} is the radius of the star. For binaries comprised of compact objects D_{crit} is much smaller than for main sequence stars allowing them to penetrate much deeper into the black hole's gravitational well. Compact objects also do not have the risk of interactions between binary members such as mass exchange, tidal deformation or collisions.

Hills' first models were done for binaries with a small centre of mass velocity at infinity relative their velocities at the tidal radius, however his later simulations involve higher energy orbits (Hills, 1991). It is in this study where it is important to recognize the

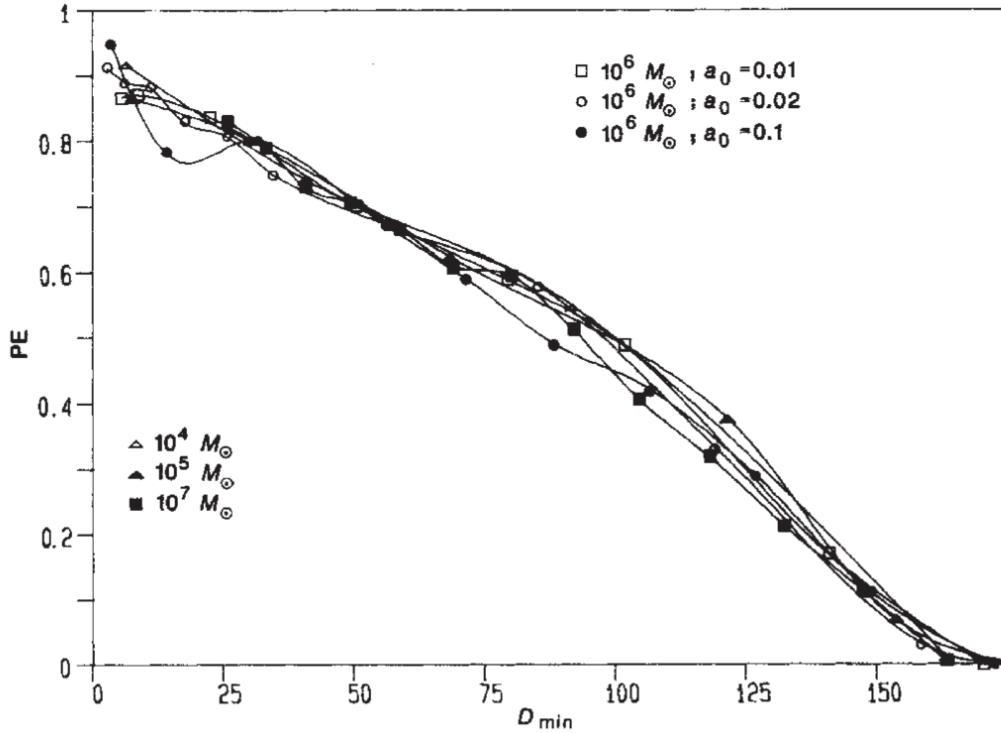


Figure 1.1: The probability of an exchange collision as a function of penetration depth as found by Hills (1988). Penetration depth here is taken using Hills normalization $D_{min} \sim 80D$ and binary separation is given in units of AU. Figure is taken from Hills (1988)

distinction between a binary dissociation and an exchange collision. Both are forms of binary TDEs, however in an exchange collision one of the binary partners remains bound to the black hole while the other is ejected, while binary dissociation occurs when neither of the binary partners is bound to the black hole, and neither are they bound to each other. Within my work, unless otherwise specified, binary disruption is used to mean exchange collision as within my framework dissociation is not relevant.

Dissociation can only occur in binary TDEs where the binary orbital energy is greater than the characteristic change in energy of the binary partners as a result of their disruption. This characteristic energy change is a function of the black hole mass such that $\Delta E \propto M^{1/3}$, as shown in Hills (1988). As a result of this, binaries being disrupted by more massive black holes require a larger orbital energy in order to become dissociated (Hills, 1991). A larger dissociation rate leads to a reduced chance of an exchange collision as the total disruption rate as a function of the penetration depth is not strongly dependent on the orbital energy of the binary. This lack of dependence

can be explained by considering the velocity of the binary centre of mass at the tidal radius,

$$V_{cm}(R_t)^2 \approx \left(\frac{M}{10^6 M_\odot}\right)^{\frac{2}{3}} \left(\frac{a}{0.01 \text{AU}}\right)^{-1} 10^{15} \text{m}^2 \text{s}^{-2} + V_\infty^2. \quad (1.3)$$

For higher mass SMBHs the first term dominates over the initial velocity, and the orbit approximates to a zero energy parabolic orbit as in Hills (1988).

Although it was not stated explicitly in Hills (1991), Fig. 1.2 (taken from that paper) shows that even in cases with a periastron distance close to zero the probability of a binary exchange is not 100% specifically the bottom right panel of Fig. 1.2 and the line marked with a solid circle with ~ 0 orbital energy where dissociation is not possible. This result is interesting, suggesting that binaries are able to survive deep penetrating orbits. Although as has already been said there is a limit on the periastron distance a binary orbit can have before there is a risk of stellar tidal disruption given by equation 1.2.

The rate of binary TDEs is based on the rate of binaries entering the so called loss cone, that being the range of angular momentum parameter space that would allow a binary star system to be in an orbit that would result in a binary TDE with periapsis distance $R_p \leq R_T$. Working under the reasonable assumption that the orbital energy of the binary was negligible and the orbit could be treated as parabolic, a binary enters the loss cone when it has a specific angular momentum of:

$$h^2 \leq h_{lc}^2 = 2R_T^2 \left[E - \frac{GM}{R_T} \right] \approx 2GM R_T, \quad (1.4)$$

(Yu and Tremaine, 2003). Depending on the rate at which binaries enter the loss cone we can define the HVS production rate as being in the full loss cone or the empty loss cone regimes. In the full loss cone regime the change in angular momentum over a single orbit is larger than the loss cone angular momentum, meaning that the loss cone is continually and uniformly refilled with the number distribution of periapsis distance $n(R_p) \propto R_p$. Because of this the rate of HVS production is dependent on the tidal radius with binaries with larger tidal radii more frequently disrupted (Hills, 1988).

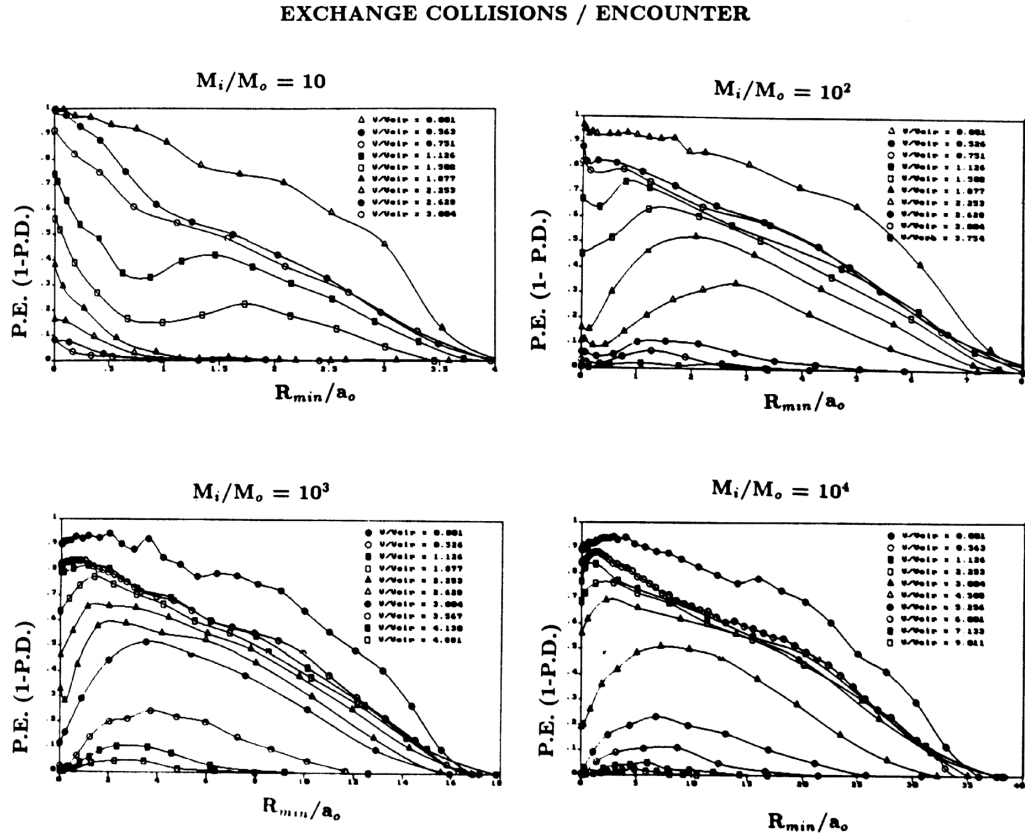


Figure 1.2: The probability of an exchange collision as a function of the periastron distance of the binary orbit as found by Hills (1991) with different black hole mass in terms of the mass of one binary member (M_0) and binary velocity at infinity in terms of the binary internal velocity. Top left panel: black hole mass $10M_0$ with velocities $0.001 < V_\infty/V_{orbital} < 3.004$. Top right panel: black hole mass 10^2M_0 with velocities $0.001 < V_\infty/V_{orbital} < 3.754$. Bottom left panel: black hole mass 10^3M_0 with velocities $0.001 < V_\infty/V_{orbital} < 4.801$. Bottom right panel: black hole mass 10^4M_0 with velocities $0.001 < V_\infty/V_{orbital} < 9.011$. Figure taken from Hills (1991).

In the empty loss cone regime the change in a binary's specific angular momentum over a single orbit is much smaller than the loss cone angular momentum. In this regime the binary orbit slowly shifts until $h \approx h_{cl}$. If this were the only factor driving change in the binary orbit we would expect an exponential drop off in binaries occupying $h < h_{lc}$. However this extremely slow evolution allows rarer scattering events to become the dominant factor in driving the change in angular momentum. Because of this binaries in the empty loss cone regime approach the black hole with a flat distribution in D (Weissbein and Sari, 2017). This rate is independent of the binary's mass or separation.

Hills (1988) made an approximation of the rate at which we could expect binary TDEs to occur within our own galaxy using the same method as Hills (1975). However this rate also requires the density of stars in the Galactic centre to be large enough that TDE's would not significantly affect the total density (full loss cone). Hills estimated a HVS ejection rate of $\sim 10^{-3}\text{yr}^{-1}$ which would suggest high number of HVSs that would be observable, however at that point there had been none reported from existing surveys.

This prediction of the rate of binary TDEs would later be improved upon by Yu and Tremaine (2003) using a method similar to Hills' method of estimating the HVS rate. However, Yu and Tremaine considered the potential for Binary TDEs to deplete the loss cone making the dominant factor in the binary TDE rate the diffusion rate of stars in the nuclear cluster filling the loss cone (empty loss cone). Evaluating the TDE rate in this way assuming a binary separation of $a = 0.3\text{AU}$,

$$n_{TDE} \approx 1.5 \times 10^{-5} \left(\frac{\eta}{0.1} \right) \text{yr}^{-1}, \quad (1.5)$$

where η is the diffusion constant, a factor that determines the rate at which gravitational relaxation occurs and is of the order of 0.1. The binary TDE rate is only weakly dependent on binary separation decreasing to $0.9 \times 10^{-5} (\eta/0.1) \text{yr}^{-1}$ at $a = 0.01\text{AU}$.

Zhang et al. (2013) also calculate the rate of binary TDEs based on the several models and injection methods, with a rate of 10^{-3}yr^{-1} in the full loss cone regime and a

minimum rate of 10^{-5}yr^{-1} in the empty loss cone regime. Based on the stellar mass functions and observations of HVSs they predicted the rate of TDEs in our galaxy to be within the range of $10^{-5} - 10^{-4}\text{yr}^{-1}$.

This method of binary tidal disruption serves as an explanation for stars observed in close proximity to Sgr A*, such as the star S0-2 that was mentioned previously being used by Schödel et al. (2002) to confirm the presence of the SMBH in the Galactic centre. Stars would not be able to form due to the tidal forces that would act on any star forming cloud in such close proximity to a massive black hole. As one star is ejected its partner loses energy and becomes bound to Sgr A*. The change in velocity of a star due to disruption is derived by Yu and Tremaine (2003) as of the order of,

$$\Delta v \sim \sqrt{\frac{Gm}{a} \frac{m_p}{m}}, \quad (1.6)$$

where m_p is the mass of the star's binary partner. If the binary is disrupted at the periastron of its orbit we can find the orbital parameters of the bound star, as the bound star's periastron would be the same as the binary's periastron and has $v(r_p) = v_m(r_p) - \Delta v$. Assuming that the energy change due to the binary TDE is significantly larger than the orbital energy of the binary pre-disruption, the semi-major axis of the bound star is approximately $a_b = a(M/m)^{2/3}$. Compare this estimate to the observed orbital conditions of S0-2 with a semi-major axis of 953AU and mass $13.6^{+2.2}_{-1.8}M_\odot$ (Habibi et al., 2017); assuming no change in orbital parameters post disruption, this would suggest that S0-2 originated from a binary with initial separation $\sim 0.9\text{AU}$. An equal mass binary with this initial separation would have a tidal radius of 44AU, significantly less than the periastron of S0-2. This coupled with the rarity of binaries with such a large separation, implies some form of post-disruption relaxation. This discrepancy could also be explained by S0-2 originating in a binary with a more massive partner $m_p \sim 200M_\odot$ and a larger binary semi-major axis $a \sim 4\text{AU}$ (Gould and Quillen, 2003). A binary with these conditions could also disrupt producing a bound star similar to S0-2. However if Gould and Quillen's explanation for S0-2's orbital parameters can be applied to other S stars we can observe, it suggests that large mass ratio binaries are the norm given the range of eccentricities we observe, with eccentricities as low as

0.358 ± 0.036 for S1 (Eisenhauer et al., 2005). If these high mass-ratio binaries were the norm we would expect to see several high mass S stars resulting from binary TDEs where the low mass member is ejected.

Further numerical studies would follow after the identification of the first HVS, SDSS J090745.0+024507 in 2005 (Brown et al., 2005). Gualandris et al. (2005) attempted to test three different origins for the first HVS, disruption of a binary star system by a massive black hole, the acceleration of a single star by a massive black hole binary, and the disruption of an intermediate mass ($100 - 1000M_{\odot}$) black hole-star binary (IMBHSB) by a massive black hole. All these methods are capable of producing stars with the same velocity as the observed star under the right circumstances. Of these three methods of HVS production the disruption of IMBHSB produces the highest energy HVSs as the ejection energy of disrupted binaries is proportional to the mass of the binary partner. However, the expected rarity of intermediate mass black holes in binaries with main sequence stars leaves the HVS rate from this method prohibitively low at 10^{-11}yr^{-1} . The massive black hole binary acceleration model requires Sgr A* to be a single component in a binary system; to date there has been no evidence to suggest that this is the case, leaving us with the disruption of a binary star system as the most likely origin of SDSS J090745.0+024507.

To predict the full spectrum of escape velocities of HVSs, Bromley et al. (2006) also performed numerical simulations of binary disruptions for a range of initial conditions holding one binary partner mass within a small range $3M_{\odot} < m_1 < 4M_{\odot}$ with the other star's mass sampled over a larger range $0.5M_{\odot} < m_2 < 4M_{\odot}$, the binary separation sampled between 0.05AU and 4AU, and the closest approach distance to the black hole sampled between 1AU and 700AU. Bromley et. al. confirmed the findings of Hills (1988) that the disruption probability could be given as a function of binary separation, closest approach distance and the masses of the black hole and binary given in the form of the penetration depth. Bromley et al. (2006) also numerically give the

average velocity of an ejected star as a function of the penetration depth:

$$\langle v_1 \rangle = 1750 \left(\frac{2m_2}{m} \right)^{\frac{1}{2}} \left(\frac{a}{0.1\text{AU}} \right)^{-\frac{1}{2}} \left(\frac{m}{2M_\odot} \right)^{\frac{1}{3}} \left(\frac{M}{3.5 \times 10^6 M_\odot} \right)^{\frac{1}{6}} \mathcal{F}(D) \text{km s}^{-1}, \quad (1.7)$$

where $\mathcal{F}(D)$ is of the order of unity and can be fit to a fifth order polynomial with coefficients: $A_0 = 0.774$, $A_1 = 0.0204$, $A_2 = -6.23 \times 10^{-4}$, $A_3 = 7.62 \times 10^{-6}$, $A_4 = -4.24 \times 10^{-8}$, $A_5 = 8.62 \times 10^{-11}$. After normalizing with the penetration depth the most significant effect on the distribution of ejection velocities comes from the orientation and orbital phase of the binary. In Fig. 1.3 Bromley et al. (2006) shows the distribution of ejection velocities for a given set of initial conditions with a Gaussian fit with $\langle v_1 \rangle = 2600 \text{km s}^{-1}$ and $\sigma = 500 \text{km s}^{-1}$, with $\sigma \approx 0.2 \langle v_1 \rangle$ found to be a reasonable approximation for a wide range of initial conditions with μ taken from equation 1.7.

Bromley et al. (2006) found that the HVSs with the highest ejection velocities come from binaries with angular momentum strongly aligned with the binary centre of mass angular momentum around the black hole (prograde). They also gave the probability of an individual encounter resulting in a disruption as a linear function of penetration depth,

$$P_{dis} \approx 1 - \frac{D}{2.2}, \quad (1.8)$$

This is a good approximation of Hills' results (Fig. 1.2) in the range of parameters covered in their sample, but it does not account for surviving binaries in the deepest penetrations. Using a galactic density profile of

$$\rho(r) = \frac{\rho_0}{1 + \left(\frac{r}{a_c} \right)^2}, \quad (1.9)$$

where ρ_0 is the central density ($1.27 \times 10^4 M_\odot \text{pc}^{-3}$) and a_c is the core radius (8pc), Bromley et al. (2006) found their results to be in good agreement with observational data for most HVS velocities falling within the predicted ejection velocities for $3 - 4 M_\odot$. The only significant outlier was US708 (Hirsch et al., 2005) which later observations would suggest as originating from a supernova ejection and not a binary

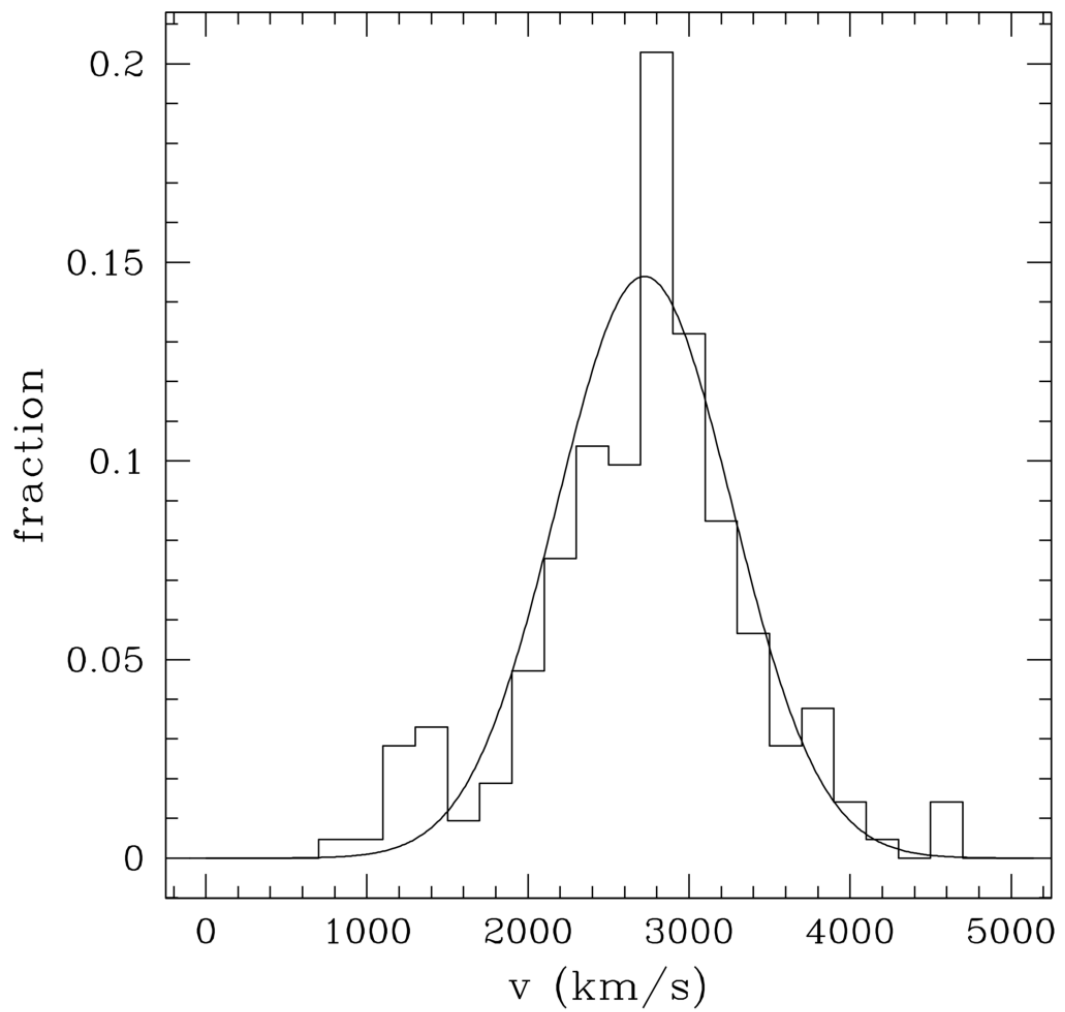


Figure 1.3: Distribution of ejection speeds immediately after disruption for a binary with $m_1 = 4M_\odot$, $M = 3.5 \times 10^6 M_\odot$, $a = 0.1\text{AU}$, and $R_p = 5\text{AU}$. This orbit corresponds to a penetration depth of $D \approx 0.5$. Figure taken from Bromley et al. (2006).

disruption (Geier et al., 2015).

While the velocity of HVSs immediately after disruption is not dependent on star mass, the stellar lifetime introduced a dependence of mass on the spatial distribution of HVSs with more massive stars needing higher velocities to reach the halo within their own lifetimes (Sesana et al., 2007).

The trajectory of an ejected HVS can be obtained analytically from the energy of the HVS. Post disruption, the path of the HVS follows approximately the same trajectory as the path of the initial binary with the same periapsis but with a increased eccentricity. The deflection angle of a binary's velocity at periapsis from its initial injection velocity at infinity is given by $\pi/2 - \Psi$ where $\tan(\Psi) = \sqrt{|1 - e^2|}$. As the injection trajectory can be treated as parabolic with $e = 1$ the change in the trajectory of the new orbit is equal to $\tan^{-1}(\sqrt{|1 - \Delta e^2|})$. For a HVS ejected with velocity 750km s^{-1} - 1000km s^{-1} the ejected HVS is only deflected by $\sim 8^\circ$. Because the trajectory is only changed by a small amount HVS populations memorize their origin in the galactic core (Lu et al., 2010). The spatial distribution of observed HVSs is not isotropic when projected from the galactic centre, however this distribution can be linked to existing structures in the Galactic centre as shown in Fig. 1.4 (taken from Lu et al., 2010).

From these positions the majority of observed HVSs have a high probability of originating from the clockwise stellar disk (CWS) or the northern arm (Narm). However these origins result in new problems as the population in the CWS disk does not reflect what would be expected from the observed sample of HVSs. Due to observational constraints, HVS detections are limited to B type stars. These stars have a flight time from the Galactic centre of $\sim 1 - 2 \times 10^8\text{yr}$, while the populations of OB stars in the CWS disk are only $6 \pm 6 \times 10^6\text{yr}$ old (Levin and Beloborodov, 2003). The CWS disk would need to have been rejuvenated with young stars over the past $2 \times 10^8\text{yr}$ to replace stars lost to binary TDEs, however star formation in the region is suppressed by the presence of Sgr A*, preventing sufficiently large gas clouds from forming new stars.

Stars may be injected into the loss cone from these structures through the Kozai-Lidov

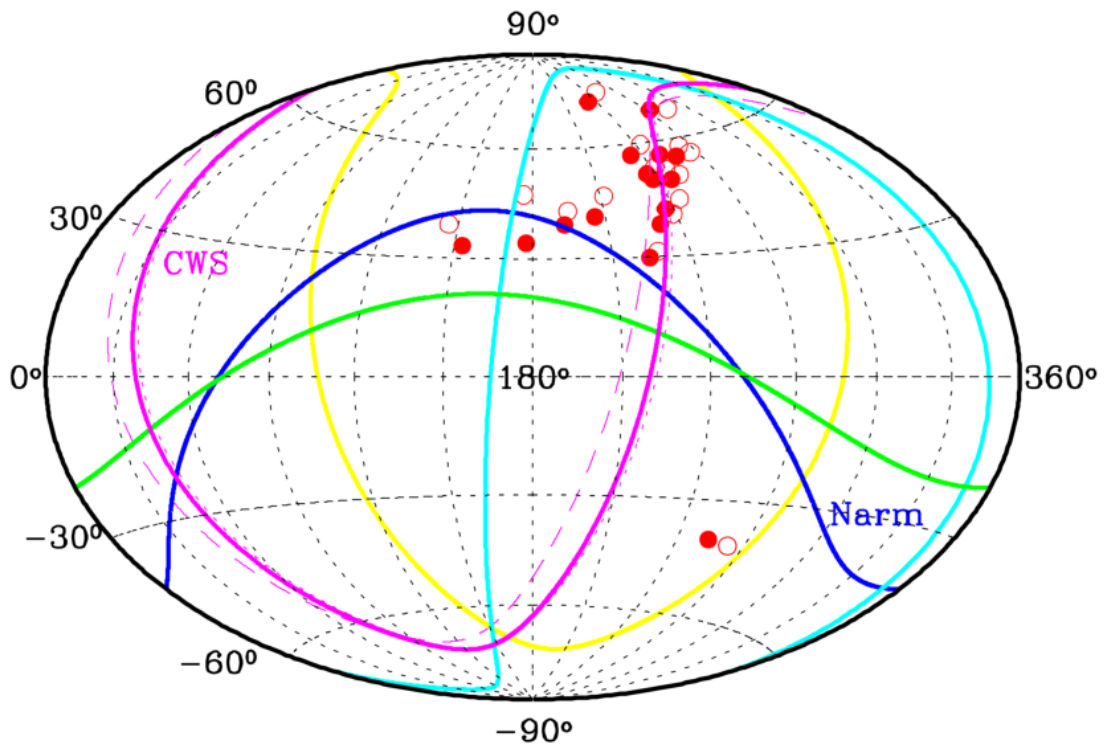


Figure 1.4: Projection of the coordinates of observed HVSs and some structures in the Galactic centre, with open circles being stars with their coordinates centred on the earth and closed circles being the stars' coordinates centred in the Galactic centre. The curves show the projection to infinity of the planes of the counterclockwise disk (yellow), the northern arm (Narm, blue), the bar components of the minispiral (cyan), the circumnuclear disk (green), and the clockwise stellar disk (CWS, magenta) fitted from Paumard et al. (2006) (thick solid line), Lu et al. (2009) (thin dashed line), and Bartko et al. (2009) (thin dotted line). Figure taken from Lu et al. (2010)

mechanism (Kozai, 1962; Lidov, 1962) with other stars in the disk pushing them into eccentric orbits around the black hole. Šubr and Haas (2016) would test this method in their own study, in which they populated a disk of 2000 binaries and examined the evolution of the disk. They begin with a disk populated with an IMF of $n_m \propto m^{-3/2}$ and a binary separation equally distributed in log space. All binaries initially beginning with no relative inclination to the disk and eccentricity $e = 0.9(a - a_{min}) / (a_{max} - a_{min})$ where $a_{min} = 0.04\text{pc}$ and $a_{max} = 0.4\text{pc}$ define the range of the separation distribution. They found that injection in this method can produce binaries with large internal eccentricity and inclination relative to the disk. This method also found some stars ejected directly from the disk through scattering although these ejected stars cannot reach the same velocities as those produced through binary disruption. This study also confirms that stars ejected from the Galactic centre maintain a similar orbit to its originating disk. The mass function of HVSs produced through this mechanism differs from the IMF of the disk, with high mass stars being preferentially ejected as HVSs. This could be explained in two ways: first that as massive stars are more likely to have massive partners, the massive stars are typically going to be ejected with higher velocity and therefore be recorded as HVSs, second is that more massive binaries will sink towards the inner part of the disk at a greater rate due to two-body relaxation and once there the effect of the Kozai-Lidov mechanism is more pronounced pushing them into the loss cone.

Extreme mass ratio inspirals are produced when a compact object (CO) merges with a massive black hole; this merger occurs as a result of energy lost in the form of gravitational waves from the CO. These COs can initially become bound to the black hole from close two body encounters (Miller et al., 2005). However binary tidal disruption presents an alternate method for CO capture as observations of X-ray transients within the central 1pc of the Galactic centre suggests the presence of binaries comprised of COs (Muno et al., 2005; Laycock et al., 2005). The difference between these two capture methods is the initial semi-major axis of the bound CO, as the two-body encounter method requires the orbit to be close enough that gravitational waves can be emitted. If it is very tightly bound and eccentric from the start, it can begin inspiraling from grav-

itational wave emission immediately. Binary disruption only requires the binary to be within its tidal radius. Both methods leave the bound CO on highly eccentric orbits but the wider orbit of the TDE method allows the bound CO circularize before merging with the black hole entering the LISA detection range with $e \sim 0.01$ (Miller et al., 2005) while close capture COs begin emitting with higher eccentricity $e \sim 0.5 - 0.9$. Binaries that are able to survive their encounter with a SMBH are also relevant to the field of gravitational wave astronomy, as perturbations from the encounter can leave the surviving binary in a tighter and more eccentric orbit which reduces the time required for a binary CO system to merge through gravitational wave emission (Peters, 1964).

Considering the relevance of the Hills method to gravitational wave astronomy, Addison et al. (2015) produced their own study with more detailed exploration of the specific parameters beyond simply the penetration depth that leads to the disruption of binary systems. Addison et al. (2015) explore a range of penetration depths $0.35 < D < 5$, defined therein using the parameter $\beta = D^{-1}$ in an empty loss cone distribution of periapsis (equally distributed), with random binary orientation defined by its inclination from a prograde orbit i , and the longitude of their ascending node Ω_0 , and random initial binary phase θ_0 . The survival rate of binary encounters is plotted for each of these parameters in Fig. 1.5 taken from the same paper.

When averaged over the other parameters the most significant parameters are penetration depth and inclination with there being no consistent trend for azimuthal angle and binary phase when averaged over these shallow penetrations. We can understand the disruption of binaries in terms of a change of eccentricity derived by Heggie and Rasio (1996) for a circular binary on a parabolic orbit:

$$\Delta e = 6\sqrt{\pi}2^{\frac{1}{4}}D^{\frac{3}{4}}\exp\left[-\frac{(2D)^{3/2}}{3}\right]\mathcal{G}(i, \phi), \quad (1.10)$$

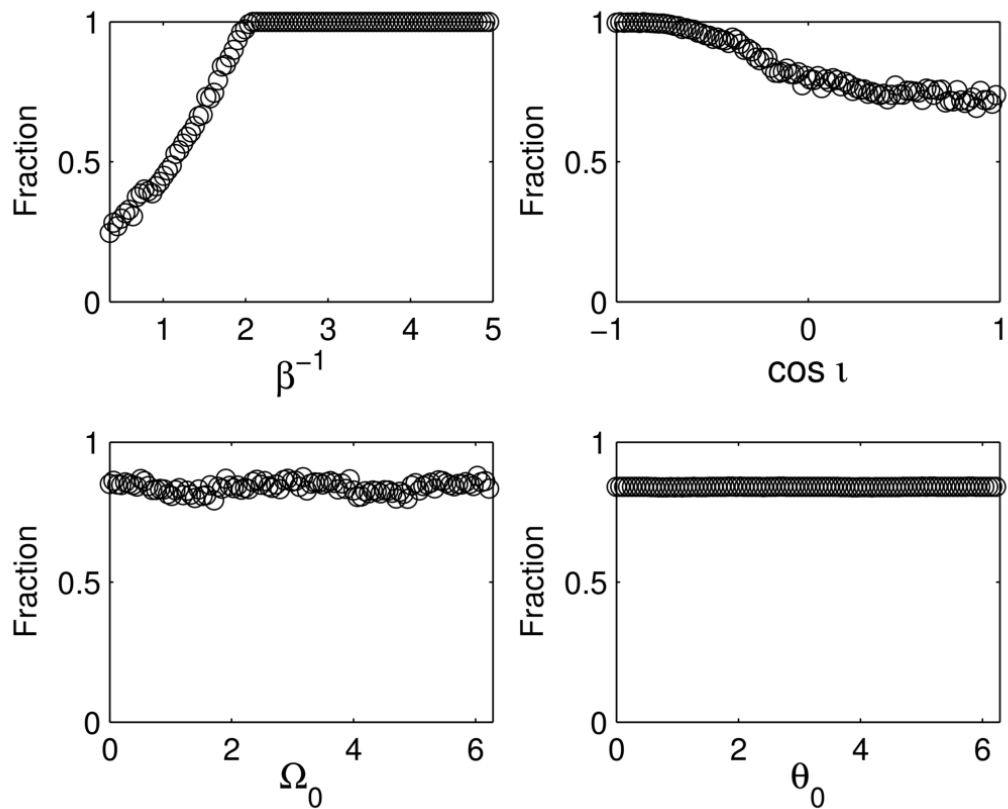


Figure 1.5: The surviving fraction of encounters simulated by Addison et al. (2015) for each initial parameter. Top left: Penetration depth averaged over orientation and binary phase. Top right: Inclination averaged over penetration depth, azimuthal angle, and binary phase. Bottom left: Azimuthal angle averaged over penetration depth, azimuthal angle, and binary phase. Bottom right: Binary phase averaged over penetration depth and orientation. Figure taken from Addison et al. (2015)

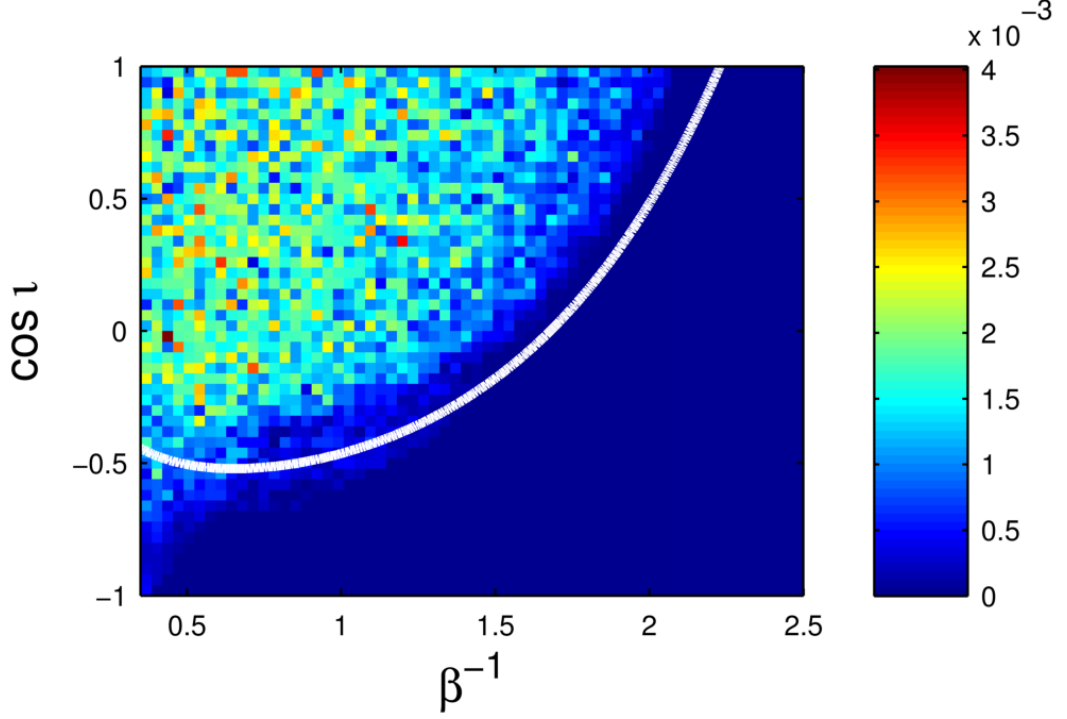


Figure 1.6: 2D histogram of disruptions vs. penetration depth ($\beta^{-1} = D$) and inclination ($\cos(i)$) with the solid line marking the range of inclination and penetration depth given by Eqn. 1.12. Figure taken from Addison et al. (2015)

where $\mathcal{G}(i, \phi)$ is of the order of unity and given by

$$\mathcal{G}(i, \phi) = \cos^2\left(\frac{i}{2}\right) \left[\cos^4\left(\frac{i}{2}\right) + \sin^2\left(\frac{i}{2}\right) + \frac{4}{3} \cos^2\left(\frac{i}{2}\right) \sin^2\left(\frac{i}{2}\right) \cos \phi \right]^{\frac{1}{2}}, \quad (1.11)$$

where $\cos(\phi)$ is a function of azimuthal angle and binary phase. By setting $\cos \phi$ to be equal to unity and knowing that for a disrupted binary $\Delta e \geq 1$ we can define a range of penetration depth and inclination for which disruption can occur.

$$\frac{1}{\mathcal{G}(i, 0)} = 6\sqrt{\pi} 2^{\frac{1}{4}} D^{\frac{3}{4}} \exp\left[-\frac{(2D)^{3/2}}{3}\right] \quad (1.12)$$

As can be seen in Fig. 1.6 this range is accurate for $D \gtrsim 1$ but for deeper penetrations it is less accurate with disrupted binaries found even where $i = \pi$ where equation 1.10 would suggest that disruption should not be possible. Once well within this range however the disruption rate is not strongly dependent on penetration depth and inclination

with disruptions distributed fairly evenly with any differences potentially being due to the random sampling method used to obtain the data.

To explore the implications for binary CO mergers, Addison et al. (2015) also examined the range of final eccentricity and separation in binaries that survived encounters within their sample. In these surviving cases the binary will either tighten with the centre of mass gaining energy, or soften with the binary becoming bound to the black hole. In this way binaries are divided into three classes: Bound binaries with a merger timescale greater than the binary centre of mass orbital period (Long BEMRI), Bound binaries with a merger timescale shorter than the binary centre of mass orbital period (short BEMRI), and unbound stars. The merger timescale of a binary CO due to gravitation wave emission, sometimes referred to as the Peters lifetime (Peters, 1964), is given approximately as,

$$T_{GW} \approx 150 \text{Myr} \left(\frac{m}{M_{\odot}} \right)^{-3} \left(\frac{a}{R_{\odot}} \right)^4 (1 - e)^{\frac{7}{2}}. \quad (1.13)$$

The eccentricity of a surviving binary can be taken to a reasonable degree of accuracy from equation 1.10 for shallow penetration depths and prograde inclinations but as with applications for disruption conditions (seen in Fig. 1.6) it does not hold for deeper penetrations as can be seen by comparing the numerical and analytic results for surviving eccentricity (white and black contours in Fig. 1.7). The general trend however holds with binaries surviving a deep penetrating encounter having a significantly higher post encounter eccentricity than binaries surviving a shallow penetration.

The semi-major axes of post encounter binaries experience a much less significant change as a result of their encounter with the overall mean found to be $\langle a/a_0 \rangle = 0.988$ with 97% of binaries in the range of $0.5 < a/a_0 < 1.5$. The most significant change in semi-major axis comes from binaries with penetration depth $D < 2$, with shallower penetrations producing a much less pronounced change. The post encounter semi-major axis also features a stronger dependence on Ω_0 than is seen in the disruption chance or eccentricity. Binaries entering with $i = \pi/2$ and $\Omega = \pi/2$ or $3\pi/2$ will be left with a larger semi-major axis. These orientations correspond to binaries with

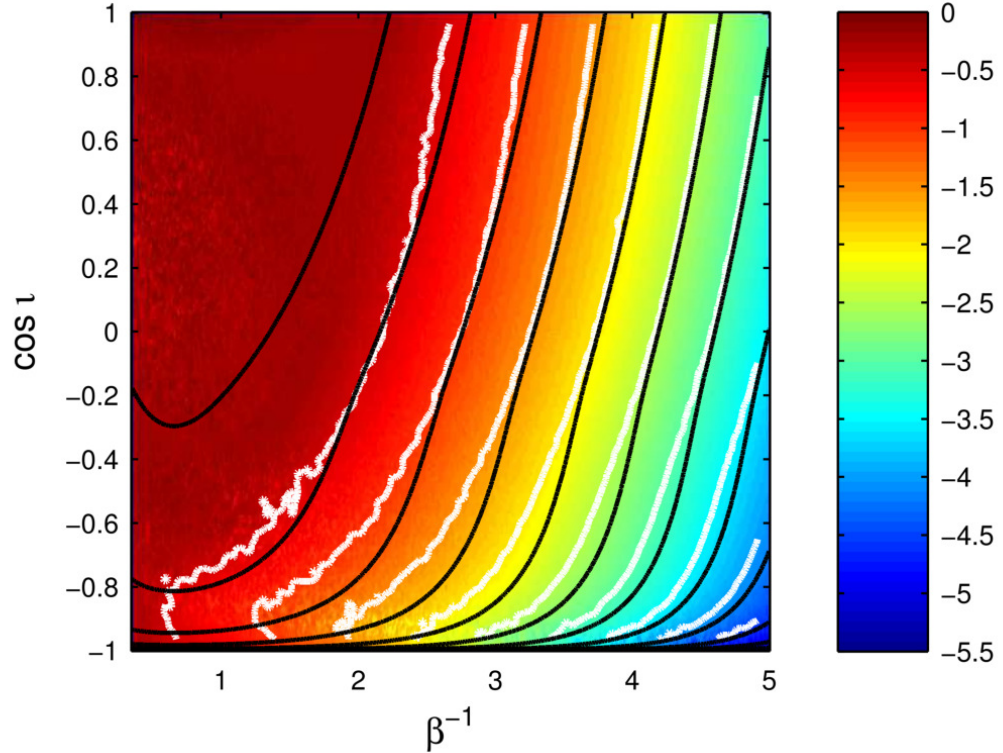


Figure 1.7: 2D histogram of surviving eccentricity $\log(e)$ vs. penetration depth (β^{-1}) and inclination ($\cos(i)$). Contours of constant eccentricity from right to left of $\log(e) = -5.5, -5.0, -4.5, \dots, 0$ from numerical results (white) and analytic solution given by Eqn. 1.10 (black). Figure taken from Addison et al. (2015)

orbital angular momentum vector pointed approximately towards or away from the black hole.

While the encounter can produce a wide range of post-encounter Peters times, the surviving binaries within this range of parameters sampled by Addison et al. (2015) had an average Peters time of $T_{GW} \approx 0.84T_{GW0}$ where T_{GW0} is the initial Peters time $\sim 10^8$ yr. As all binaries in their are initially circular the surviving eccentricity can only increase, therefore all binaries with $T_{GM}/T_{GW0} > 1$ must have a wider semi-major axis. In this way the distribution of Peters time is strongly dependent on that of semi-major axis. This relatively unchanged Peters time combined with estimates for encounter rates and CO binary population mean the rate of detected binary coalescence would only be enhanced by as much as 1%, an amount that would be difficult to verify given the expected scarcity of these events.

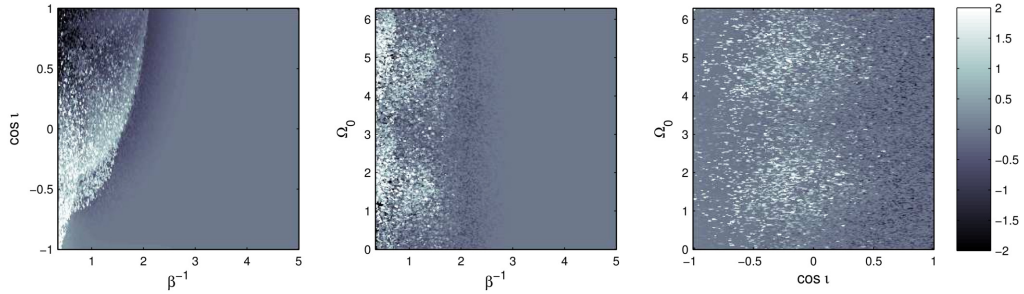


Figure 1.8: Greyscale maps of change in Peters lifetime $\log(T_{GW}/T_{GW0})$ for different pairs of input parameters averaged over binary phase. Figure taken from Addison et al. (2015)

While the velocity of a HVS immediately after disruption can be estimated based on analytical models of binary disruption, observations of HVSs to date have been limited to stars that have already reached the Galactic halo (Brown et al., 2006a,b, 2007a,b, 2009, 2012, 2014). An understanding of the velocity distribution of HVSs can be used to make predictions of the Galactic potential by comparing observed proper motions in the halo with predicted ejection velocities. The velocity of an ejected star at infinity if acting only under the gravity of the black hole is

$$\langle v \rangle = \sqrt{\frac{2Gm_p}{a}} \left(\frac{M}{m} \right)^{\frac{1}{6}} \mathcal{H}, \quad (1.14)$$

where m_p is the mass of the ejected star's partner, m is the total binary mass, M is the black hole mass and \mathcal{H} is a function of the encounter geometry of the order unity. Rossi et al. (2014) use numerical simulations along with distributions of binary initial conditions to predict the distribution of HVS velocities at ejection in both the empty and full loss cone regimes. In their work they utilize both the analytical solution above and Monte Carlo simulations to numerically calculate the actual ejection velocity. Heavy extinction due to dust makes it difficult to know the distribution of masses and orbital parameters of binaries in the Galactic centre. Instead the distribution is taken as being similar to the distribution found observationally in the solar neighborhood (Duquennoy and Mayor, 1991) and clusters (Kiminki and Kobulnicky, 2012) where binaries are found to have a logarithmic distribution of semi-major axis $f_a \propto a^{-1}$ with a minimum separation a_{min} larger than the Roche limit of the stars to prevent mass exchange between binary partners. For the mass of the partner star m_p , Rossi et al. (2014) con-

siders two cases, the first being a case where all binaries have equal mass, and the second where the mass of the partner obeys a power law distribution $f_m \propto m_p^{-\alpha}$ where $\alpha > 1$ with partner mass ranging between $m_{min} = 0.5M_\odot$ and $m_{max} = 100M_\odot$.

To numerically obtain the ejection velocity Rossi et al. (2014) used a semi-analytic approximation of the 3 body interaction first proposed by the same group in Sari et al. (2010). My own work utilizes the same approximation and the full derivation will be described in Section 2.2. Briefly the approximation considers the separation of the binary partners moving in a time-dependent potential from the black hole. The initial conditions are normalized in terms of penetration depth to limit parameter space and reduce computation time.

In the analytic solution Rossi et al. (2014) found that the rate of ejection of stars \dot{N}_v , for a given velocity v , is dominated by stars that come from binaries with the least massive possible companion, with the highest velocity ejections only reachable by compact binaries with equal mass partners. In the low velocity case the rate is due to ejections with low mass partners, while in the high velocity case they are dominated by ejections from compact binaries which, as the minimum separation is dependent on the mass of the partner, is also dominated by the low mass binaries.

Observations of HVSs were and continue to be very rare with the range of velocities being very narrow with a cut off at $675 - 709 \text{ km s}^{-1}$. Comparing these limited observations with the numerical results from Rossi et al. (2014) suggests that the distribution of binary separation is not flat in log space but instead favours wider separations. This could be the effect of a filtering process that would cause contact binaries to collide or undergo stellar TDEs during their orbit.

As most observed HVSs are located in the halo Rossi et al. (2017) did not assume any specific model for the galaxy mass distribution but instead described the Galactic potential by the minimum velocity V_G that an object requires to reach a radius of 50kpc which is dependent only on the total mass contained within that radius. Most of the HVSs' deceleration occurs within this radius so the velocity distribution is expected to be independent of radius outside 50kpc. Based on this the velocities of HVSs could be

used to calculate the escape velocity of the galaxy to be $\sim 800\text{km s}^{-1}$.

1.3 Observations

1.3.1 Hyper-Velocity Stars

Hyper-velocity stars (HVSs) would go unobserved for eighteen years after Hills' original paper until 2005 when the first was discovered by Brown et al. (2005). SDSS J090745.0+024507 is a B9 main sequence star with a Galactic rest frame radial velocity of 709km s^{-1} that is located in the Galactic halo at a distance from the Galactic centre of 50kpc giving it a velocity of over twice the escape velocity from the Galaxy.

The second HVS, US 708, discovered by Hirsch et al. (2005), was a helium rich O type star with a Galactic rest frame velocity of 1157km s^{-1} , one of the fastest objects in the Galaxy. While initially it was theorized to have been produced via the Hills mechanism, proper motion measurements found it to have an origin in the Galactic disk and interactions with a SMBH were ruled out (Geier et al., 2015). US 708 is more likely have originated from a supernova ejection.

A third HVS, HE 0437-5439, was discovered by Edelmann et al. (2005), another main sequence B-type star with a Galactic rest frame velocity of 563km s^{-1} . In order for HE 0437-5439 to have been ejected from the Galactic centre it would have had to have been ejected 100Myr ago. This is much longer than its main sequence lifetime of 25Myr. Given its proximity to the Large Magellanic Cloud (18kpc) it was initially posited that it may have been ejected from there instead. Proper motion measurements from Hubble Space Telescope would later confirm that HE 0437-5439 was traveling away from the Galaxy (Brown et al., 2010), but the proper motion constraints were not sufficient to rule out a Large Magellanic Cloud origin (Irrgang et al., 2013). If HE 0437-5439 did originate from the Galactic centre then, in order to make sense of the discrepancy between the flight time of the star and its main sequence lifetime, it is required that HE 0437-5439 be a blue straggler; the result of a merger or mass transfer

between two stars forming a star with a younger apparent age (Chatterjee et al., 2013). This suggests that the initial binary disruption would in fact have been a disruption of a hierarchical triple system ejecting a binary that later merged.

Aiming to expand the sample of HVS's, observational efforts turned to more comprehensive searches of the Galactic halo (Brown et al., 2006a,b, 2007a,b, 2009, 2012, 2014). As the stellar population of the Galactic halo is made primarily of older late type stars the search targets faint B-type stars with lifetimes consistent with travel time from the Galactic centre. The HVS survey confirmed at least 16 new HVSs making up the majority of HVS observations to date.

With data from the LAMOST spectroscopic survey three additional HVS candidates have been identified: LAMOST-HVS1 (Zheng et al., 2014), LAMOST-HVS2, and LAMOST-HVS3 (Huang et al., 2017). All of the three candidates are, like previously discovered HVSs, B type stars. The positions of all three HVSs on the sky are consistent with stars ejected from star forming regions around the Galactic centre, however the flight time for LAMOST-HVS1 and LAMOST-HVS2 is longer than the lifetime of the stars themselves suggesting that if these stars did originate from the Galactic centre then they are most likely blue stragglers much like HE 0437-5439. The lifetime of LAMOST-HVS3 is however longer than its flight time giving it long enough to have been ejected normally through the Hills mechanism.

With the release of GAIA data release 2 we were provided with high precision astrometry allowing for better constraints on the proper motion of HVSs. GAIA DR2 contains proper motions of all HVSs to date, with the exception of HVS14 and HVS23 for which there are too few observations to constrain proper motions, along with a large number of bound high velocity stars that may have been ejected through binary TDEs with Galactic rest frame velocity $> 275\text{km s}^{-1}$. Brown et al. (2018b) uses data from GAIA DR2 for these stars, comparing with the previous observations from Hubble. The Hubble Space Telescope seems to be more fitting of observing faint stars, of magnitude $g > 18.5$, with errors in proper motion up to four times smaller than those from GAIA. GAIA can have errors up to three times smaller for stars brighter than this.

Table 1.1 shows a list of HVSs observed to date that may have been ejected through tidal disruption, with their heliocentric and Galactic rest frame velocities (v_{\odot} and v_{rf} respectively), their distance to the Galactic centre (R_{GC}), and their Galactic longitude and latitude (l and b respectively) along with the paper in which they were first reported. Note the lack of HVS2 and HVS11 in the list as the former had been found to originate in the disc (Geier et al., 2015) while the latter’s Galactic rest frame velocity of 315.2km s^{-1} is below the escape velocity at 54kpc (Brown et al., 2014). This does not rule HVS11 out from originating in the Galactic centre but as it is not unbound it does not fit the definition of HVS. There are other HVSs that are only marginally unbound as the choice of Galactic potential can leave some HVSs below the escape velocity at their position. In Fig. 1.9 the Galactocentric distance and velocity of HVSs as listed in table 1.1 are shown with escape velocity estimates taken from Brown et al. (2014) and Gnedin et al. (2010). HVS15, HVS16, HVS24, LAMOST-HVS1, LAMOST-HVS3 all lie below one of these fits.

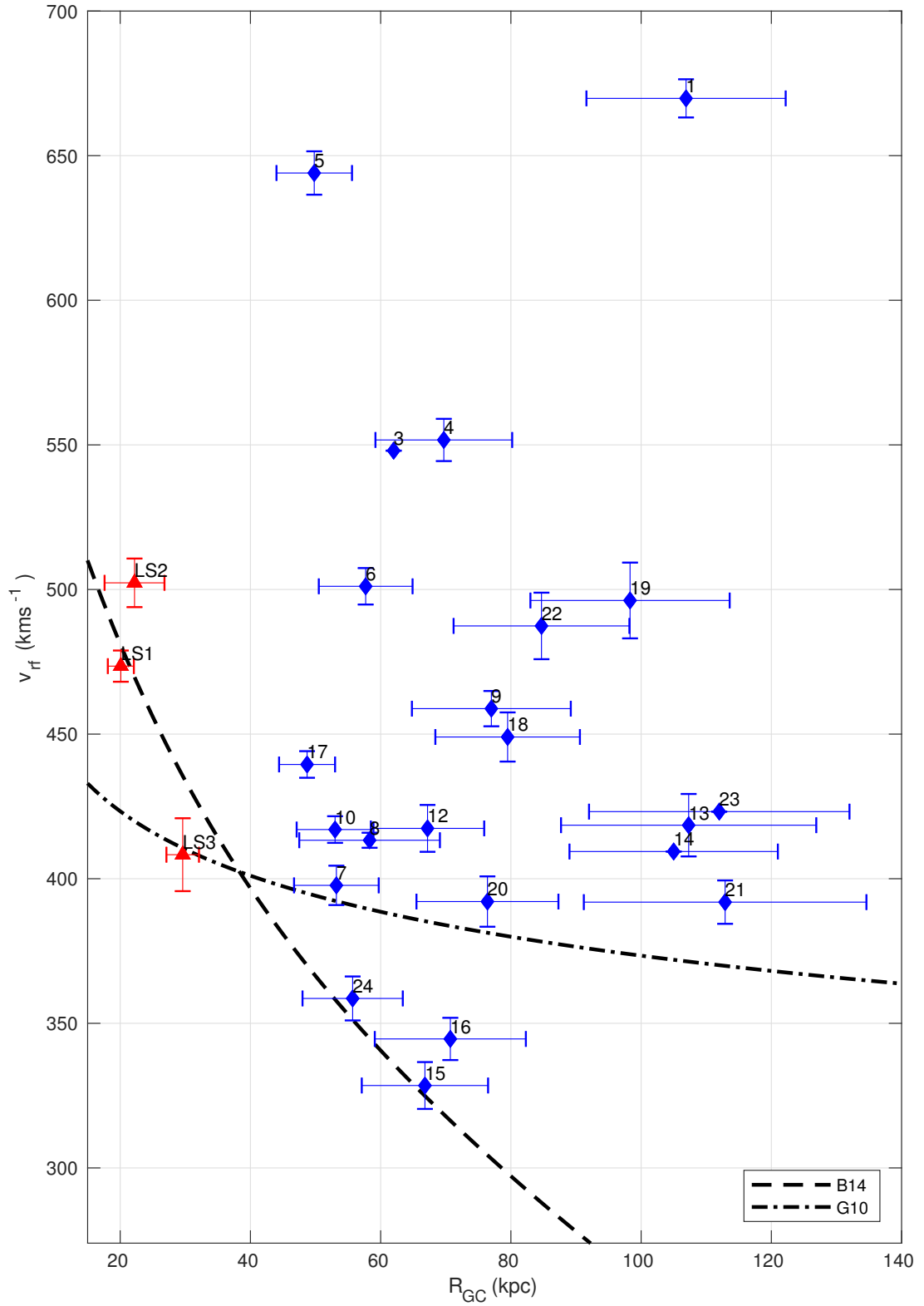


Figure 1.9: Galactic rest frame velocity and radius from the Galactic centre of currently observed HVSs as listed in table 1.1 with the LAMOST-HVSs marked by red triangles and HVSs discovered through other surveys marked by blue diamonds. The dashed and dot-dashed lines mark estimates for the escape velocity at given radius given by Brown et al. (2014) and Gnedin et al. (2010) respectively.

ID	v_{\odot} (km s ⁻¹)	v_{rf} (km s ⁻¹)	R_{GC} (kpc)	l (deg)	b (deg)	Catalog	Original paper
HVS1	833.0 ± 5.5	669.8 ± 6.6	106.9 ± 15.3	227.33	+31.33	SDSS J090744.99+024506.88	1
HVS3	723	548	62	263.04	+47.05	HE 0437-5439	2
HVS4	600.9 ± 6.2	551.7 ± 7.3	69.7 ± 10.5	194.76	+42.56	SDSS J091301.01+305119.83	3
HVS5	545.5 ± 4.3	644.0 ± 7.5	49.8 ± 5.8	146.23	+38.70	SDSS J091759.47+672238.35	3
HVS6	609.4 ± 6.8	501.1 ± 6.3	57.7 ± 7.2	243.12	+59.56	SDSS J110557.45+093439.47	4
HVS7	526.9 ± 3.0	397.7 ± 6.8	53.2 ± 6.5	263.83	+57.95	SDSS J113312.12+010824.87	4
HVS8	499.3 ± 2.9	413.3 ± 2.6	58.3 ± 10.8	211.70	+46.33	SDSS J094214.03+200322.07	5
HVS9	616.8 ± 5.1	458.8 ± 6.1	77.0 ± 12.2	244.63	+44.38	SDSS J102137.08005234.77	5
HVS10	467.9 ± 5.6	417.0 ± 4.6	53.0 ± 5.9	249.93	+75.72	SDSS J120337.85+180250.35	5
HVS12	552.2 ± 6.6	417.4 ± 8.1	67.2 ± 8.7	247.11	+52.46	SDSS J105009.59+031550.67	6
HVS13	569.3 ± 6.1	418.5 ± 10.8	107.3 ± 19.6	251.65	+50.64	SDSS J105248.30000133.94	6
HVS14	537.3 ± 7.2	409.4	105 ± 16	241.78	+53.20	SDSS J104401.75+061139.02	6
HVS15	461.0 ± 6.3	328.5 ± 8.1	66.8 ± 9.7	266.51	+55.92	SDSS J113341.09012114.25	6
HVS16	429.8 ± 7.0	344.6 ± 7.3	70.7 ± 11.6	285.86	+67.38	SDSS J122523.40+052233.84	6
HVS17	250.2 ± 2.9	439.5 ± 4.6	48.7 ± 4.3	73.52	+41.16	SDSS J164156.39+472346.12	7
HVS18	237.3 ± 6.4	449.0 ± 8.5	79.5 ± 11.1	103.64	-26.77	SDSS J232904.94+330011.47	7
HVS19	592.8 ± 11.8	496.2 ± 13.1	98.3 ± 15.3	256.05	+63.74	SDSS J113517.75+080201.49	7
HVS20	512.1 ± 8.5	392.1 ± 8.7	76.4 ± 10.9	262.56	+60.39	SDSS J113637.13+033106.84	7
HVS21	356.8 ± 7.5	391.9 ± 7.5	112.9 ± 21.7	165.26	+56.11	SDSS J103418.25+481134.57	7
HVS22	597.8 ± 13.4	487.4 ± 11.5	84.7 ± 13.5	263.33	+62.10	SDSS J114146.44+044217.29	8
HVS23	259.3 ± 9.8	423.2	112 ± 20	059.36	-39.47	SDSS J215629.01+005444.18	8
HVS24	492.5 ± 5.3	358.6 ± 7.6	55.7 ± 7.7	256.27	+54.55	SDSS J111136.44+005856.44	8
LAMOST-HVS1	611.7 ± 4.6	473.5 ± 5.4	20.1 ± 2.0	221.10	+35.41	LAMOST-HVS1	9
LAMOST-HVS2	341.1 ± 7.8	502.3 ± 8.4	22.2 ± 4.6	60.40	+45.25	LAMOST-HVS2	10
LAMOST-HVS3	361.4 ± 12.5	408.3 ± 12.6	29.6 ± 2.5	165.14	-31.20	LAMOST-HVS3	10

Table 1.1: Table of observed HVSs. (1) Brown et al. (2005), (2) Edelmann et al. (2005) (3) Brown et al. (2006a) (4) Brown et al. (2006b), (5) Brown et al. (2007b), (6) Brown et al. (2009), (7) Brown et al. (2012), (8) Brown et al. (2014), (9) (Zheng et al., 2014) (10) Huang et al. (2017)

1.3.2 S-Stars

Within the Galactic core, at a distance from Sgr A* of less than 0.04pc there exists a population of young B-Dwarf stars with highly eccentric orbits and random angular momentum orientations that do not conform to the local disk like structures found further out such as the clockwise and counter-clockwise rotating stellar disks (Eisenhauer et al., 2005).

The orbits of the very closest stars, within 0.5arcsec of Sgr A*, are the best constrained as their orbits are fast enough to reliably track over short timescales. This distance corresponds to a semi-major axis of $< 4\text{AU}$ and an orbital period of $< 135\text{yr}$. Observations of stars within this region over 10 years starting in 1992 allowed for the full orbital motion of the closest S-stars to be extrapolated along with orbital period giving a constraint on the mass of Sgr A*. Schödel et al. (2003) and Eisenhauer et al. (2005) would do this with the S-stars S1, S2, S8, S12, S13, S14 giving the best view of the stars in our Galactic core.

Due to the tidal forces in the area around Sgr A* it is difficult for gas clouds to condense down and form stars without being disrupted first. These stars must therefore have migrated into these orbits by other means. Binary disruption is a plausible explanation for how these stars may have become bound to Sgr A*; as one member of a binary is ejected as a HVS its partner becomes bound having lost the energy that the HVS gained (Ginsburg and Loeb, 2006). For equal mass binaries, stars bound to the SMBH through the Hills mechanism do however have very large eccentricities with $e > 0.98$ (Brown et al., 2018a); only two S-Stars, S8 ($e = 0.97$) & S14 ($e = 0.98$), have the eccentricity that we would expect. It is possible however that for binaries with larger initial mass ratios ($m_1/m_2 \ll 1$) bound stars can reach eccentricities of $e = 0.8$ (Zhang et al., 2013). Specifically, in an unequal mass binary if the less massive star becomes bound then it will have a lower eccentricity than if the more massive star were to be bound. In a parabolic orbit both stars have equal chance of being ejected, however in a hyperbolic orbit the less massive star will be preferentially bound while in an elliptical orbit the more massive star will be more likely to be bound (Kobayashi et al., 2012).

Stars bound in this way initially remain on the orbital plane that the binary was injected towards the SMBH on. This is counter to what we see from the isotropic orientations of the S-stars and the eccentricities are also much lower than can be formed through the Hills mechanism alone.

Chapter 2

Binary Exchange collision and the Restricted 3 Body Problem

To simulate the orbit of binaries around massive black holes I utilize a restricted solution to the 3-body problem. In this chapter I will explain the conditions under which it is possible for a binary tidal disruption event to occur. I will also go through the derivation of my solution and detail the sampling methods I utilize to generate my results.

2.1 Conditions required for an exchange collision

A binary exchange collision occurs when a binary star system is acted on by a massive third body (a massive black hole) causing one of the binary members to become unbound from its partner and bound to the third body. There are two requirements for an exchange collision: first the tidal forces must be powerful enough to disrupt the binary, and second the energy change from the disruption must be sufficient for one partner to be bound and the other to be ejected.

The Tidal Radius

The first step, the unbinding of the binary, occurs as a result of a tidal disruption event, where the tidal force from the third body on each partner (F_t) becomes large enough to pull the binary apart. The point where this occurs is defined as the tidal radius R_t and can be described with three different arguments: The argument from acceleration, the argument from velocity, and the argument from separation.

- The argument from acceleration defines the tidal radius as the distance at which the tidal acceleration A_t is equal to the gravitational acceleration of the binary star system A_b . The tidal acceleration is defined as the difference between the gravitational acceleration on each binary partner from the black hole:

$$\begin{aligned} A_t &= \frac{GM}{(R_m - \frac{a}{2})^2} - \frac{GM}{(R_m + \frac{a}{2})^2}, \\ &\approx \frac{2GMa}{R_m^3}, \end{aligned} \quad (2.1)$$

where M is the mass of the black hole, R_m is the distance from the black hole to the binary centre of mass, a is the binary separation, and assuming that $R_m \gg a$ which I find to be valid for all cases I consider.

Then we find:

$$\begin{aligned} \frac{Gm}{a^2} &= \frac{2GMa}{R_m^3}, \\ R_m &\approx a \left(\frac{M}{m} \right)^{\frac{1}{3}}, \end{aligned} \quad (2.2)$$

where m is the total mass of the binary system.

- The argument from velocity defines the tidal radius as the distance where the change of velocity over the dynamical timescale Δt due to the tidal acceleration ($A_t \Delta t$) is comparable to the escape velocity of the binary components $v_e = \sqrt{2Gm/a}$. Due to the binary's orbit any changes to the binary caused by tidal

acceleration will cancel out when averaged over multiple rotations, and because of this the dynamical timescale must be shorter than or comparable to the binary orbital timescale ($P_b = \sqrt{a^3/GM}$) in order for a binary to be disrupted. The tidal radius can therefore be defined as:

$$\begin{aligned} \sqrt{\frac{2Gm}{a}} &= \frac{2GMa}{R_m^3} \sqrt{\frac{a^3}{Gm}}, \\ R_m &\approx a \left(\frac{M}{m} \right)^{\frac{1}{3}}. \end{aligned} \quad (2.3)$$

- The argument from position is similar to the argument from velocity. It defines the tidal radius as the distance where the displacement over the dynamical timescale due to the tidal acceleration $\sim A_t \Delta t^2$ is comparable to the initial binary separation a .

$$a = \frac{GMa}{R_m^3} \frac{a^3}{Gm}, \quad (2.4)$$

$$R_m = a \left(\frac{M}{m} \right)^{\frac{1}{3}}. \quad (2.5)$$

This definition of the tidal radius also conveniently makes the dynamical timescale of both the centre of mass orbit and the internal binary orbit equal.

Energy Change due to disruption

Within the tidal radius the massive black hole is able to disrupt the binary causing the components to become independent. The eventual fate of the binary components is dependent on the initial total orbital energy of the system and the energy gained or lost by the components. It can be shown that if the latter is much larger than the self binding energy of the binary $\sim Gm^2/a$ then both stars may become bound (if the initial energy is negative), or ejected (if the initial energy is positive).

In a parabolic orbit the energy of an individual star post disruption is only from the

change in energy due to the disruption ΔE . The size of ΔE can be approximated in three ways by considering: the change in kinetic energy, the change in gravitational potential energy, and work done during the binary orbit (Sari et al., 2010).

- In the kinetic energy case I consider ΔE simply to be based on the relative velocity of the individual binary components. In this case I assume the disruption occurs instantaneously, the binary arrives at the tidal radius in a circular orbit and the two stars become independent of each other maintaining their previous position and velocity acting only under the black hole's gravity. The star that gains energy has a velocity post disruption of $\mathbf{v}_1 \approx \mathbf{V}_m + \mathbf{v}$ where \mathbf{V}_m is the velocity of the binary centre of mass at the tidal radius ($V_t = \sqrt{GM/R_t}$), and \mathbf{v} is the velocity of the star at disruption relative to its partner ($v_0 = \sqrt{Gm/a}$). This leads to a change in kinetic energy of the order of:

$$\begin{aligned} \Delta E &= \frac{1}{2}m(V_m + v_0)^2 - \frac{1}{2}mV_m^2, \\ &\approx mV_mv_0, \end{aligned} \tag{2.6}$$

since the centre of mass velocity is much larger than the binary orbital velocity I have ignored the second order term. This gives a change in energy of

$$\Delta E = \frac{Gm^2}{a} \left(\frac{M}{m} \right)^{\frac{1}{3}}. \tag{2.7}$$

Since $M \gg m$, ΔE is much larger than the binding energy of the binary.

- In the potential energy case I consider the difference in potential energy of the two binary partners at the tidal radius, again assuming an instantaneous disruption. The distance from the energy-gaining star to the black hole is $r_1 = R_t + a/2$ and its partner is located at $R_t - a/2$. The difference in the two stars' potential energy is of the order of

$$\begin{aligned}
\Delta E &= \frac{GMm}{R_t - a/2} - \frac{GMm}{R_t + a/2}, \\
&= \frac{GMma}{R_t^2}, \\
&= \frac{Gm^2}{a} \left(\frac{M}{m} \right)^{1/3}.
\end{aligned} \tag{2.8}$$

- At the tidal radius the binary orbital timescale becomes identical to the centre of mass black hole orbital timescale ($P_{bh} = \sqrt{R_t^3/GM}$); this means that over the course of one half period of the binary it has been displaced by R_t while each star is acting on its partner, pulling it around its orbit, doing work equal to force times displacement. The mutual gravity force between the two stars is

$$F = \frac{Gm^2}{a^2}, \tag{2.9}$$

so the change in energy due to work done over the dynamical timescale is of the order of:

$$\begin{aligned}
\Delta E &= \frac{Gm^2 R_t}{a^2}, \\
&= \frac{Gm^2}{a} \left(\frac{M}{m} \right)^{1/3}.
\end{aligned} \tag{2.10}$$

Each of three arguments results in the same estimate for the energy lost by a star and gained by its partner and from these three arguments I can analytically estimate the range of energies between which an exchange collision is plausible. In order for an exchange collision to occur a star must gain or lose enough energy such that one is ejected with positive energy and one is bound with negative energy. For binaries in a parabolic orbit this is certain due to their zero energy orbit and conservation of energy, but in hyperbolic or elliptical orbits the energy change may not be sufficient to result in a binary exchange.

Considering a plausible apoapsis R_a for elliptical orbits around the central massive

black hole within a galaxy I can place constraints on the range of orbital parameters for which the total orbital energy E_m is less than the change in energy due to disruption. Starting with orbits with R_a around the edge of the black hole's sphere of influence $r_h = GM/\sigma^2$ where σ is the local stellar velocity dispersion $\sim 100\text{km/s}$ (Genzel et al., 2010). In the Milky Way, this is of the order of several parsecs, and with these orbital parameters the orbital energy of the binary is $\sim 10^{-3}\Delta E$. The limit for apoapsis of a binary orbit, where $E_m \sim \Delta E$ is $R_a = (M/m)^{1/3}R_t$, in these orbits binaries will preferentially be bound to the black hole even if the binary is disrupted.

It can be shown that a binary on an orbit with total orbital energy $E_m = \Delta E$ will have comparable velocity at the tidal radius to a binary on a zero energy orbit.

$$\begin{aligned} V_t^2 &= \frac{\Delta E}{m} + \frac{GM}{R_t}, \\ &= \frac{Gm}{a} \left(\frac{M}{m}\right)^{\frac{1}{3}} + \frac{GM}{R_t}, \\ &= \frac{GM}{R_t} \left(1 + \left(\frac{m}{M}\right)^{\frac{1}{3}}\right). \end{aligned} \tag{2.11}$$

As in my scenario $M \gg m$, it is clear that for any binary orbital energy that can result in an exchange collision I can use a parabolic orbit.

2.2 The Restricted 3 body problem

2.2.1 General Approximation

In order to simplify the 3 body system involved in binary disruption events I utilize a form of the restricted 3 body problem first outlined in Sari et al. (2010). In this section the derivation of this method will be explained in depth.

I start with a binary system injected on an orbit towards a massive object from a distance significantly larger than the tidal radius. First the equation of motion of each component is given as:

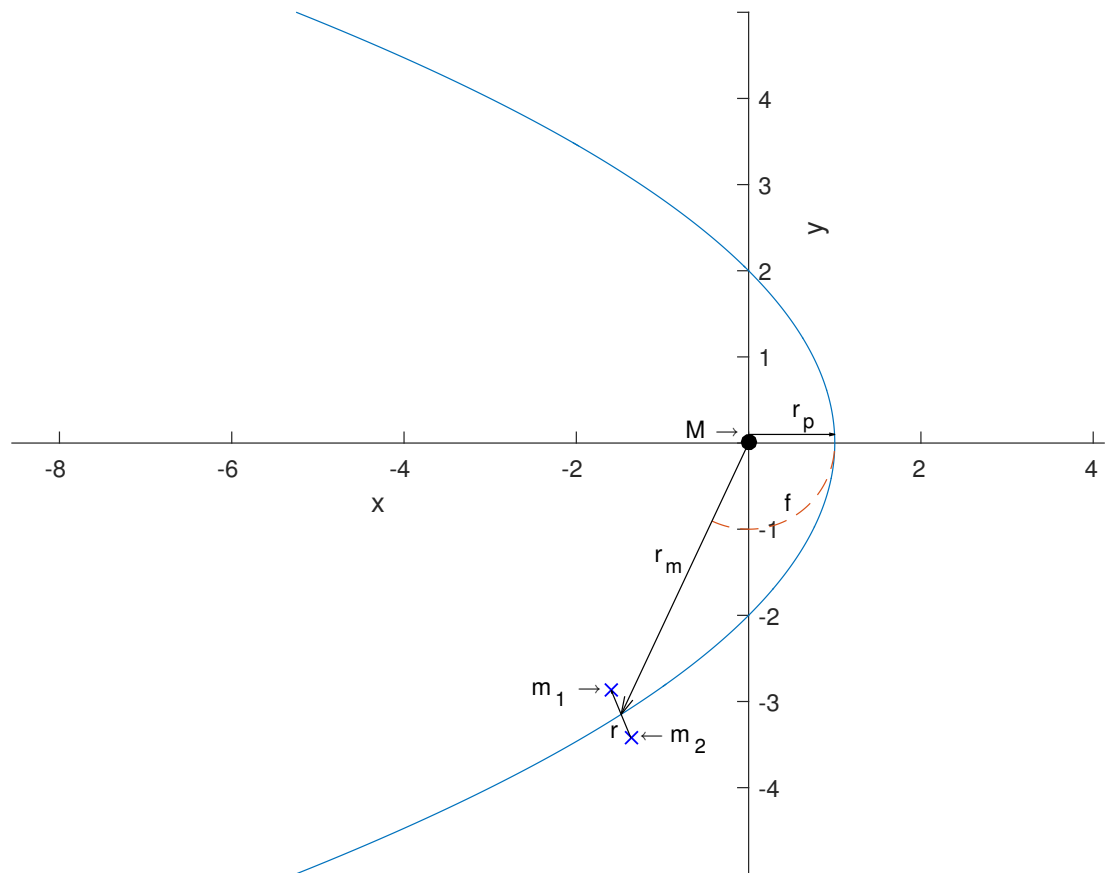


Figure 2.1: Layout of objects in a 3 body interaction with a binary star system (blue crosses) on a parabolic orbit (blue line) around a black hole (black dot at $(0, 0)$) with instantaneous distance from the central mass of r_m and binary separation of r . The axes are scaled to the distance of closest approach (r_p).

$$\frac{d^2 \mathbf{r}_1}{dt^2} = -\frac{Gm_2}{|\mathbf{r}_1 - \mathbf{r}_2|^3}(\mathbf{r}_1 - \mathbf{r}_2) - \frac{GM}{|r_1|^3}\mathbf{r}_1, \quad (2.12)$$

$$\frac{d^2 \mathbf{r}_2}{dt^2} = -\frac{Gm_1}{|\mathbf{r}_1 - \mathbf{r}_2|^3}(\mathbf{r}_2 - \mathbf{r}_1) - \frac{GM}{|r_2|^3}\mathbf{r}_2, \quad (2.13)$$

where \mathbf{r}_1 and \mathbf{r}_2 are the positions of the primary and secondary binary components respectively in the black hole rest frame, while m_1 and m_2 are the component masses. Within the restricted 3 body problem I consider only the separation of the two stars with a time dependent potential induced by the black hole. In this way I define the position vector $\mathbf{r} = \mathbf{r}_1 - \mathbf{r}_2$

$$\begin{aligned} \frac{d^2 \mathbf{r}}{dt^2} &= -\frac{Gm}{|r|^3}\mathbf{r} - GM \left(\frac{\mathbf{r}_1}{|\mathbf{r}_1|^3} - \frac{\mathbf{r}_2}{|\mathbf{r}_2|^3} \right), \\ &= -\frac{Gm}{|r|^3}\mathbf{r} - GM \left(\frac{\mathbf{r}_m + \frac{m_2}{m}\mathbf{r}}{|\mathbf{r}_m + \frac{m_2}{m}\mathbf{r}|^3} - \frac{\mathbf{r}_m - \frac{m_1}{m}\mathbf{r}}{|\mathbf{r}_m - \frac{m_1}{m}\mathbf{r}|^3} \right), \end{aligned} \quad (2.14)$$

where \mathbf{r}_m is the position vector of the binary centre of mass in the black hole rest frame, which is defined by the initial total energy of the binary and is expressed as a Keplerian orbit. In my approximation $r_m \gg r$ so I neglect the second order and higher terms of r in the second term of the equation of motion.

$$\begin{aligned} \frac{d^2 \mathbf{r}}{dt^2} &= -\frac{Gm}{r^3}\mathbf{r} - GM \left[\frac{\mathbf{r}_m + \frac{m_2}{m}\mathbf{r}}{r_m^3} \left(1 - \frac{3m_2}{m} \frac{\mathbf{r} \cdot \mathbf{r}_m}{r_m^2} \right) \right. \\ &\quad \left. - \frac{\mathbf{r}_m - \frac{m_1}{m}\mathbf{r}}{r_m^3} \left(1 + \frac{3m_1}{m} \frac{\mathbf{r} \cdot \mathbf{r}_m}{r_m^2} \right) \right], \\ \frac{d^2 \mathbf{r}}{dt^2} &= -\frac{Gm}{r^3}\mathbf{r} - \frac{GM}{r_m^3}\mathbf{r} + \frac{3GM}{r_m^5}(\mathbf{r} \cdot \mathbf{r}_m)\mathbf{r}_m. \end{aligned} \quad (2.15)$$

Within my work I assume that the binary is always on a parabolic orbit as a binary injected towards the black hole from a sufficiently large distance will approximate to a zero energy orbit described by

$$\mathbf{r}_m = \frac{2r_p}{1 + \cos f} \begin{pmatrix} \cos f \\ \sin f \\ 0 \end{pmatrix}. \quad (2.16)$$

Here r_p is the distance between the black hole and binary centre of mass at the closest point in its orbit and f , known as the true anomaly, is the angle between \mathbf{r}_m and the point of closest approach. f is a function of time but analytically I can only express time as a function of f :

$$t = \frac{\sqrt{2}}{3} \sqrt{\frac{r_p^3}{GM}} \tan \frac{f}{2} \left(3 + \tan^2 \frac{f}{2} \right) \quad (2.17)$$

This relationship is derived by using conservation of angular momentum, $L = mr_m^2 \dot{f}$. Rescaling the distance unit by $(m/M)^{1/3} r_p$, the time unit by $\sqrt{r_p^3/GM}$, and the mass unit by m the equation of motion in this new unit system becomes:

$$\tilde{\mathbf{r}} = \left(\frac{\tilde{r}_p}{\tilde{r}_m} \right)^3 [-\tilde{\mathbf{r}} + 3(\tilde{\mathbf{r}} \cdot \hat{\mathbf{r}}_m) \hat{\mathbf{r}}_m] - \frac{\tilde{\mathbf{r}}}{\tilde{r}^3}, \quad (2.18)$$

where the tilde indicates a unit that has been rescaled and a hat indicates a unit vector. This solution is then separated into three equations for x , y , and z and a final one for the evolution of f derived from the conservation of angular momentum.

$$\tilde{\ddot{x}} = -\frac{(1 + \cos f)^3}{8} [\tilde{x} - 3(\tilde{x} \cos f + \tilde{y} \sin f) \cos f] - \frac{\tilde{x}}{\tilde{r}^3}, \quad (2.19)$$

$$\tilde{\ddot{y}} = -\frac{(1 + \cos f)^3}{8} [\tilde{y} - 3(\tilde{x} \cos f + \tilde{y} \sin f) \sin f] - \frac{\tilde{y}}{\tilde{r}^3}, \quad (2.20)$$

$$\tilde{\ddot{z}} = -\frac{(1 + \cos f)^3}{8} \tilde{z} - \frac{\tilde{z}}{\tilde{r}^3}, \quad (2.21)$$

$$\dot{f} = \frac{\sqrt{2}(1 + \cos f)^2}{4}. \quad (2.22)$$

The energy of one of the binary partners is calculated as follows:

$$E_1 = \frac{1}{2} m_1 v_1^2 - \frac{GMm_1}{r_1} - \frac{Gm_2 m_1}{r}, \quad (2.23)$$

however as shown in section 2.1 the energy gained from the disruption is of the order of $(M/m)^{1/3}$ larger than the binding energy, so I can neglect the third term from eq. 2.23 and consider the energy rewritten in terms of the relative position and velocity of

binary partners to the binary centre of mass,

$$\begin{aligned}
E_1 &= \frac{1}{2}m_1 \left| \mathbf{v}_m + \frac{m_2}{m}\mathbf{v} \right|^2 - \frac{GMm_1}{\left| \mathbf{r}_m + \frac{m_2}{m}\mathbf{r} \right|}, \\
&\approx \frac{1}{2}m_1 \left(v_m^2 + 2\frac{m_2}{m}\mathbf{v}_m \cdot \mathbf{v} \right) \\
&\quad - \frac{GMm_1}{r_m^2} \left(r_m - \frac{m_2}{m} \frac{\mathbf{r}_m \cdot \mathbf{r}}{r_m} \right), \\
&\approx \frac{m_1}{m}E_m + \frac{m_1m_2}{m}\mathbf{v}_m \cdot \mathbf{v} + \frac{GMm_1m_2}{mr_m^3}\mathbf{r}_m \cdot \mathbf{r}. \tag{2.24}
\end{aligned}$$

Within the parabolic approximation the orbital energy of the binary $E_m = 0$. Rescaling the position and time terms by the parabolic unit system the energy becomes

$$E_1 = \frac{GMm_1m_2}{mr_p} \left(\frac{m}{M} \right)^{\frac{1}{3}} \left(\frac{\tilde{r}_p^2}{\tilde{r}_m^2} \tilde{\mathbf{r}}_m \cdot \tilde{\mathbf{r}} + \frac{\tilde{\mathbf{v}}_m \cdot \tilde{\mathbf{v}}}{\tilde{r}_p} \right). \tag{2.25}$$

This leaves the energy of the primary in Cartesian coordinates:

$$\begin{aligned}
E_1 &= \frac{Gm_1m_2}{a} \left(\frac{M}{m} \right)^{\frac{1}{3}} \times \\
&\frac{1}{D} \left[\frac{(1 + \cos f)^2}{4} (x \cos f + y \cos f) + \frac{-\dot{x} \sin f + \dot{y} (1 + \cos f)}{\sqrt{2}} \right]. \tag{2.26}
\end{aligned}$$

Here D is the ratio of the closest approach distance and the tidal radius, known as the penetration depth $D = r_p/R_t$. Since the total energy of the system is zero the energy of the secondary body is simply the negative of the primary $E_2 = -E_1$. From the approximations made in section 2.1 I expect the term on the second line to be of the order of unity so I often report energies, that have been rescaled by $(Gm_1m_2/a)(M/m)^{1/3} \tilde{E}$. The energy of a star is of particular importance as it is one of the potential methods for determining if a binary has been disrupted. If a binary is disrupted, the energy of an individual star becomes constant as it is no longer interacting with its partner. This parallels the energy gained or lost due to disruption (ΔE).

The angular momentum of the primary star around the black hole \mathbf{L}_1 is calculated as

follows:

$$\begin{aligned}
\mathbf{L}_1 &= m_1(\mathbf{r}_1 \times \dot{\mathbf{r}}_1), \\
&= m_1 \left[\left(\mathbf{r}_m + \frac{m_2}{m} \mathbf{r} \right) \times \left(\dot{\mathbf{r}}_m + \frac{m_2}{m} \dot{\mathbf{r}} \right) \right], \\
&= m_1 \left[\mathbf{r}_m \times \dot{\mathbf{r}}_m + \frac{m_2}{m} \mathbf{r} \times \dot{\mathbf{r}}_m + \frac{m_2}{m} \mathbf{r}_m \times \dot{\mathbf{r}} + \frac{m_2^2}{m^2} \mathbf{r} \times \dot{\mathbf{r}} \right], \\
&= \frac{m_1}{m} \mathbf{L}_m + \Delta \mathbf{L}_1,
\end{aligned} \tag{2.27}$$

where $\mathbf{L}_m = m \mathbf{r}_m \times \dot{\mathbf{r}}_m$ is the angular momentum of the binary centre of mass, which is constant for a given orbit. Since \mathbf{r}_m and $\dot{\mathbf{r}}_m$ are perpendicular at $r_m = r_p$ and $v_m = \sqrt{2GM/r_m}$,

$$\mathbf{L}_m = \sqrt{2GMm^2r_p} \begin{pmatrix} 0 \\ 0 \\ 1 \end{pmatrix}. \tag{2.28}$$

$\Delta \mathbf{L}_1$ is the angular momentum change due to the internal angular momentum of the binary, which becomes constant after disruption. As in previous solutions I use the fact that $r_m \gg r$ and $\dot{r}_m \gg \dot{r}$ to neglect the final term giving,

$$\Delta \mathbf{L}_1 = \frac{m_1 m_2}{m} (\mathbf{r} \times \dot{\mathbf{r}}_m + \mathbf{r}_m \times \dot{\mathbf{r}}). \tag{2.29}$$

For the secondary star the change in angular momentum is $\Delta \mathbf{L}_2$, and the only difference is the signature of \mathbf{r} and $\dot{\mathbf{r}}$ meaning that $\Delta \mathbf{L}_2 = -\Delta \mathbf{L}_1$.

Assuming $\mathbf{r} \approx a$ and $\dot{\mathbf{r}} \approx \sqrt{Gm/a}$ and using the same instantaneous disruption model used previously when estimating ejection energy,

$$\begin{aligned}
\Delta L_1 &\approx \frac{m_1 m_2}{m} \left(a \sqrt{\frac{GM}{R_t}} + R_t \sqrt{\frac{Gm}{a}} \right), \\
&\approx \left(\frac{M}{m} \right)^{\frac{1}{3}} \sqrt{Gm^3 a}.
\end{aligned} \tag{2.30}$$

For shallow penetrations \mathbf{L}_m dominates over $\Delta\mathbf{L}_1$

$$\frac{L_m}{\Delta L_1} \approx \frac{\sqrt{2GMm^2r_p}}{\left(\frac{M}{m}\right)^{\frac{1}{3}} \sqrt{Gm^3a}} \approx \left(\frac{M}{m}\right)^{\frac{1}{3}} \sqrt{D}. \quad (2.31)$$

For penetration depths $D \gg (m/M)^{2/3}$, it can be said that $L_1 = (m_1/m)L_m$. From the angular momentum I can get the eccentricity of stellar orbits post disruption, one hyperbolic and one elliptical

$$e_1 = \sqrt{1 + \frac{2L_1^2 E_1}{m_1^3 G^2 M^2}}. \quad (2.32)$$

For shallow penetrations I substitute $(m_1/m)L_m$ and use the rescaled \tilde{E}_1

$$e_1 = \sqrt{1 + \frac{Gm_1m_2}{a} \left(\frac{M}{m}\right)^{\frac{1}{3}} \frac{(4GMm_1^2r_p)\tilde{E}_1}{m_1^3 G^2 M^2}}, \quad (2.33)$$

$$= \sqrt{1 + 4D \frac{m_2}{m} \left(\frac{m}{M}\right)^{\frac{1}{3}} \tilde{E}_1}, \quad (2.34)$$

$$\approx 1 + 2D \frac{m_2}{m} \left(\frac{m}{M}\right)^{\frac{1}{3}} \tilde{E}_1. \quad (2.35)$$

2.2.2 Radial Approximation

The formulation that has been explained here is appropriate for all penetration depths, however in the deepest penetration depths $D \ll 1$ I can further simplify the evolution of the orbit by describing it not as a parabolic orbit but as a radial orbit with the binary in freefall from infinity directly towards the black hole,

$$r_m = \left(\frac{9GMt^2}{2}\right)^{\frac{1}{3}} \begin{pmatrix} 1 \\ 0 \\ 0 \end{pmatrix}. \quad (2.36)$$

In this radial regime I use a different unit system where distance is scaled by a and time is scaled by $\sqrt{Gm/a^3}$ which I use to rescale equation 2.15, then substituting the

centre of mass location to give an equation of motion:

$$\ddot{\tilde{\mathbf{r}}} = \left(\frac{2}{9\tilde{t}^2} \right) [-\tilde{\mathbf{r}} + 3(\tilde{\mathbf{r}} \cdot \hat{\mathbf{r}}_m)\hat{\mathbf{r}}_m] - \frac{\tilde{\mathbf{r}}}{\tilde{r}^3}. \quad (2.37)$$

Since the unit vector of \mathbf{r}_m is unity in the X dimension and zero in all others the equation of motion separated into Cartesian coordinates becomes:

$$\ddot{\tilde{x}} = +\frac{4\tilde{x}}{9\tilde{t}^2} - \frac{\tilde{x}}{\tilde{r}^3}, \quad (2.38)$$

$$\ddot{\tilde{y}} = -\frac{2\tilde{y}}{9\tilde{t}^2} - \frac{\tilde{y}}{\tilde{r}^3}, \quad (2.39)$$

$$\ddot{\tilde{z}} = -\frac{2\tilde{z}}{9\tilde{t}^2} - \frac{\tilde{z}}{\tilde{r}^3}. \quad (2.40)$$

The energy given in the same way from equation 2.25 is

$$E_1 = \frac{Gm_1m_2}{a} \left(\frac{M}{m} \right)^{\frac{1}{3}} \times \left(\frac{2}{9} \right)^{\frac{2}{3}} \tilde{t}^{-\frac{4}{3}} (\tilde{x} + 3\tilde{t}\dot{\tilde{x}}), \quad (2.41)$$

where, as with the general case, $E_1 = -E_2$.

2.2.3 Free Solutions in the General Solution

As the binary approaches the black hole in deep penetrations the tidal forces become so dominant that the self-binding force becomes negligible and both stars travel on independent orbits acting only under the gravity of the black hole. In this regime I can obtain analytic solutions to the equations of motion by considering two near identical orbits with slightly changed initial conditions denoted by Δ . Since the equation of motion is a three dimensional second order differential equation there exist six independent solutions. In these independent solutions one orbit is parabolic with standard initial conditions (\mathbf{r}_m) and the other has only a single initial variable changed and all other variables identical (\mathbf{r}'_m). The solutions are constructed with a variation to a single condition; these conditions are:

- Variation of periapsis crossing time.

- Variation of the orbit's eccentricity.
- Variation of periapsis distance.
- Variation with a rotation of apsidal axis.
- Variation with a rotation around the apsidal axis.
- Variation with a rotation around the latus rectum.

In the discussion below, it is useful to use a new variable $N \equiv \tan(f/2)$ and relations $\sin f = 2N/(1 + N^2)$ and $\cos f = (1 - N^2)/(1 + N^2)$. I consider an orbit infinitesimally close to a parabolic orbit, and I will evaluate the separation between the orbits $(\Delta x, \Delta y, \Delta z)$ at a given time (i.e. the separation between two stars in the orbits). For a given time, the true anomaly of the former $f' = f + \Delta f$ is infinitesimally different from that (f) of the fiducial parabolic orbit. Ignoring the 2nd and higher order terms of Δf , I can show the following relations.

$$\sin f' \approx \sin f + \Delta f \cos f = \frac{2N + \Delta f(1 - N^2)}{1 + N^2}, \quad (2.42)$$

$$\cos f' \approx \cos f - \Delta f \sin f = \frac{(1 - N^2) - 2\Delta f N}{1 + N^2}, \quad (2.43)$$

$$N' \equiv \tan(f'/2) \approx N + (\Delta f/2)(1 + N^2). \quad (2.44)$$

- Variation of periapsis crossing time.

Considering two stars on identical parabolic orbits with different periapsis crossing time, the relative position can be thought of as the difference of two points on the same orbit separated by a constant small change in time $t' = t + \Delta t$. The change in the true anomaly Δf can be evaluated by using Eq. 2.22 or equivalently $\Delta f = \sqrt{2}(1 + N^2)^{-2}\Delta\tilde{t}$ where $\Delta\tilde{t}$ is the crossing time difference Δt in units of $\sqrt{r_p^3/GM}$. I can express the separation in terms of N .

$$\Delta x = r'_m \cos f' - r_m \cos f = -\frac{\sqrt{2}r_p N}{1 + N^2}\Delta\tilde{t}, \quad (2.45)$$

$$\Delta y = r'_m \sin f' - r_m \sin f = \frac{\sqrt{2}r_p}{1 + N^2}\Delta\tilde{t}, \quad (2.46)$$

$$\Delta z = 0, \quad (2.47)$$

where $r'_m \equiv 2r_p/(1 + \cos f') = r_p(1 + N'^2)$ and $r_m = r_p(1 + N^2)$. Expressing these back in terms of f ,

$$\begin{pmatrix} \Delta x \\ \Delta y \\ \Delta z \end{pmatrix} \propto \begin{pmatrix} -\sin f \\ 1 + \cos f \\ 0 \end{pmatrix}. \quad (2.48)$$

By substituting $\mathbf{r} = (-\sin f, 1 + \cos f, 0)$ into the equation of motion, it is easy to show that this is a solution when the binary self-gravity term is negligible.

- Variation of the orbit's eccentricity.

Considering two stars on identical orbits, one parabolic and one with eccentricity $e = 1 + \Delta e$, the relative position can be thought of as the difference between these two at the same point in time. Like with the solution based on variation in crossing time this introduces a change in true anomaly Δf , I pick points at equal time: $t = \mathcal{K}(N, e, R_p) = \mathcal{K}(N', e', R_p)$. I start by considering the form of this altered orbit:

$$r'_m = \frac{(1 + e)R_p}{1 + e \cos(f')} = R_p(1 + N'^2) \left(1 + N'^2 \frac{\Delta e}{2}\right), \quad (2.49)$$

I can derive my \mathcal{K} function based on conservation of angular momentum,

$$h' = r_m'^2 \frac{df'}{dt} = r_m'^2 \frac{df'}{dN'} \dot{N}', \quad (2.50)$$

Considering the orbital-energy-invariance equation $v_m = \sqrt{GM(2/r_m - 1/a)}$, where $a = R_p/(1 - e)$, the specific angular momentum at the periastron $h' \approx \sqrt{2GM R_p(1 + \Delta e/4)}$. I rewrite the conservation of the angular momentum as

$$\mathcal{K}(N', e', R_p) = \sqrt{\frac{2R_p^3}{GM}} \left[N' + \frac{N'^3}{3} + \Delta e \left(-\frac{N'}{4} + \frac{N'^3}{4} + \frac{N'^5}{5} \right) \right]. \quad (2.51)$$

This equation gives the time as a function of N' (or equivalently f') for a given set of the parameters Δe and R_p . For a given time t , f and f' are slightly different

because the two orbits have different eccentricity. Equalizing the time for the two orbits $\mathcal{K}(N', e', R_p) = \mathcal{K}(N, e, R_p)$, I obtain

$$\Delta f = \frac{N(5 - 5N^2 - 4N^4)}{10(1 + N^2)^2} \Delta e. \quad (2.52)$$

Now I can evaluate the separation,

$$\begin{aligned} \Delta x &= R_p(1 + N^2) \left(\Delta f(N \cos(f) - \sin(f)) + \Delta e \frac{N^2}{2} \cos(f) \right), \\ &= \frac{R_p \Delta e N^4}{10(1 + N^2)^2} (5 + 4N^2 - N^4). \end{aligned} \quad (2.53)$$

$$\begin{aligned} \Delta y &= R_p(1 + N^2) \left(\epsilon(N \sin(f) + \cos(f)) + \Delta e \frac{N^2}{2} \sin(f) \right), \\ &= \frac{R_p \Delta e N}{10(1 + N^2)} (5 + 5N^2 + 6N^4). \end{aligned} \quad (2.54)$$

Expressing displacement in terms of the true anomaly, I get:

$$\begin{pmatrix} \Delta x \\ \Delta y \\ \Delta z \end{pmatrix} \propto \begin{pmatrix} (8 + 12 \cos(f)) \tan^4(f/2) \\ \frac{35 \sin(f) - 2 \sin(2f) + 3 \sin(3f)}{(1 + \cos(f))^2} \\ 0 \end{pmatrix}. \quad (2.55)$$

- Variation of periapsis distance.

In this solution the varied orbit remains parabolic with a changed periastron distance. Consider two similar orbits with slightly changed periastron distance $R'_p = R_p + \Delta R_p$, with an associated change in the true anomaly Δf . This change in the true anomaly is obtained in a similar method to the variation of eccentricity method where $t = \mathcal{K}(N, e, R_p) = \mathcal{K}(N', e, R'_p)$ giving:

$$\Delta f = \frac{-\Delta R_p}{2R_p} \sin(f)(2 + \cos(f)), \quad (2.56)$$

which I can substitute into the relative position

$$\Delta x = R_p(1 + N^2) \left[\frac{\Delta R_p}{R_p} \cos(f) - \Delta f N \right], \quad (2.57)$$

$$\Delta y = R_p(1 + N^2) \left[\frac{\Delta R_p}{R_p} \sin(f) + \Delta f \right]. \quad (2.58)$$

Finally giving a displacement of:

$$\begin{pmatrix} \Delta x \\ \Delta y \\ \Delta z \end{pmatrix} \propto \begin{pmatrix} (2 - \cos(f)) \\ \cos(f) \tan\left(\frac{f}{2}\right) \\ 0 \end{pmatrix}. \quad (2.59)$$

- Variation with a rotation of apsidal axis.

In this solution I compare my parabolic orbit with an identical orbit that has been rotated around the focus on the X-Y plane by a small angle $\Delta\omega$

$$\mathbf{r}'_m = \begin{bmatrix} 1 & -\Delta\omega & 0 \\ \Delta\omega & 1 & 0 \\ 0 & 0 & 1 \end{bmatrix} \mathbf{r}_m, \quad (2.60)$$

$$\begin{pmatrix} \Delta x \\ \Delta y \\ \Delta z \end{pmatrix} \propto \begin{pmatrix} \frac{\sin(f)}{1 + \cos(f)} \\ \frac{\cos(f)}{1 + \cos(f)} \\ 0 \end{pmatrix}. \quad (2.61)$$

- Variation with a rotation around the apsidal axis.

In this solution I again rotate but this time around the apsidal line (i.e. the X axis) by a small angle $\Delta\omega$. This introduces a z component to the parabolic equation which previously has been set to zero.

$$\mathbf{r}'_m = \begin{bmatrix} 1 & 0 & 0 \\ 0 & 1 & -\Delta\omega \\ 0 & \Delta\omega & 1 \end{bmatrix} \mathbf{r}_m, \quad (2.62)$$

$$\begin{pmatrix} \Delta x \\ \Delta y \\ \Delta z \end{pmatrix} \propto \begin{pmatrix} 0 \\ 0 \\ \frac{2 \sin(f)}{1 + \cos(f)} \end{pmatrix}. \quad (2.63)$$

- Variation with a rotation around the latus rectum.

The final solution is a rotation around the latus rectum line (the Y axis), which also introduces a Z component.

$$\mathbf{r}'_m = \begin{bmatrix} 1 & 0 & \Delta\omega \\ 0 & 1 & 0 \\ -\Delta\omega & 0 & 1 \end{bmatrix} \mathbf{r}_m, \quad (2.64)$$

$$\begin{pmatrix} \Delta x \\ \Delta y \\ \Delta z \end{pmatrix} \propto \begin{pmatrix} 0 \\ 0 \\ \frac{2 \cos(f)}{1 + \cos(f)} \end{pmatrix}. \quad (2.65)$$

2.2.4 The t=0 Singularity in the Radial solution

In order to use the radial solution as an approximation for very deep penetrating binaries in the general case I must be able to fully simulate the orbit of the binary into positive times. However in the radial solution I cannot evolve the binary through the periastron with the standard reduced equations of motion. The nature of the radial solution leads to r_m becoming zero at $t = 0$ causing the separation between the stars become infinite. I can remove this problem by relying on free solutions to navigate through the minimum separation into positive times.

As with the general solution as I approach $t = 0$ the self-binding forces in the binary become negligible and the equations of motion for each spatial dimension become dependent only on the dimension itself and time, allowing us to solve the differential,

$$\ddot{\tilde{x}} = \frac{4\tilde{x}}{9\tilde{t}^2}, \quad (2.66)$$

which is satisfied by a power law $\tilde{x} \propto \tilde{t}^n$ where the value of n can be shown to be $4/3$ and $-1/3$,

$$\tilde{x} = A_x \tilde{t}^{-\frac{1}{3}} + B_x \tilde{t}^{\frac{4}{3}}. \quad (2.67)$$

Here A_x and B_x are coefficients of integration, likewise y and z have similar equations of motion

$$\tilde{y} = A_y \tilde{t}^{\frac{1}{3}} + B_y \tilde{t}^{\frac{2}{3}}, \quad (2.68)$$

$$\tilde{z} = A_z \tilde{t}^{\frac{1}{3}} + B_z \tilde{t}^{\frac{2}{3}}, \quad (2.69)$$

Since at this distance from the black hole interaction between the stars is negligible on this time-scale, the coefficients are constant, so the velocity of the star is given using the free solution as:

$$\dot{\tilde{x}} = -\frac{1}{3}A_x \tilde{t}^{-\frac{4}{3}} + \frac{4}{3}B_x \tilde{t}^{-\frac{1}{3}}, \quad (2.70)$$

$$\dot{\tilde{y}} = \frac{1}{3}A_y \tilde{t}^{-\frac{2}{3}} + \frac{2}{3}B_y \tilde{t}^{-\frac{1}{3}}, \quad (2.71)$$

$$\dot{\tilde{z}} = \frac{1}{3}A_z \tilde{t}^{-\frac{2}{3}} + \frac{2}{3}B_z \tilde{t}^{-\frac{1}{3}}. \quad (2.72)$$

The values of the coefficients are given by:

$$A_x = \frac{4\tilde{x}}{5} \tilde{t}^{\frac{1}{3}} - \frac{3\dot{\tilde{x}}}{5} \tilde{t}^{\frac{4}{3}}, \quad (2.73)$$

$$B_x = \frac{\tilde{x}}{5} \tilde{t}^{-\frac{4}{3}} - \frac{3\dot{\tilde{x}}}{5} \tilde{t}^{-\frac{1}{3}}, \quad (2.74)$$

$$A_y = 2\tilde{y} \tilde{t}^{-\frac{1}{3}} - 3\dot{\tilde{y}} \tilde{t}^{\frac{2}{3}}, \quad (2.75)$$

$$B_y = -\dot{\tilde{y}} \tilde{t}^{-\frac{2}{3}} + 3\tilde{y} \tilde{t}^{\frac{1}{3}}, \quad (2.76)$$

$$A_z = 2\tilde{z} \tilde{t}^{-\frac{1}{3}} - 3\dot{\tilde{z}} \tilde{t}^{\frac{2}{3}}, \quad (2.77)$$

$$B_z = -\dot{\tilde{z}} \tilde{t}^{-\frac{2}{3}} + 3\tilde{z} \tilde{t}^{\frac{1}{3}}. \quad (2.78)$$

It can be seen from these solutions that although the binary separates at $t = 0$ it later returns in positive times. As the coefficients are constant so long as the binding force is negligible I can obtain the conditions of the binary in positive time by simply changing the signature of time in the free solutions.

These coefficients in the radial free solutions can be linked to the coefficients in the general free solutions. As the penetration depth approaches zero ($D \ll 1$) and the orbit becomes radial, in essence a straight line towards the black hole, the true anomaly is $-\pi$ for the entirety of the orbit up until $t = 0$ when it rapidly makes a full 2π rotation. I can compare the two solutions by expanding around $f = -\pi + \Delta f$. Time can be shown as a function of Δf

$$\tilde{t} = \frac{\sqrt{2}}{3} D^{\frac{3}{2}} \tan\left(\frac{-\pi + \Delta f}{2}\right) \left(3 + \tan^2\left(\frac{-\pi + \Delta f}{2}\right)\right), \quad (2.79)$$

$$\Delta f = -\left(\frac{128}{9}\right)^{\frac{1}{6}} D^{\frac{1}{2}} \tilde{t}^{-\frac{1}{3}}. \quad (2.80)$$

Considering the solution with respect to variation in crossing time, the general free solution when expanded around $-\pi + \Delta f$ has the same time dependency as the A_x term in the radial free solution

$$\Delta x = -\sin(-\pi + \Delta f) \approx \Delta f \propto \tilde{t}^{-\frac{1}{3}}. \quad (2.81)$$

In the same manner each of the five other coefficients of the radial free solutions can be linked to the general free solutions: B_x is linked to solution for a variation in orbital eccentricity (Eq. 2.55), A_y is linked to the solution for variation in periastron distance (Eq. 2.59), B_y is linked to the solution for a rotation in apsidal axis (Eq. 2.61), A_z is linked to the solution for a rotation around the apsidal axis (Eq. 2.63), and B_z is linked to the solution for a rotation around the latus rectum (Eq. 2.65).

In deep penetrations, in the general case as well as the radial case, the final energy and position accurately reproduce those of the full 3 body integration, however the motions of the stars during the periapsis of their orbits are not recreated. In deep penetrations the approximation causes binary partners to separate substantially as they approach the periastron (Fig. 2.2), however they do later return to the same path as that of the full 3 body integration.

In the radial free solutions as $|t| \ll 1$ the A_x term dominates over all others causing the separation of binary members. It can be shown that the same term dominates in

the general case as well, as the paths of the binary members in deep penetrations of the general case follow the free solution for variation in time (Fig. 2.3), however the 3 body solution does not follow the free solution exactly. This effect is due to the approximation treating the stars as test particles. Increasing the mass of the black hole in the 3 body case results in an orbit similar to the restricted case however as the subject of this study is focused on interactions in our own Galactic centre the black hole mass can always be taken as $M \gg m$.

To navigate the radial case across $t = 0$ using the radial solution I need to select a value of t , T_{min} , where it becomes acceptable to neglect the self gravity. In my scaled unit system it is simple to approximate the range of T_{min} . From the radial free solutions (Eq. 2.67, 2.68, & 2.69) I know that as $t \rightarrow 0$, $r \rightarrow x \rightarrow A_x t^{-1/3}$. The criterion to enter the free solution is therefore taken from the radial equation of motion: $t \ll A_x$. Since A_x is of the order of unity the requirement becomes simply $t \ll 1$. I have tested ranges of T_{min} (Fig. 2.4) to find the most effective value for future use. As the time step of integration is scaled based on the dominant dynamical timescale, a smaller T_{min} can become computationally expensive over multiple simulations. I therefore want to choose a value as large as is feasible while still maintaining numerical accuracy. Based on these tests I have determined that $T_{min} = 10^{-5}$ results in a fractional difference of less than 0.01 while keeping computation time down.

2.2.5 Time step scaling

In the restricted three body solution there are two dynamical timescales to consider: the binary orbital timescale $T_r = \sqrt{r^3/Gm}$ which scales to $\tilde{r}^{3/2}$ and the outer orbit timescale $T_m = \sqrt{r_m^3/GM}$ which scales to $(2/(1 + \cos f))^{3/2}$ in the general case, and $\sqrt{9/2\tilde{t}}$ in the radial case. The timesteps in the integration are scaled to these values with $\Delta t = 10^{-5} \times \min(T_r, T_m)$ to maintain accuracy. This scaling is accurate for both eccentric and circular binaries. The fractional difference in ejection energy for circular and eccentric binaries integrated with base time step 10^{-5} and binaries integrated with smaller time steps are less than 0.1% for timesteps an order of magnitude smaller.

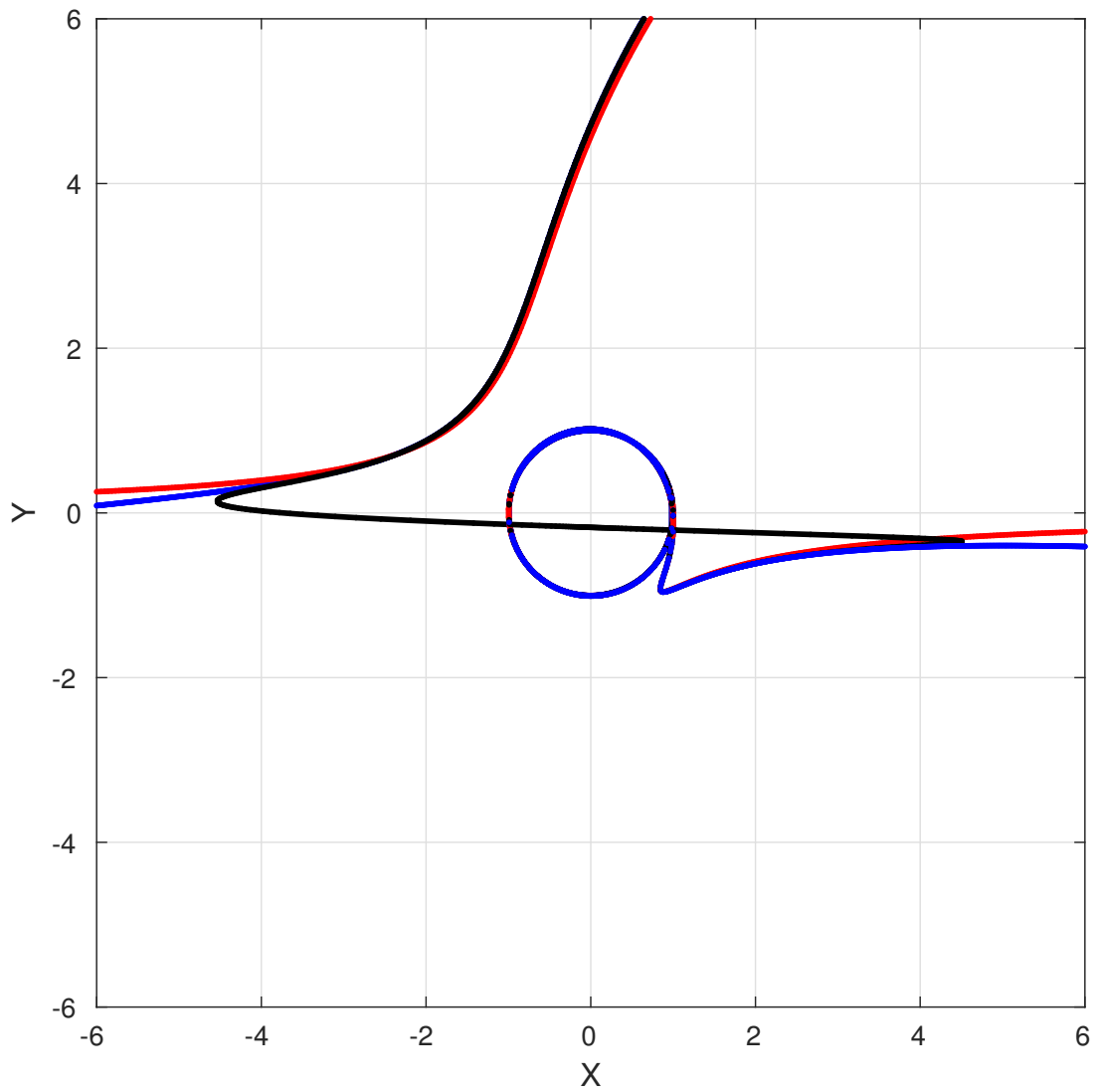


Figure 2.2: The path of the primary star's orbit relative to its partner integrated from the same initial conditions using the full 3 body model (black), the restricted general case (blue), and the restricted radial case (red). The penetration depth of the three body and general cases is set as 10^{-5} , the black hole mass in the 3 body case is set to $2 \times 10^6 m$ and binary phase at periastron is 0.0. The distance is scaled to the initial separation a .

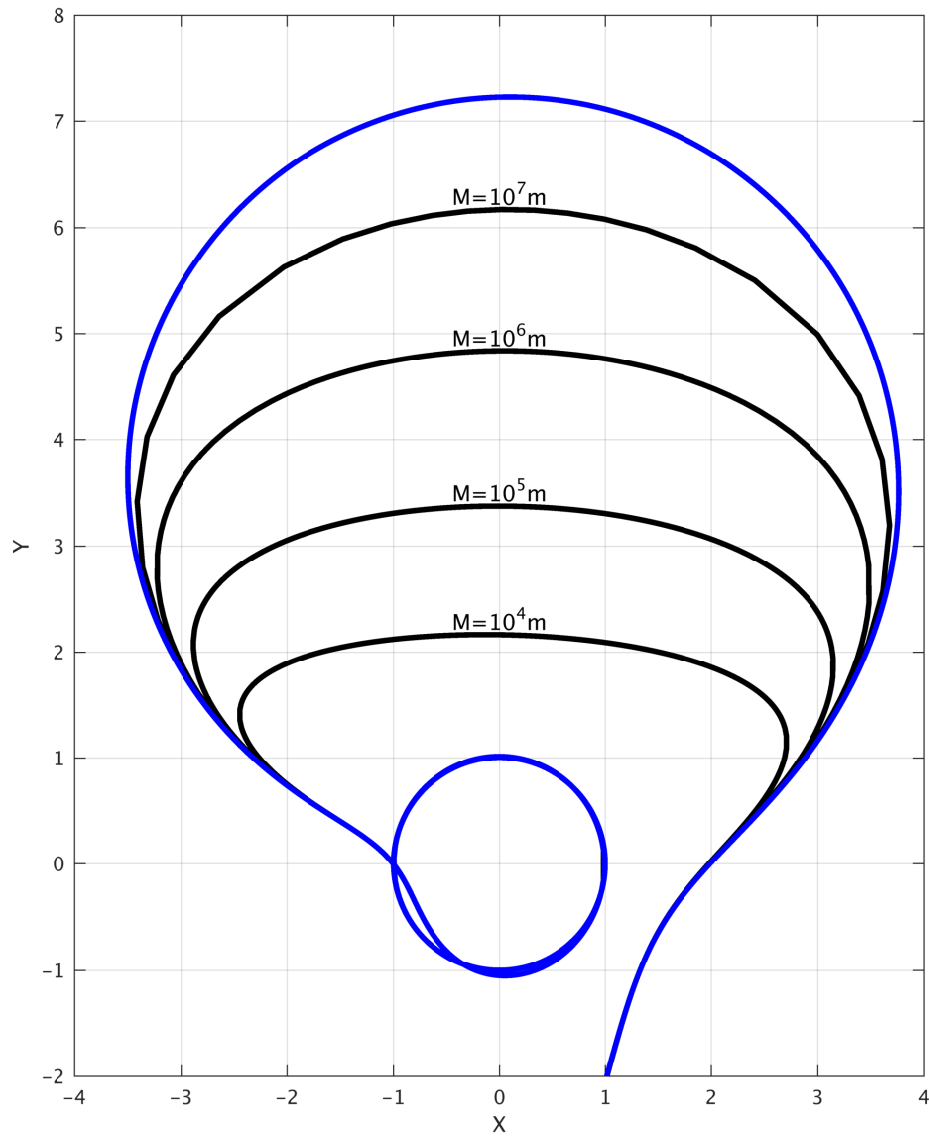


Figure 2.3: The path of the primary star's orbit relative to its partner integrated from the same initial conditions using the full 3 body model (black) and the restricted general case (blue) with penetration depth $D = 10^{-2}$ and binary phase at periastron of 0.5π in a co-planar prograde orbit. The full 3 body model is integrated using a range of different black hole masses. The restricted general case has the same form as the free solution for variation in time.

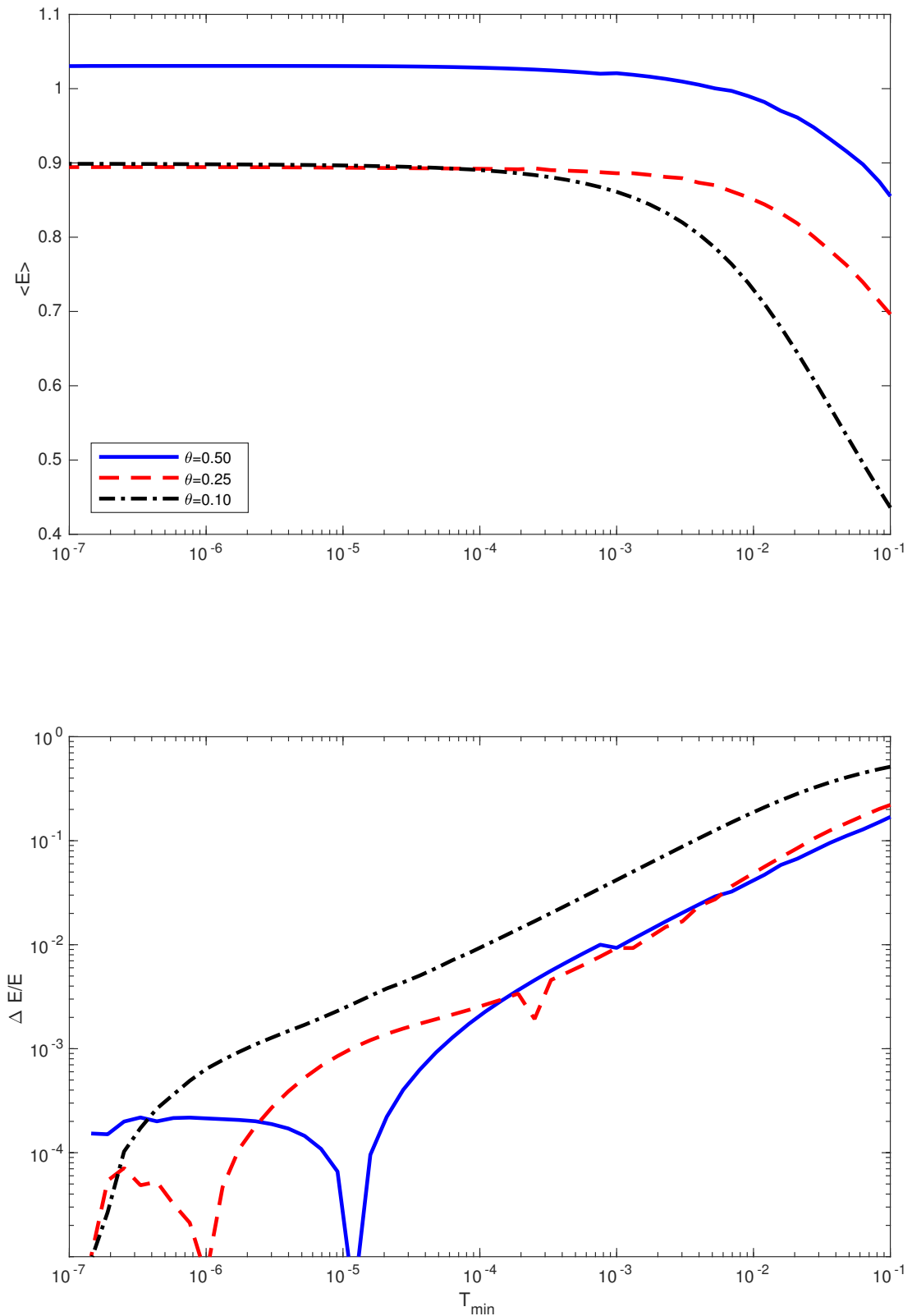


Figure 2.4: Top: The mean ejection energy of stars in the radial case with $\theta = 0.50\pi$, 0.25π , 0.10π in blue solid, dashed red, and dot-dashed black respectively, in units of $Gm_1m_2/a(M/m)^{1/3}$ as a function of the T_{min} . Bottom: The fractional difference in mean energy between $E(T_{min})$ and $E(T_{min} = 10^{-7})$ with $\theta = 0.50\pi$, 0.25π , 0.10π in blue solid, dashed red, and dot-dashed black respectively.

2.3 Initial Conditions

2.3.1 General Case

Within the restricted 3 body problem I have rescaled factors to reduce the parameter space required to fully sample the spectrum of different initial conditions. In this way the results of a single given integration are applicable to any different combination of masses and separations. As such the only conditions I need consider when choosing initial conditions of a circular binary in the general case are: The penetration depth D , the phase of the binary ϕ , and the orientation of the binary defined in polar space by the angular momentum vector with inclination from the positive X axis θ and the azimuthal angle from the positive Y axis φ (Fig. 2.7).

I can restrict the range of binary phase angles that need to be considered by recognizing the symmetry of the binary system. In a circular binary of equal mass the two stars are displaced around the centre of mass by π radians and so a rotation π results in an identical binary. Likewise within my approximation the only effect of rotation is a change in signature of E_1 , that is to say that in the case where the primary is bound to the black hole while its partner is ejected a rotation of initial binary phase of π would result in the secondary being bound while the primary is ejected. In this way I can restrict the range of binary phase angles to $0 \leq \phi < \pi$ which are sampled in an equal distribution. In my approximation where $a \ll r_m$ the offset of the binary centre of mass in an unequal mass binary is not a factor when considering only the first order terms, therefore a rotation of π produces an identical negative result to the equation of motion and energy (Eqn. 2.18, 2.26). Because of this the symmetry in binary phase is valid for all mass ratios. This does not hold for eccentric binaries where a rotation of π can result in a different binary separation and cannot be sampled in an equal distribution as angular velocity is not constant.

I consider 3 different techniques for sampling orientation angles. The first is a Monte Carlo random sample generated using pairs of randomly generated numbers u, v between 0 and 1 that produce orientation angles $\theta = \cos^{-1}(2u-1)$ and $\varphi = 2\pi v$. The sec-

ond method uses the same distribution as the Monte Carlo sample but using a regular distribution instead of random, choosing rings of equal θ with $d\theta = \cos^{-1}(\theta)$ between 0 and π and populating those rings with points with azimuthal angle φ equally distributed between 0 and 2π . The third is based on the method by Deserno (2004) where points are distributed on a sphere approximately equidistant from their neighbouring points. This is done in concept by dividing the surface of a sphere into approximately equal squares and placing a point in the centre of each.

I start by deciding the number of points required N , and given that the surface area of a unit sphere is 4π , each square has area $A = 4\pi/N$ with angular length on each edge of $d = \sqrt{A}$. I then divide the sphere into rings of equal θ , the number of rings is $N_\theta = \pi/d$ with angular displacement $d_\theta = \pi/N_\theta$. On each ring of equal θ I then populate it with points equally separated in azimuthal angle φ , with approximate separation $d_\varphi = A/d_\theta$.

To test the efficacy of the three sampling methods at producing an equal distribution I compare the distribution with different sample size N . Then to judge the accuracy of the distribution I consider each orientation angle as a point on the surface of a unit sphere, defining \bar{s} as the average distance between a specific point on a unit sphere and the points generated by my methods. In a perfect distribution this value is known and derived in the following way (also see Fig. 2.5):

$$\bar{s} = \frac{1}{N} \sum_{i=1}^N (s_i), \quad (2.82)$$

$$= \frac{1}{N} \sum_{i=1}^N \left(2 \sin \left(\frac{\theta_i}{2} \right) \right). \quad (2.83)$$

$N = 4\pi n$ where n is a constant surface area number density. In a ring on the sphere with inclination α from a specific point with thickness $d\alpha$ the number of points $N_\alpha = 2\pi n \cos(\alpha) d\alpha$. All points within this ring have the same s therefore,

$$\begin{aligned}
\bar{s} &= \int_0^\pi \sin\left(\frac{\theta}{2}\right) \cos(\theta) d\theta, \\
&= 2 \int_0^\pi \sin^2\left(\frac{\theta}{2}\right) \cos\left(\frac{\theta}{2}\right) d\theta, \\
&= 4 \int_0^{\frac{\pi}{2}} \sin^2(\tau) \cos(\tau) d\tau, \\
&= \frac{4}{3}.
\end{aligned} \tag{2.84}$$

For each of my distributions I take a point at each of end of the cartesian axis ($[1, 0, 0]$, $[-1, 0, 0]$, $[0, 1, 0]$, $[0, -1, 0]$, $[0, 0, 1]$, $[0, 0, -1]$) and take the $\bar{s} = 4/3$ of each. The average for each of these is given in Fig. 2.6 with increasing sample size. The Deserno (2004) method is more accurate for all sample sizes. While both the regular and Deserno methods work in principle by having each point describing an equal area, the dimensions of that area are not constant in the regular method. In the Deserno method each point occupies a square of equal height and width, but in the regular method points around $\theta = 0$ and $\theta = \pi$ are very tall but narrow, while points around $\theta \approx \pi/2$ are very wide but short. This makes it less efficient for sampling orientations.

I am also able to limit the range of binary orientation angle θ in the same way as the binary phase can be limited by recognizing another symmetry in the system. Since in the general case the black hole is always located on the X - Y plane the only effect of changing the signature of the z component to the equation of motion 2.18 is a change in signature of the \dot{z} component Eq. 2.21. In this way for every initial orientation there is a mirror orientation with only the signature of the z component changed (see the dashed lines on Fig. 2.7). Since the angular momentum vector is defined as $\hat{l}(\theta, \varphi) = (\cos \theta, \sin \theta \cos \varphi, \sin \theta \sin \varphi)$ the orientation that produces the mirrored orientation is $\hat{l}(\pi - \theta, \pi - \varphi)$. Therefore it is possible to limit the range of orientation angles such that $0 \leq \theta \leq \pi/2$ and $0 < \varphi < 2\pi$. Within my simulations I do not use this limiting method as within the Deserno sampling method there is no loss or gain in accuracy by limiting my range.

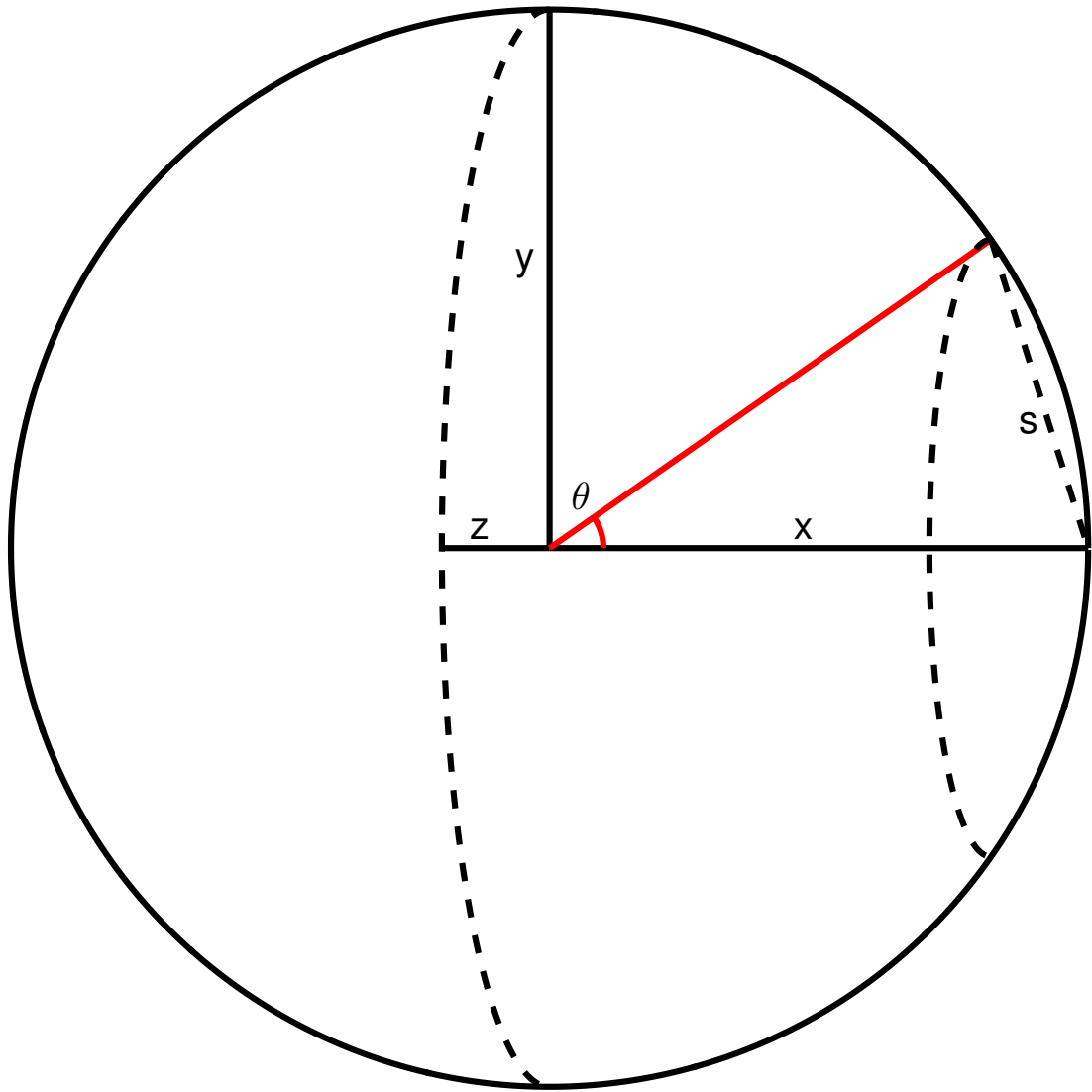


Figure 2.5: Diagram describing the derivation of mean separation of points randomly distributed on the surface of a sphere.

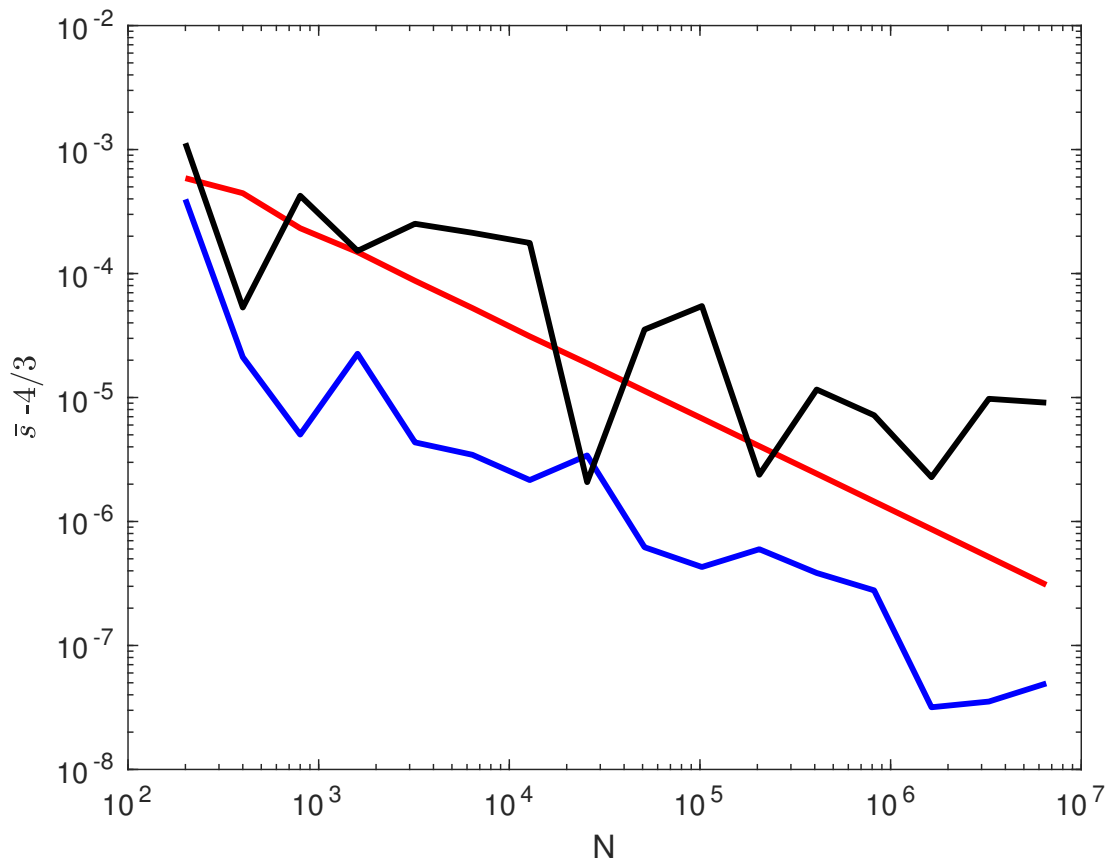


Figure 2.6: The difference between the mean distance to points generated vis the three orientation sampling methods and the mean distance obtained from a perfect distribution. The Monte Carlo method is shown in black, the regular distribution method is shown in red, and the Deserno (2004) method shown in blue.

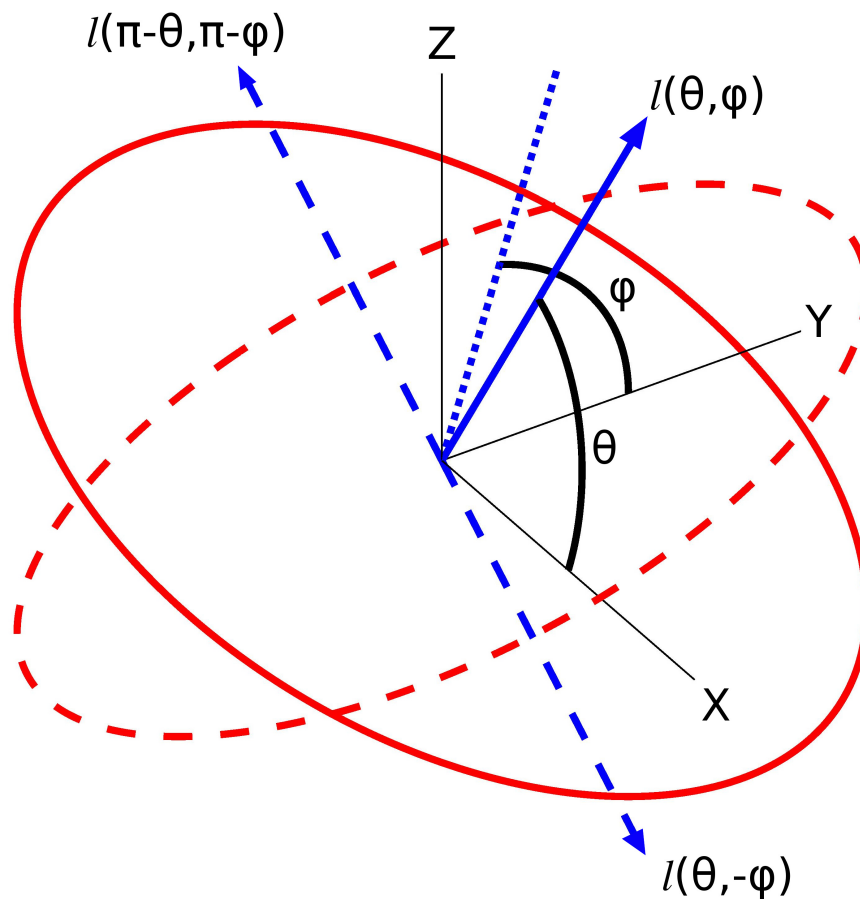


Figure 2.7: The initial circular orbit of a binary (red solid line) and its angular momentum vector (blue solid arrow) with its projection (blue dotted line) on the Y - Z plane. The binary itself orbits the MBH on a parabolic orbit on the X - Y plane. The red dashed line indicates another circular orbit which is symmetric to the red solid orbit with respect to the X - Y plane. The two blue dashed arrows are the angular momenta of the same (red dashed) orbit but one orbiting in the prograde direction and the other in the retrograde.

In the case of binaries with an initial eccentricity the initial conditions for binary orientation are described differently. Along with ϕ angle there is an additional factor, the angle describing the position of the periapsis of the eccentric orbit relative to the X axis before the binary is rotated by the orientation angles: ϖ . In an eccentric orbit the angular velocity is not constant, and because of this ϕ can not be sampled linearly between 0 and 2π . To produce a sample I attempt to derive ϕ as a function of t using Kepler's laws.

$$\frac{dA}{dt} = \text{constant} = \frac{\pi ab}{T}, \quad (2.85)$$

where dA is an area swept out by a line connecting the star to its centre of orbit, a is the semi-major axis, b is the semi minor axis and T is the orbital period.

$$\frac{1}{2}r^2(\phi)d\phi = \frac{\pi ab}{T}dt, \quad (2.86)$$

$$\frac{1}{2} \left(\frac{a(1-e^2)}{(1+e\cos\phi)} \right)^2 d\phi = \frac{\pi a^2 \sqrt{1-e^2}}{T} dt, \quad (2.87)$$

$$\frac{1}{(1+e\cos\phi)^2} d\phi = \frac{2\pi(1-e^2)^{-\frac{3}{2}}}{T} dt. \quad (2.88)$$

There is no trivial solution to this differential so instead I must solve it numerically. In essence I integrate a through a single orbital period using the Euler method with equal spaced time intervals.

$$\Delta\phi = 2\pi \frac{(1+e\cos\phi)^2}{(1-e^2)^{\frac{3}{2}}} \frac{\Delta t}{T}, \quad (2.89)$$

$$\Delta\phi = \frac{2\pi}{N_\phi} \frac{(1+e\cos\phi)^2}{(1-e^2)^{\frac{3}{2}}}, \quad (2.90)$$

which generates a sample $\phi_{i+1} = \phi_i + \Delta\phi(\phi_i)$.

As said before the symmetry between $0 < \phi < \pi$ and $\pi < \phi < 2\pi$ does not exist in elliptical orbits. However a similar symmetry exists with ϖ where a rotation of π while maintaining the same ϕ results in the same negative energy result as the original symmetry. Since ϖ is randomly oriented I can sample it equally distributed between

$0 \leq \varpi < \pi$. For the general case I model binaries with eccentricities $e = 0, 0.3, 0.6$ and 0.9 .

The last remaining variable to decide is penetration depth D which is decided separately from the other variables. While other initial conditions are sampled in a regular fashion or using a numerical method D is sampled only as needed to fully describe the range between D_{min} where the results can be described accurately by the radial solution, and D_{max} where the probability that a binary will undergo an exchange collision becomes 0. Within this range I specify points in a semi-logarithmic scale sufficient to produce continuous curves in all results.

In eccentric binaries, D is sampled in a regular equal distribution in log space in the range of $4 \times 10^{-5} < D < 4$. Due to limitations of computing time eccentric binaries are not simulated with full 3d orientations as the inclusion of ϖ and a full range of D make the simulations too computationally expensive. Instead they are simulated using co-planar orientations where both stars and black hole are located on the X - Y plane ($\theta = 0.5\pi, \varphi = 0.5\pi$). I run eccentric binaries with specific values of e similarly to how I sample D in the circular case.

In summary, I have shown three forms of symmetry in binaries' initial conditions. The first is in the binary phase of circular binaries where there is rotational symmetry of order one, as binaries rotated by π result in a change of signature of ejection energy as the bound and ejected stars switch places. This symmetry does not hold for eccentric binaries where instead the same form of symmetry is found in the rotation of the apsidal line. With orientation there is symmetry in the angular momentum when rotated about the Z -axis by π ; this rotation produced an identical result, with no change in bound-disruption state.

2.3.2 Radial Case

The radial case is simpler with regards to initial conditions as it is constructed such that $D = 0$. Since R_m in the radial case is always located on the X axis the system is

symmetric to rotation around the X axis. Because of this the orientations of binaries in the radial approximation are only dependent on θ . I sample θ as a regular equal distribution between 0 and $\pi/2$ and any averages taken over orientation are normalized by a factor of $\sin(\theta)$ to account for a 3D rotation around the X axis. For eccentric binaries the restriction of parameter space allows a more thorough exploration on e dependency, letting us sample eccentricity to a higher resolution. All other variables are sampled in the same manner as in the general case.

2.3.3 Kozai-Lidov Mechanism

In deciding on the distribution of orientations I need to consider the effect of perturbations from the black hole on the binary at large distances. Over timescales of the order of multiple binary orbits the inclinations and eccentricity shift due to what is known as the Kozai-Lidov (KL) mechanism (Kozai, 1962; Lidov, 1962). To test the potential effect of the KL mechanism on the distribution of orientations I run simulations using the full three-body equation of motion with a highly elliptical outer orbit with apoapsis $R_a = 1000R_t$. I integrate up to $r_m = 10R_t$, where I typically begin the simulations, and measure the change in orientation angle and eccentricity over time (Figs. 2.8 & 2.9), with the change in orientation angle α coming from $\mathbf{L}_0 \cdot \mathbf{L}(t) / |\mathbf{L}_0| |\mathbf{L}(t)| = \sin(\alpha)$.

The change in orientation stays below 10^{-2} radians throughout its orbit, and this is far below the resolution of orientations produced by my sampling method. Likewise the change in eccentricity is negligible during the early orbit.

Although the effect from the KL mechanism can be significant over multiple outer orbits this is not relevant to my work as I do not simulate binaries very far post periapsis, and with my penetration depths any change in orientation and eccentricity in a binary that survives its orbit is dominated by the effects of tidal forces during the periapsis of its orbit. I therefore can ignore the effect of the KL mechanism on my sample.

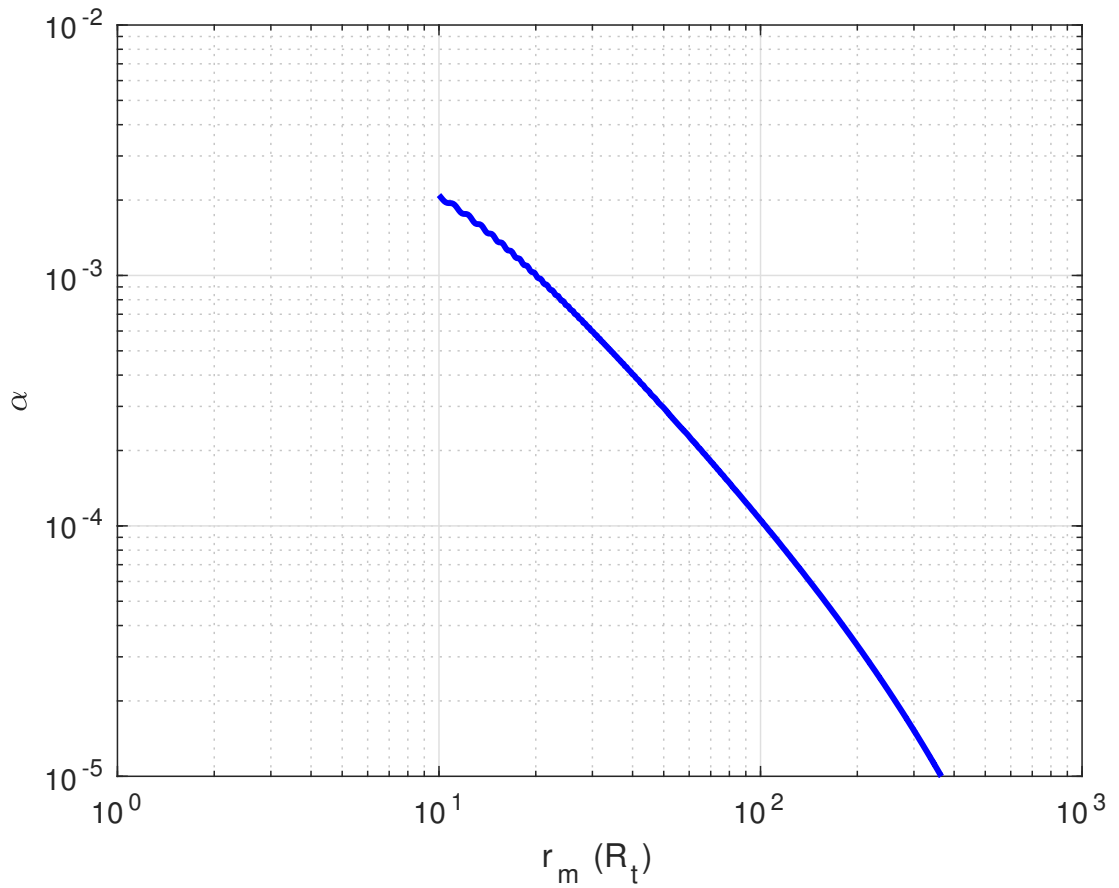


Figure 2.8: The angular change in binary orientation as it approaches the black hole using a full three body integration on a highly elliptical outer orbit with $R_p = R_t$, $R_a = 1000R_t$, $e = 0$, $\theta = 0.25\pi$, and $\phi = 0.5\pi$.

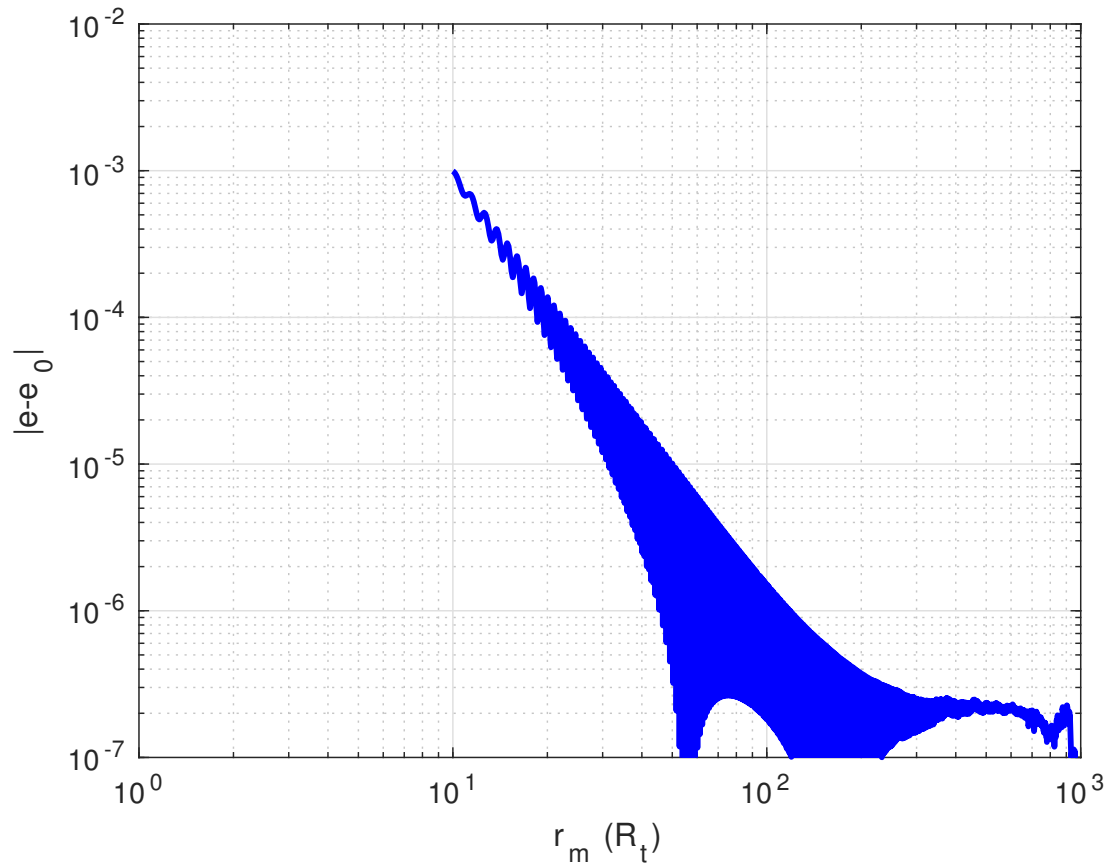


Figure 2.9: The change in binary eccentricity as it approaches the black hole using a full three body integration on a highly elliptical outer orbit with $R_p = R_t$, $R_a = 1000R_t$, $e = 0$, $\theta = 0.25\pi$, and $\phi = 0.5\pi$

Chapter 3

Numerical Simulations

In this chapter I report my findings based on the simulations described in chapter 2. I consider the results of binary disruption in terms of the probability of binary disruption and the energy of the resulting HVSs. I explore how these factors depend on the penetration depth, orientation, binary phase, and eccentricity. I explore in depth the key factors that lead to disruption in the radial case, linking the region of parameter space for which binaries are disrupted, with the free solutions listed in chapter 2.

3.1 Disruption Probability and Ejection Energy

There are two methods that I can use to determine if a binary has been disrupted by the black hole. Both are based on variables that become constant if the binary is disrupted. As the energy of an individual star oscillates between positive and negative values I can determine if a binary has survived its orbit if its energy changes sign after leaving the black hole's tidal radius. I can also use the eccentricity of the star relative to its partner to determine if the binary has been disrupted. If the binary survives its orbit then the relative eccentricity will become a constant value less than one, while a disrupted value will have eccentricity greater than one. Both of these methods produce the same result when the binary orbit is integrated for a sufficient distance outside the tidal radius.

Both methods have a criterion by which I can immediately deduce the final condition of the binary. With the energy method if the star's energy oscillates after the binary has completed its orbit and has exited out of the black hole's sphere of influence then I know it has not been disrupted. With the eccentricity method, if the eccentricity rises above one then I know that the binary has been disrupted. In both these situations I can record the binary's conditions, immediately stop the run and move on to the next set of conditions. If the binary is not integrated up to a large enough time there is a risk of incorrectly classifying certain binaries, as the energy method can miss surviving binaries with orbital periods longer than the integration time, while the eccentric method can miss disrupted binaries that do not separate fully until later on.

Once the binary has passed the periastron it still interacts with the black hole and its partner for a distance before escaping the black hole's sphere of influence, and therefore can have its energy and eccentricity continue to change for a short duration into positive time before breaking up. I therefore do not evaluate the disruption criteria until after the binary is well outside the tidal radius. For my simulations I wait until $t = -t_0/5$, where t_0 is the time when $r_m = 10R_t$ (this being the point I begin my simulations). At this time the binary is outside of twice the tidal radius and I can be confident that the binary is no longer strongly affected by the black hole.

If I do not observe energy oscillations or eccentricity greater than unity I continue the run up until $-10t_0$ to ensure that I am able to detect binaries with very extreme conditions, whose orbits have become wider as a result of their orbit around the black hole, or whose motion relative to each other is almost parabolic. I plot the disruption rate obtained using both methods as a function of θ for radial orbits in Fig. 3.1. When integrated up to $-10t_0$ both methods are comparable with a difference of less than 1%. As neither method presents a significant advantage, for my results I report disruption statistics using the oscillation of energy method.

The probability of a binary's disruption is a complex combination of multiple variables but I shall attempt to describe the way each of the factors interacts to better understand the conditions for disruption.

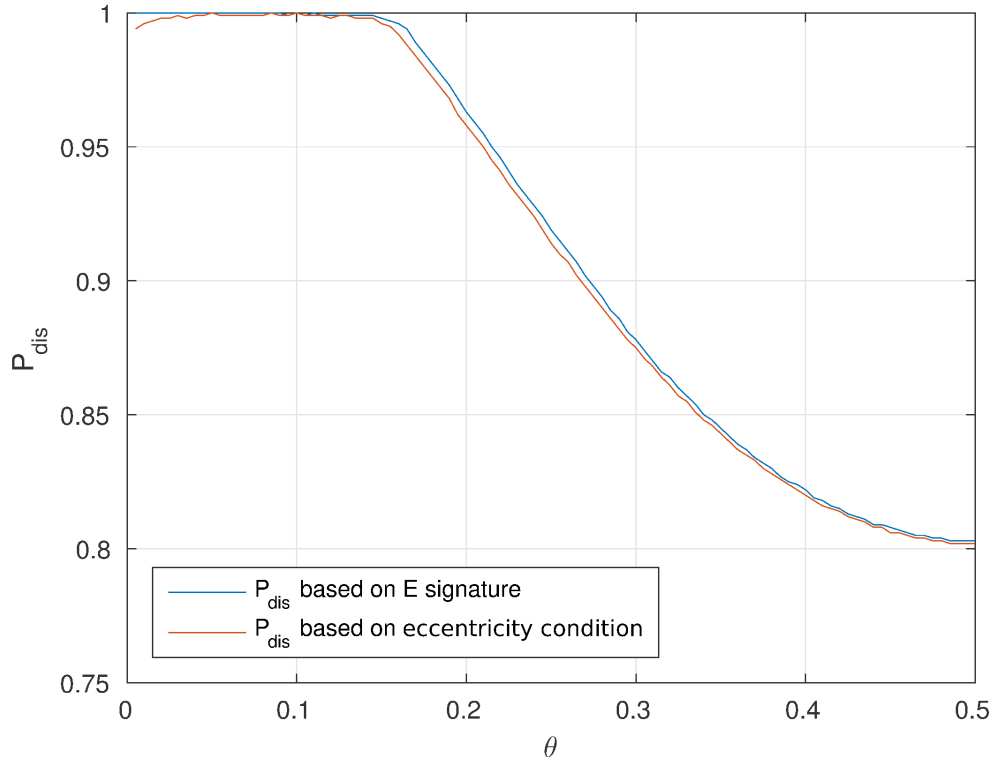


Figure 3.1: Probability of disruption as a function of the inclination angle θ in the radial approximation, with disruption probability measured using the energy oscillation method (blue) and eccentricity method (red).

3.1.1 Disruption Probability and energy with Penetration Depth

Fig. 3.2 indicates the probability of binary disruption at the BH encounter as a function of D averaged over phase and orientation. The largest D for which there is disruption is $D = 2.1$ for the coplanar prograde orbits, and for all sampled orbits. This indicates that coplanar prograde orbits have the highest disruption chance for the shallow encounters. It would be reasonable to expect that as the penetration depth decreases the disruption probability would increase until all binaries become disrupted as the magnitude of the tidal acceleration increases, however that is not what is found. Instead the disruption probability plateaus at $\sim 88\%$, meaning about 12% of binaries survive the BH encounter even for very deep penetrators with $D \ll 1$ and into the radial case (Fig. 3.2).

When the pericentre distance to the MBH becomes comparable to the tidal disruption

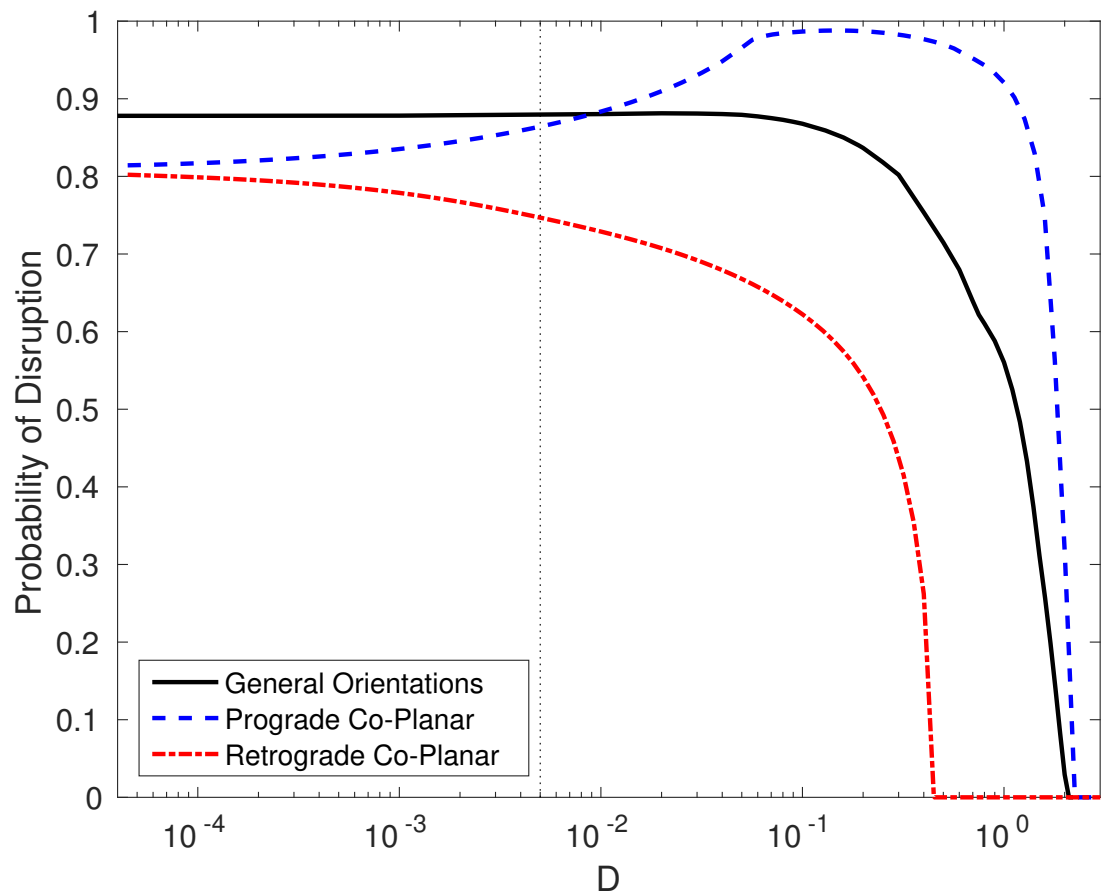


Figure 3.2: Probability of disruption as a function of the penetration factor D . Disruption probability is averaged over all: binary orientations (black solid), coplanar prograde orbits (blue dashed), and coplanar retrograde orbits (red dot-dashed). The vertical dotted line marks the penetration limit for binaries of solar-type stars with $a = 1\text{AU}$ where the individual stars undergo tidal disruption.

radius of the binary members (i.e. individual stars) there is a risk that individual stars might be disrupted by the black hole, destroying them. If the binary members are solar-type stars with radii R_{\odot} and the initial separation of the binary is $a = 1\text{AU}$, the stars themselves are disrupted for $D \lesssim R_{\odot}/a \sim 5 \times 10^{-3}$ (the vertical dotted line in Fig. 3.2). To achieve a smaller D , the initial separation a must be wider, or the binary members should be compact objects such as stellar mass BHs, neutron stars and white dwarfs. For the purposes of this work I treat all stars as point particles and do not consider the potential for the disruption of an individual star. At this point the disruption probability averaged over all orientations has become constant but comparing prograde and retrograde binaries it is clear that they do not converge to the radial solution until much deeper penetrations.

In shallow penetrations the disruption probability can be approximated as a linear relationship as stated in Bromley et al. (2006) where they stated a disruption probability relation of $P_d \approx 1 - D/2.2$ (red line in Fig. 3.3) but my examination of deep penetrations instead finds that a more accurate description of the disruption probability is as a 5th order polynomial function (blue line in Fig. 3.3):

$$P_{dis}(D) = A_0 + A_1D + A_2D^2 + A_3D^3 + A_4D^4 + A_5D^5, \quad (3.1)$$

with coefficients: $A_0 = 0.8830$, $A_1 = -0.0809$, $A_2 = -1.0541$, $A_3 = 1.5377$, $A_4 = -0.9249$ and $A_5 = 0.1881$, for $D < 2.1$. The fractional error $\Delta P_{dis}/P_{dis}$ is less than 1% for $D \lesssim 1$. As the disruption probability approaches zero around $D \sim 2$, the fractional error becomes larger, but it is still about 5% at $D = 1.8$ and about 20% at $D = 2$. This disruption rate of 88% at $D \ll 1$ is higher than that for coplanar binaries. Both coplanar prograde (the blue dot-dashed line) and retrograde (the red dot-dashed line) cases saturate at a level of $\sim 80\%$ (Sari et al., 2010).

The top panel of Fig. 3.4 shows the ejection energy averaged over the binary phase and orientation as a function of D . I also plot in the bottom panel the characteristic maximum ejection energy E_{max} as a function of D . The maximum energy is defined as a largest energy reached by a statistically relevant portion of the sample. This is

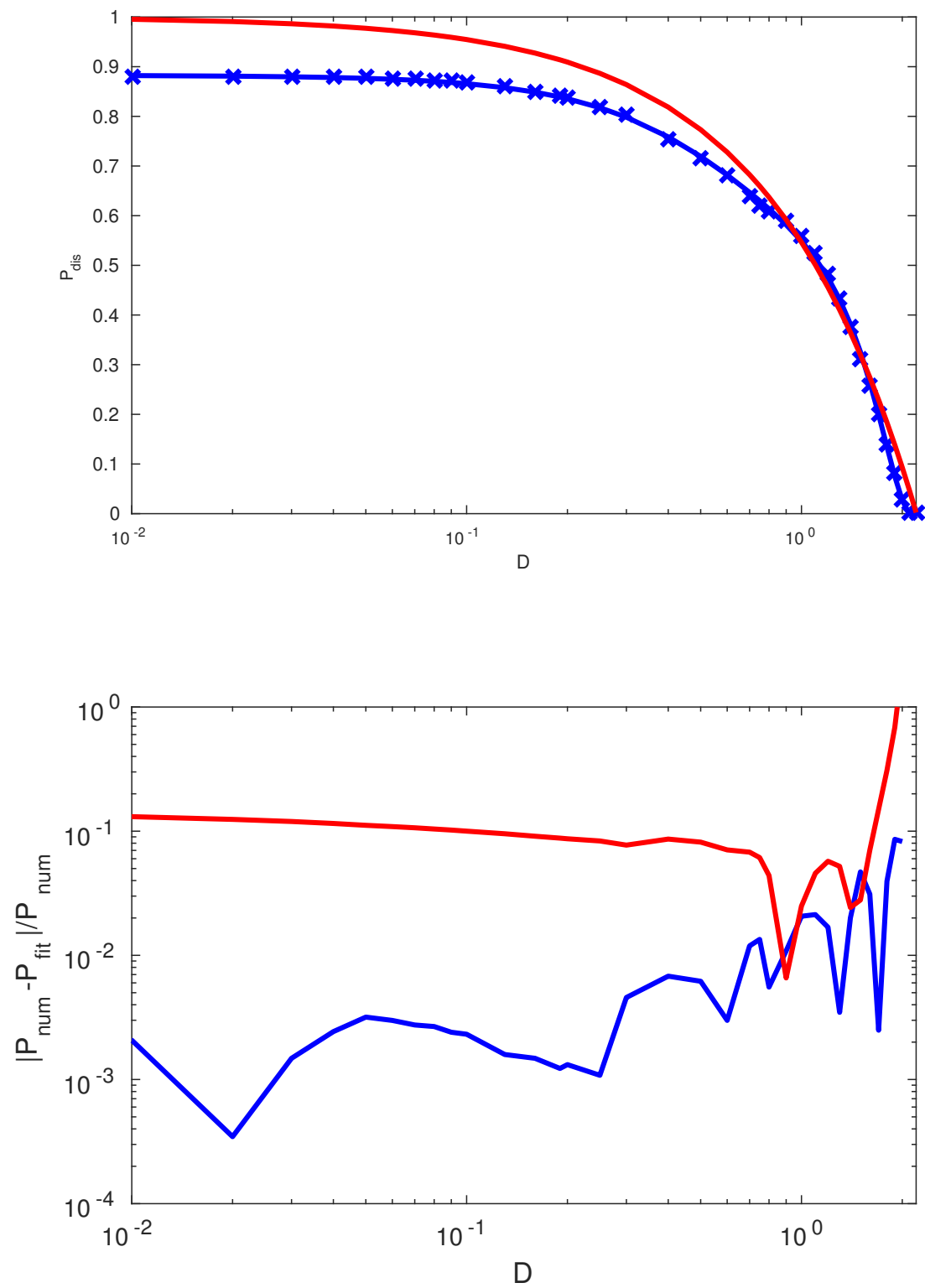


Figure 3.3: Probability of disruption as a function of the penetration factor D averaged over all orientations (blue crosses) with the 5th order polynomial fit eqn. 3.1 (blue line) and the linear fit (red line).

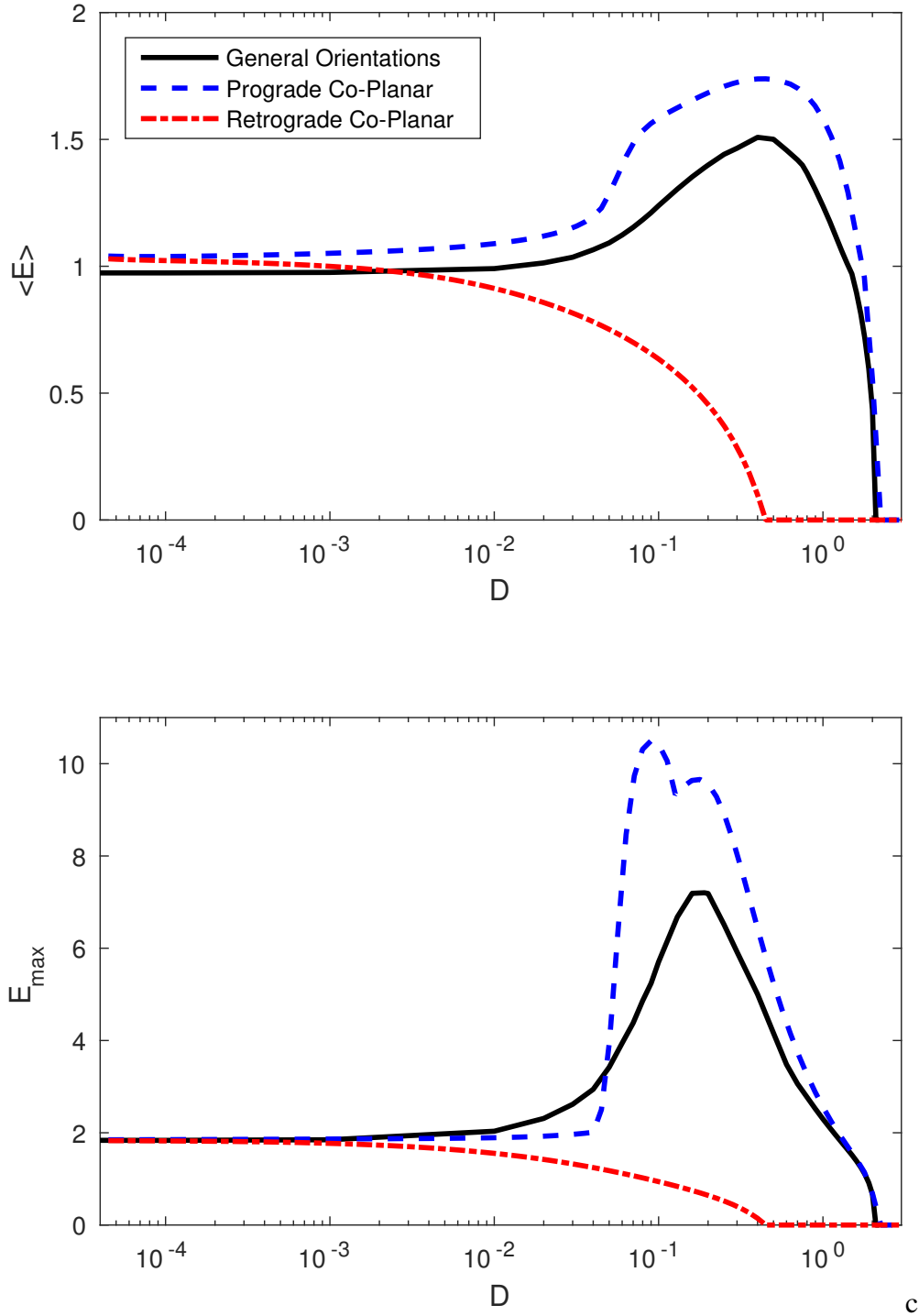


Figure 3.4: Top panel: Ejection energy averaged over binary phase and orientation as a function of D . Bottom panel: Characteristic maximum ejection energy as a function of D . For a given D , the top 1% have ejection energy higher than the characteristic maximum energy E_{\max} . Results for general binary orientations are given by the black solid line, coplanar prograde orbits are given by the blue dashed line, and coplanar retrograde orbits are given by the red dot-dashed line. The average and characteristic maximum energies are in units of $(Gm_1m_2/a)(M/m)^{1/3}$, and they are evaluated for the absolute value of the energy $|E|$.

done by taking the largest absolute value of E after cutting off the top 1% of energies. This threshold value is rather insensitive to the grid resolution, compared to the actual maximum value which is as high as ~ 27 for a coplanar prograde orbit with $D \sim 0.1$ due to how the ejection energy is distributed around the mean. In both plots, a peak is present (the black solid lines), and the peak values are lower than for the prograde orbits (the blue dot-dashed lines). There are two peaks in the E_{max} distribution for the prograde orbits with one peak falling in line with the peak for general orientations and the second at a deeper penetration. The second peak in the prograde orbits is around $D = 10^{-1}$; at this depth there is a knee in the mean energy of the prograde orbits but the mean energy is not sufficient to explain such a large maximum energy. There is another explanation for this peak however that can be found by looking at the disruption probability in terms of binary phase at this depth. At $D = 10^{-1}$ the disruption probability of prograde orbits is $\sim 99\%$, which leaves a very narrow range of binary phase angles over which binaries can survive, and around this range the ejection energy is maximized (Fig. 3.5). The energy change as a function of binary phase will be described in greater detail in section 3.1.3.

The average energy for the ejection energy is approximated by a polynomial,

$$\langle E \rangle = A_0 + A_1 D + A_2 D^2 + A_3 D^3 + A_4 D^4 + A_5 D^5, \quad (3.2)$$

with coefficients: $A_0 = 0.9582$, $A_1 = 3.3268$, $A_2 = -6.6801$, $A_3 = 5.2785$, $A_4 = -1.8731$, $A_5 = 0.2260$, where this energy is in units of $(Gm_1m_2/a)(M/m)^{1/3}$. The fractional error is less than 1% for $D \lesssim 1$, and it is about 3% at $D = 1.8$ and about 10% at $D = 2$. By equalizing this energy in the physical units with the kinetic energy $m_1 v_1^2/2$ (or $m_2 v_2^2/2$), I can estimate the ejection velocity of the primary (or secondary) star at a distant place from the BH. The Galactic potential should be taken into account separately to estimate the velocity in the halo (e.g. Rossi et al., 2014, 2017).

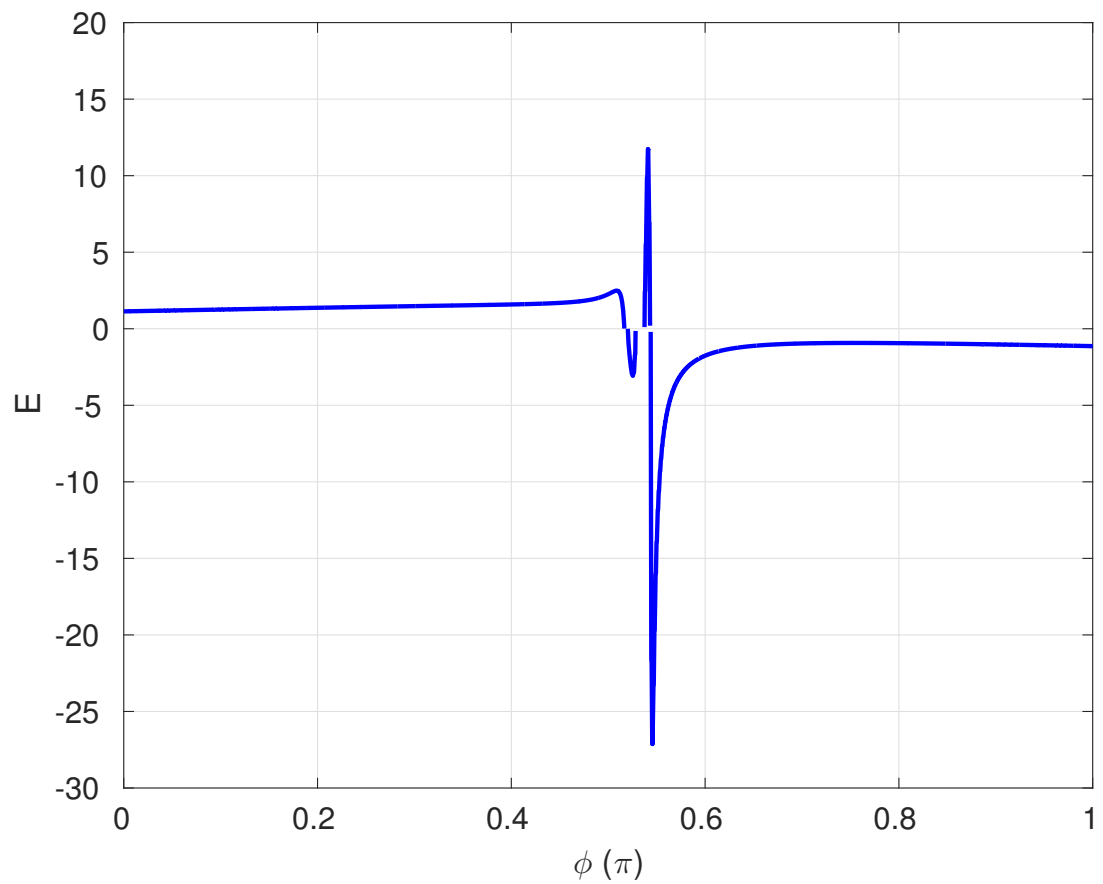


Figure 3.5: The final energy of the primary star post disruption by a massive black hole starting from co-planar prograde orbits with penetration depth of $D = 10^{-1}$ with energy in units of $Gm_1m_2/a(M/m)^{1/3}$

3.1.2 Disruption Probability and Energy with Orientation

So far I have spoken of disruption in terms of the average for all inclinations or for coplanar prograde or retrograde, however I have found an interesting variation in disruption rate with orientation. It is clear from the prograde and retrograde co-planar results that, at least in shallow orbits, disruption is favoured in prograde orbits as opposed to retrograde orbits. Given that the disruption rate averaged over orientation lies in between these two it would seem that the disruption rate would fall off with inclination from the co-planar; this is true for shallow penetrations but the dependency on orientation changes dramatically in deeper penetrations.

I start by considering disruption rate as a function of the inclination angle θ . As I have discussed in the previous section, since there is correspondence between (θ, φ) and $(\pi - \theta, \pi - \varphi)$, the disruption probability (and the ejection energy averaged over binary phase) should be the same for the two binary orientations: $P_{dis}(\theta, \varphi) = P_{dis}(\pi - \theta, \pi - \varphi)$. By integrating this relation with respect to φ , I obtain the symmetry about $\theta = \pi/2$: $P_{dis}(\theta) = P_{dis}(\pi - \theta)$. The numerical disruption probability is shown in Fig. 3.6 as a function of θ for a fixed D . The symmetry about $\theta = \pi/2$ mentioned in chapter 2 is demonstrated.

For deep penetrators $D \ll 1$, where the trajectory of the binary's centre of mass becomes radial, the binary orientation should be characterized only by the inclination angle θ . Prograde or retrograde has no meaning or influence in this limit, indeed in Fig. 3.2, prograde and retrograde results overlap in this regime. The radial approximation (the blue circles in the upper panel of Fig. 3.6) is in a good agreement with the very deep penetrations ($D = 10^{-5}$, the blue solid line) and the fractional difference in the probability of disruption between the radial and general approximations becomes less than 2% for $D < 10^{-4}$. Almost all binaries will be disrupted when the binary rotation axis is roughly oriented toward the BH or it is in the opposite direction. The surviving probability becomes significant for $0.15\pi \lesssim \theta \lesssim 0.85\pi$; the highest surviving probability (or the lowest disruption probability $\sim 80\%$) is achieved for $\theta = \pi/2$. For larger values of D , the surviving probability increases for values of θ closer to 0

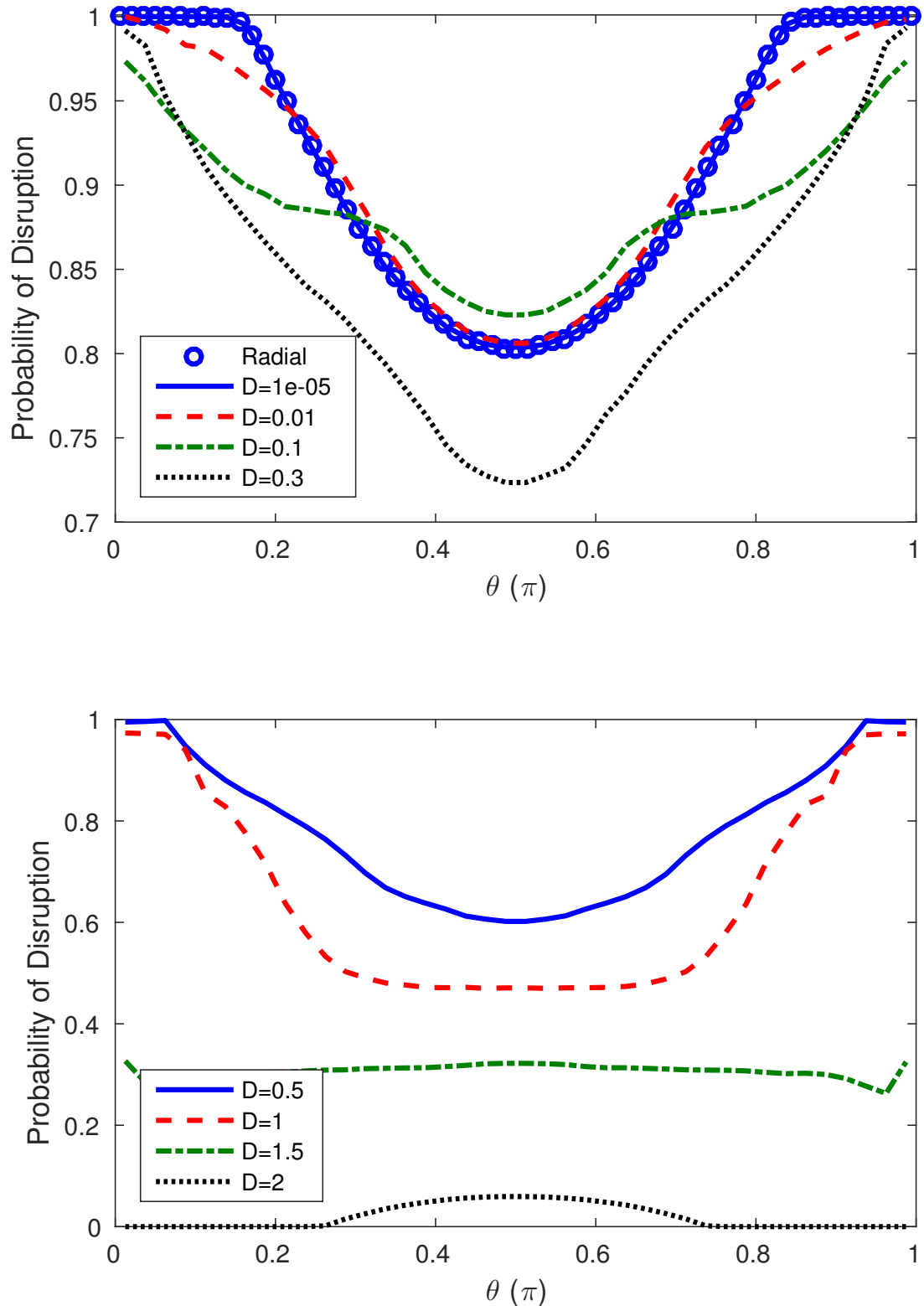


Figure 3.6: Probability of disruption for a given D as a function of the inclination angle θ . Upper panel: deeper penetrators, the radial approximation (blue circles) and the general approximation with $D = 10^{-5}$ (blue solid), 10^{-2} (red dashed), 10^{-1} (green dot-dashed), and 0.3 (black dotted). Bottom panel: shallower penetrators, the general approximation with $D = 0.5$ (blue solid), 1.0 (red dashed), 1.5 (green dot-dashed) and 2.0 (black dotted).

and π .

For very shallow penetrators, the highest disruption probability is achieved around $\theta = \pi/2$, rather than $\theta \sim 0$ or π (see the black dotted line in the bottom panel). This is because the dynamics of the relative orientation of the binary and orbital angular momenta for shallow penetrators leave coplanar prograde orbits relatively vulnerable to disruption.

Fig. 3.7 indicates the ejection energy averaged over binary phase and the azimuth angle for a given D as a function of the inclination angle θ . As already discussed the average energy is symmetric about $\theta = \pi/2$, and the numerical results are therefore plotted only for $0 < \theta < \pi/2$. The radial approximation results (the blue circles) and the general approximation results for $D = 10^{-5}$ (the blue solid line) are almost identical in this figure. However, there is a discrepancy at $\theta = 0$. Due to the nature of the radial approximation, binaries with $\theta = 0$ have zero energy at all times. The general approximation gives non-zero energy and its energy distribution is smooth around $\theta = 0$. For a wide range of D , the average energy slightly increases as the inclination angle θ increases. For the general approximation results, the energy for $\theta = \pi/2$ is higher by a factor of 1.4 – 1.7 than that for $\theta = 0$.

While comparing disruption rates with θ I average over ϕ , meaning that I ignore the difference in disruption rate of prograde and retrograde orbits. I know from the coplanar data sets (blue and red lines in Fig. 3.2) that in shallow penetrations the inclination from prograde is a dominant factor in disruption rate. In Fig. 3.8 I have plotted the probability of disruption as a function of the inclination from prograde coplanar orientation i , averaged over binary phase, for different penetration depths sampled in bins of $\Delta i = 0.05\pi$.

In the deepest penetrations with $D = 10^{-5}$ (the blue line in the top panel of Fig. 3.8), as the orbit approaches the radial approximation the highest disruption rate is found with inclinations of $\pi/2$ with $P_{dis} \sim 90\%$. The disruption rate is symmetrical on either side of this peak, with prograde and retrograde orbits being indistinguishable in radial orbits with $P_{dis} \sim 80\%$. The peak at inclination $\pi/2$ comes from binaries with $\theta \sim 0$

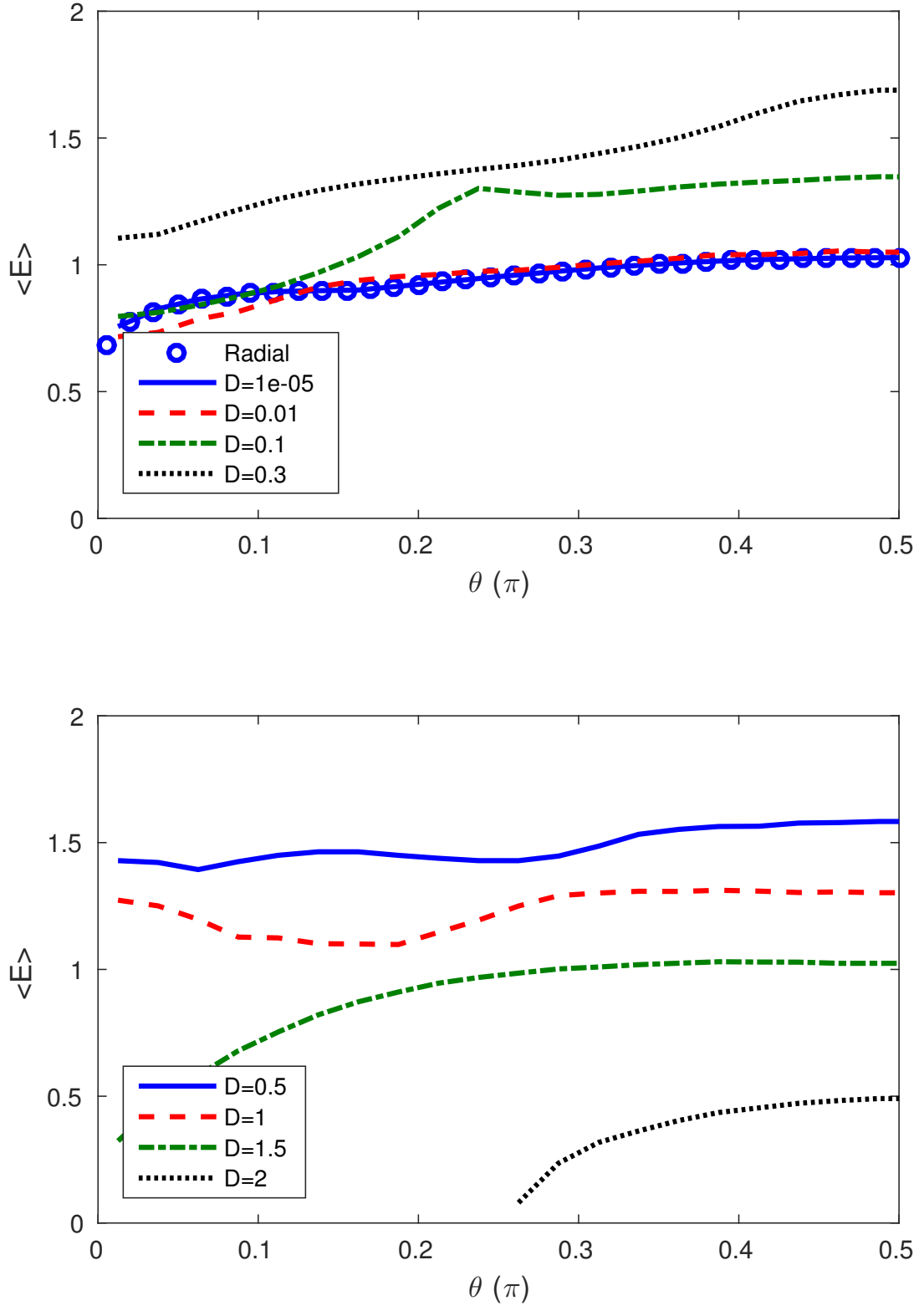


Figure 3.7: Ejection energy averaged over binary phase and azimuth angle for a given D as a function of the inclination angle θ . Upper panel: deeper penetrators, radial solution (blue crosses), $D = 10^{-5}$ (blue solid), 10^{-2} (red dashed), 10^{-1} (green dot-dashed), and 0.3 (black dotted). Bottom panel, shallower penetrators $D = 0.5$ (blue solid), 1.0 (red dashed), 1.5 (green dot-dashed) and 2.0 (black dotted). The average energy is in units of $(Gm_1m_2/a)(M/m)^{1/3}$.

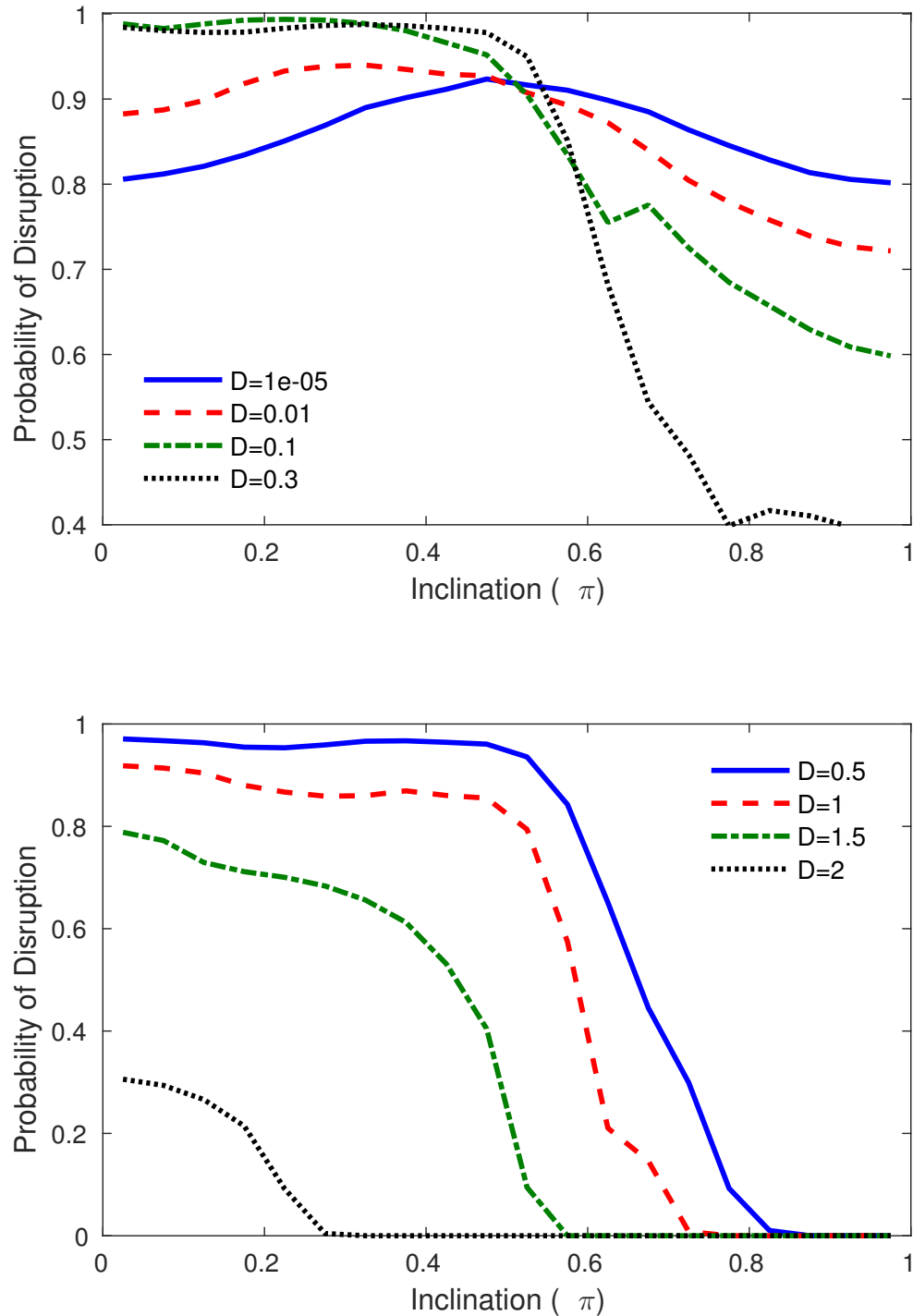


Figure 3.8: Probability of disruption for a given D as a function of the inclination from prograde coplanar orientation. Upper panel: deeper penetrators, $D = 10^{-5}$ (blue solid), 10^{-2} (red dashed), 10^{-1} (green dot-dashed), and 0.3 (black dotted). Bottom panel, shallower penetrators $D = 0.5$ (blue solid), 1.0 (red dashed), 1.5 (green dot-dashed) and 2.0 (black dotted).

or π ; as I have shown in Fig. 3.6 disruption is favoured in that range. As the orbit becomes less radial the prograde-retrograde dependency becomes apparent. For all orbits outside of the radial regime disruption is favoured in inclinations $i < \pi/2$ with the peak disruption rate for $D = 10^{-2}$ found at $i \sim 0.3$ with $P_{dis} \sim 95\%$. From this depth up to $D = 0.5$ the disruption rate is close to 100% for all orientations $i < \pi/2$, while the disruption rate for retrograde orbits rapidly drops with no disrupted binaries found for $i > 0.85\pi$ at $D = 0.5$. After this point the disruption rate drops for all inclinations, after which disruptions are only found in coplanar orientations.

I plot the ejection energy of disrupted binaries as a function of inclination in Fig. 3.9. In non-radial orientations the ejection energy has a similar function to the disruption probability, the energy being higher in ranges with higher disruption rate and lower in ranges of low disruption. This relation can be understood by considering the fact that for a binary to be disrupted the change in energy must be sufficient to overcome the self gravity of the binary and so conditions that produce a high disruption rate would also have a high mean ejection energy.

This relationship is not always true as can be seen in the near radial case of $D = 10^{-5}$ where the inverse is found. I would expect to find the maximum energy at $i = \pi/2$, the same place as the peak disruption is found. What I found however is that the mean ejection energy is lower for this inclination. From Fig. 3.7 I know that in the radial regime the ejection energy drops for orientations $\theta = 0$ and π as in these orientations the relative position of the stars to the black hole results in the individual energies of the stars being close to zero post disruption.

In Fig. 3.10 I have checked the convergence of my numerical results by comparing disruption probability with different sample sizes for specific penetration depth. The probability of disruption shown in Fig. 3.2 (general orientations, the black solid line) is obtained with $N_{ori} = 2000$ binary orientation angles and $N_{\phi} = 200$ binary phase angles. The results are about 87% for $D < 10^{-1}$. The probability is evaluated by changing N_{ori} or N_{ϕ} by a factor of 1/4 – 4. The probability changes less than 0.3% for the lower resolution (a factor of 1/4-1), and less than 0.05% for the higher resolutions (a factor of 1-4).

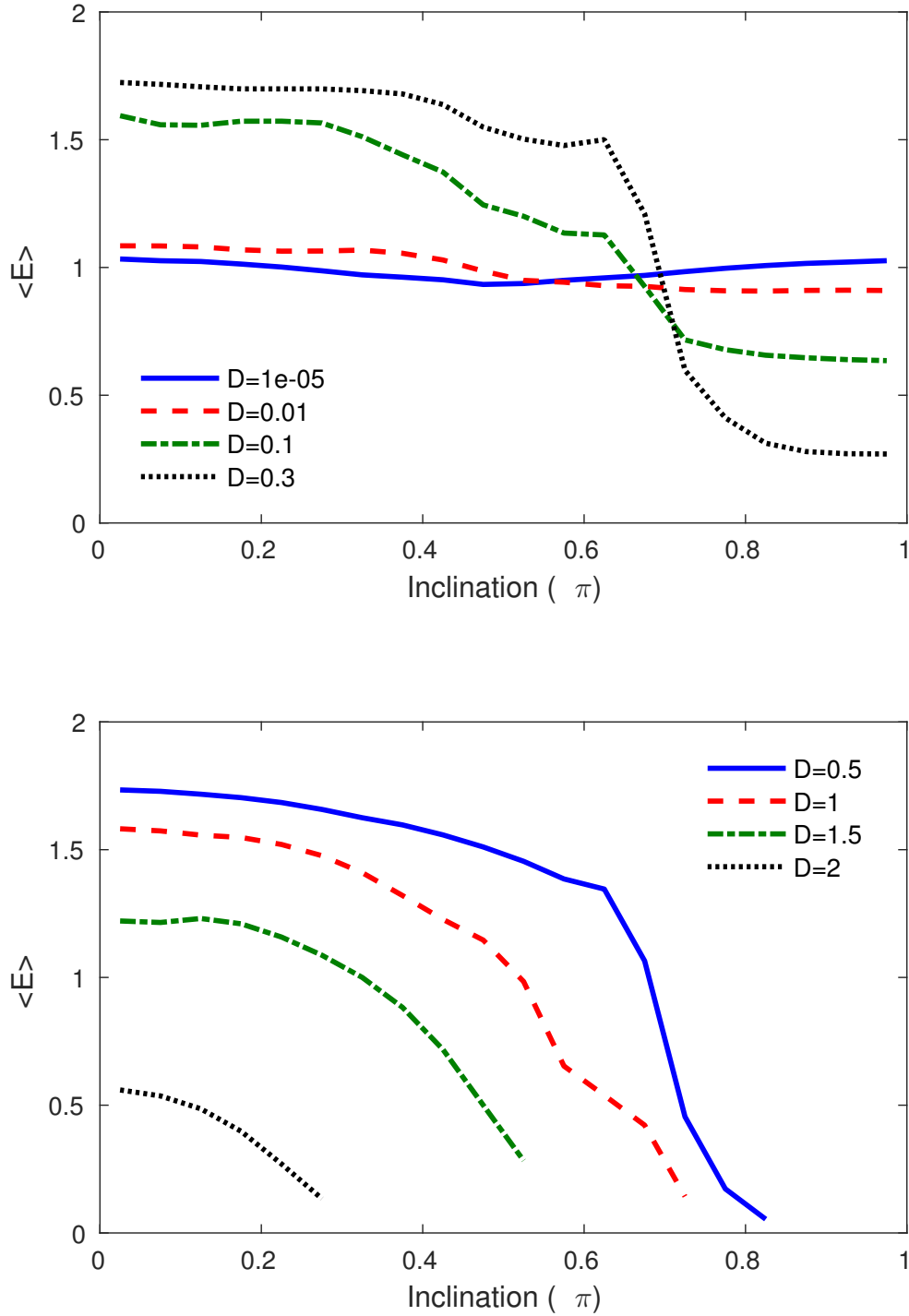


Figure 3.9: Ejection energy averaged over binary phase and inclination angle θ for a given D as a function of the inclination from prograde coplanar orientation. Upper panel: deeper penetrators, radial solution (blue crosses), $D = 10^{-5}$ (blue solid), 10^{-2} (red dashed), 10^{-1} (green dot-dashed), and 0.3 (black dotted). Bottom panel, shallower penetrators $D = 0.5$ (blue solid), 1.0 (red dashed), 1.5 (green dot-dashed) and 2.0 (black dotted). The average energy is in units of $(Gm_1m_2/a)(M/m)^{1/3}$.

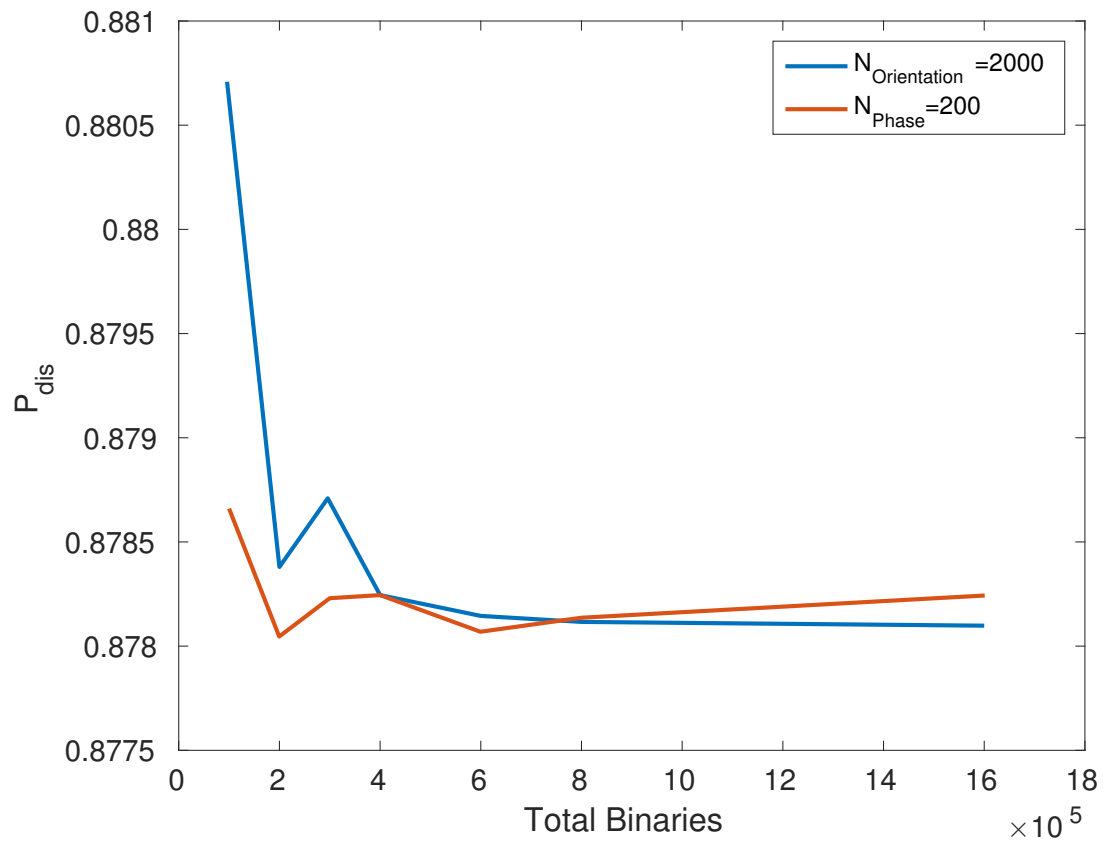


Figure 3.10: The binary disruption probability P_{dis} averaged over all binary phase angles and orientations with penetration depth $D = 10^{-3}$ and different total sample sizes. The points on the blue line are samples with 2000 orientations and 50 – 800 binary phase angles, while the red line points are samples with 200 binary phase angles and 500 – 8000 orientation angles. There is no significant difference in disruption probability when increasing total sample size beyond 4×10^5 .

3.1.3 Disruption Probability and Energy with Binary Phase

For a given penetration depth and orientation it is found that disrupted binaries are grouped within distinct ranges of ϕ . Within each range all binaries are disrupted with the primary always being either ejected or bound to the black hole, that is to say that the signature of the energy does not change within a disruption range. Given the negative energy solution for orbits with a binary phase rotated by π this leads to an equal probability of either star being ejected. Outside these disrupted ranges there is a range where binaries survive their orbits.

When the results are taken in terms of binary phase, disruption probability is no longer relevant as the results of binaries' orbits can not be averaged over orientation. Instead the result is simply a question of if, for a single set of initial conditions, the binary has been disrupted or not and what the energy of the energy change is for that set if it has been disrupted.

I can make three statements regarding the behaviour of binaries as a function of binary phase that are always found to be true.

- Whether a binary has been disrupted or not is not random. For a given orientation and penetration depth there are distinct ranges of binary phase where all binaries are disrupted.
- For a given range of disrupted binaries, the signature of the energy does not change. In other words, for a given disruption range it will always be the primary star that is ejected while the secondary becomes bound to the black hole. This is reversed on rotation of binary phase by π .
- The magnitude of the change in energy of the binary is continuous within a disruption range. Energy as a function of binary phase cannot be expressed exactly as it is dependent on orientation and penetration depth.

The exact number of disruption ranges can change with orientation and penetration depth. By looking at prograde binaries specifically (Fig. 3.11), in very shallow pen-

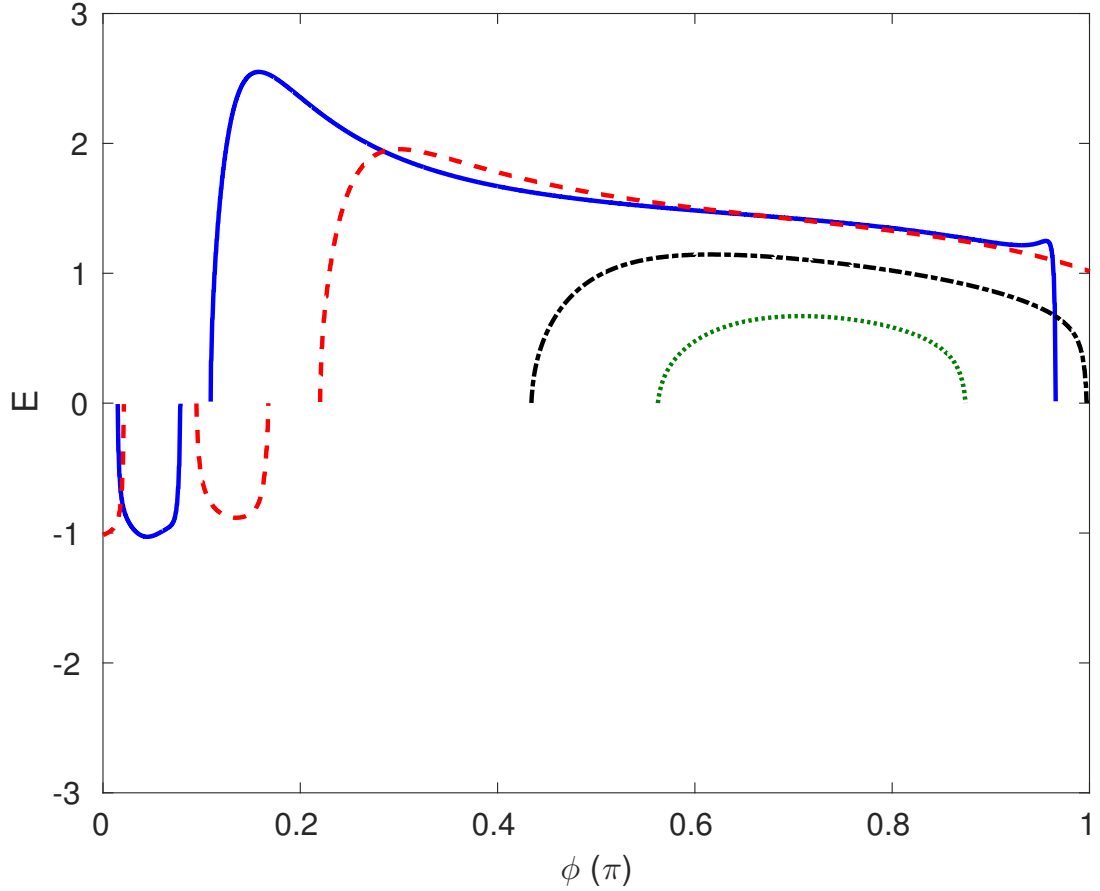


Figure 3.11: The final energy of the primary star post disruption by a massive black hole starting from co-planar prograde orbits with penetration depth of $D = 1$ (solid blue), 1.25 (dashed red), 1.75 (dot-dashed black), and 2 (dotted green) with energy in units of $Gm_1m_2/a(M/m)^{1/3}$.

etrations (black and green lines) there is a single disruption range within our sample range but a second range emerges at $D = 1.5$ (red line). This increases to three ranges at $D = 10^{-1}$ as I have shown previously in Fig. 3.5. This later returns to a single disruption range in deeper penetrations.

While I cannot give an exact relation describing energy in terms of binary phase, there are some general rules that can be used to describe the energy. Firstly I note that there is usually a slight gradient from one side of the disruption range to the other. The signature of this gradient is not consistent as a function of changing initial conditions as can be seen in the penetration depths of $D = 1$ (blue line Fig. 3.11) where the gradient is negative, with the energy decreasing with rotation. However for $D = 10^{-4}$ (the blue line in Fig. 3.12) the gradient is positive, with energy increasing on rotation.

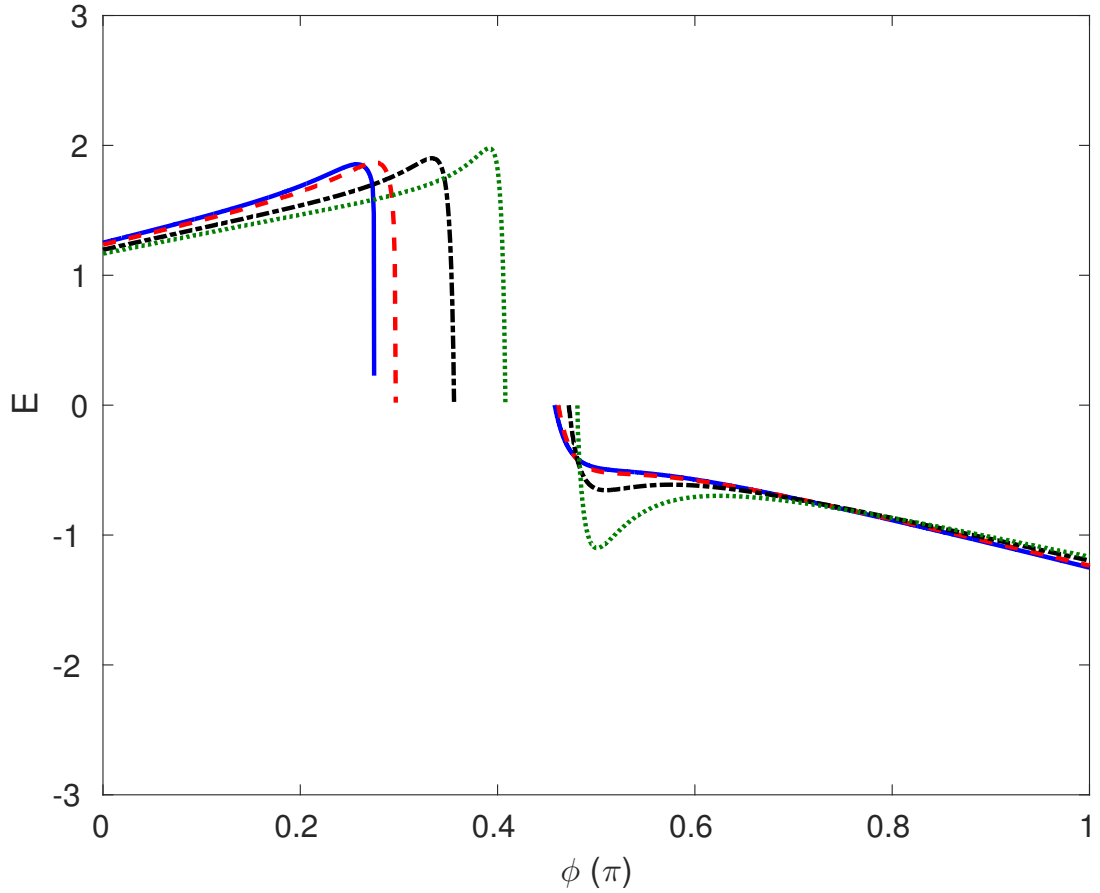


Figure 3.12: The final energy of the primary star post disruption by a massive black hole starting from co-planar prograde orbits with penetration depth of $D = 10^{-4}$ (solid blue), 10^{-3} (dashed red), 10^{-2} (dot-dashed black), and 3×10^{-2} (dotted green) with energy in units of $Gm_1m_2/a(M/m)^{1/3}$.

The second general rule I find is that if the end of one binary range is close to the start of the next range then the energy will peak around that boundary. I show this in Fig. 3.12, where I again plot prograde orbits between $10^{-4} < D < 3 \times 10^{-2}$. Within this range the disruption rate increases as the orbit becomes shallower pushing the edges of the disruption ranges towards each other. As the space between the two edges shrinks the energies of these boundaries grow. This is best shown by the energy of the right hand disruption range for $D = 3 \times 10^{-3}$ (green line of Fig. 3.12, $\phi = 0.5\pi$) where the energy is twice that of $D = 10^{-2}$ (black line) despite both having almost identical energies in the middle of the disruption range $0.2\pi < \phi < 0.7\pi$.

3.1.4 Deep Encounter Survivors

As I have shown, even in the deepest penetration interactions there exists a small fraction of binaries that are not disrupted by the black hole. The existence of surviving binaries for $D \ll 1$ was first discussed by Sari et al. (2010); more recently Addison et al. (2015) also reported a population of such surviving binaries in their large Monte Carlo simulations in which they sample down to $D = 0.35$. Although deep encounter survivors are counter-intuitive, all binaries including these peculiar ones are actually perturbed when deeply penetrating the tidal sphere, and the binary members separate. However, they approach each other after the periapsis passage and a small fraction of them can form binaries again. By observing the disruption distribution in terms of the binary phase the boundaries for disruption can be identified and potential explanations can be made as to the origin of these boundaries. To discuss this behaviour in more detail, I consider the radial restricted three-body approximation. Since the binary orientation is described by a single parameter in this regime, the discussion is simpler. As I have discussed previously, I have analytic solutions for when the binary deeply penetrates the tidal sphere. The A_x solution describes two particles that have the same trajectory, but are slightly separated in time. The B_x solution describes the relative orbits of two particles going on the same radial path, but with slightly different energies. The energy gain or loss at the tidal encounter is proportional to B_x . As the binary approaches the orbital periapsis its position and velocity are dominated by the A_x coefficient. Although the condition which ensures the binary survival after the periapsis passage is not fully understood, I have interesting results which indicate that the A_x and B_x solutions are likely to be related to the process.

Fig. 3.13 shows the range of the initial binary phase ϕ for which binaries survive the deep encounter. This is obtained based on the radial restricted three-body approximation with the binary inclination angle $\theta = 0.3\pi$. The coefficients A_x (the blue dashed line) and B_x (the red solid line) are also shown as functions of ϕ . These coefficients are evaluated at $t = -T_{min} = -10^{-6}$, and they are expected to become constants if the binary is disrupted. As said before B_x is proportional to the energy of an individual member, and the ejection energy of disrupted binaries is plotted having been rescaled

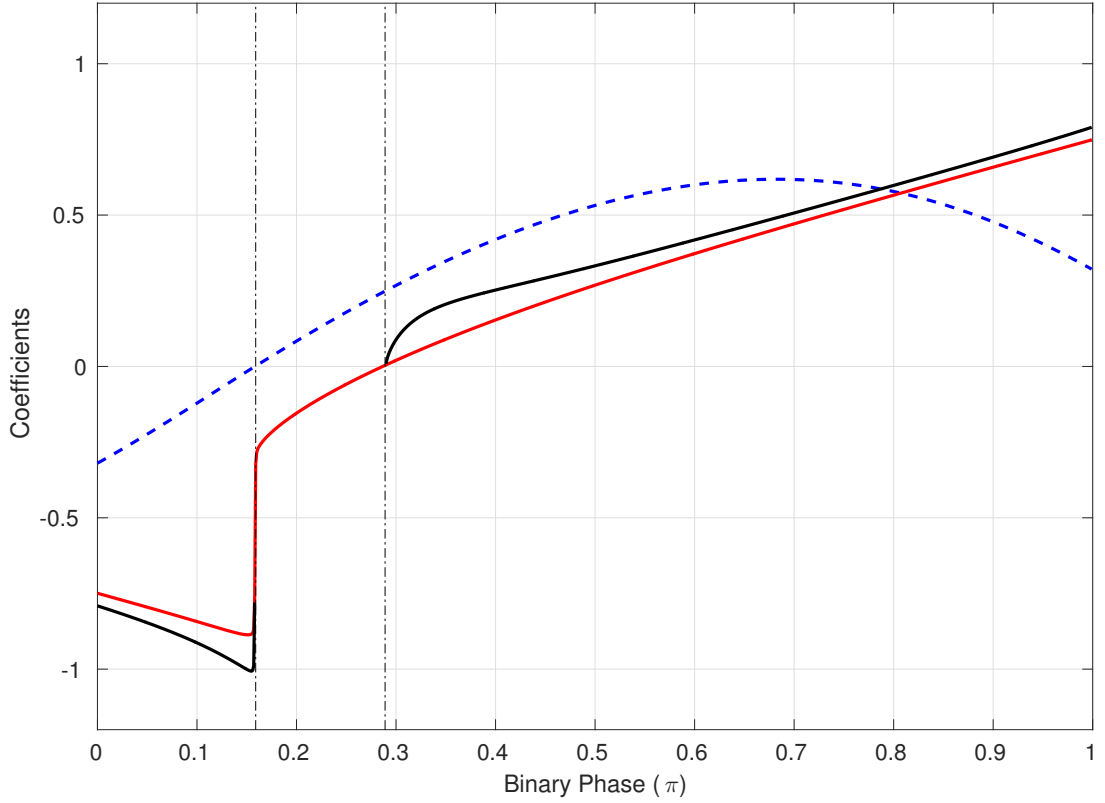


Figure 3.13: The coefficients of the free solutions as functions of the initial binary phase: A_x (blue dashed) and B_x (red solid), along with the ejection energy of disrupted binaries (solid black line) rescaled by $Gm_1m_2/a(M/m)^{1/3}5(2/9)^{2/3}$, thus normalizing it to the same scale as B_x . The binary inclination $\theta = 0.3\pi$ is chosen for this plot as it best demonstrates the link between free solution coefficients and the surviving range. Binaries survive the deep tidal encounter if the initial binary phase is in a narrow range indicated by the vertical black dot-dashed lines.

to the B_x scale (the solid black line). This energy is equivalent to the value of B_x at infinite time.

I overlay the value of the free solution coefficients A_x and B_x over the ejection energy and the disruption boundaries match up quite well with the point where A_x and B_x cross zero (Fig. 3.13). The goodness of this fit is dependent on binary inclination, with the best fit being for $\theta = 0.3\pi$.

Physically the A_x coefficient can be thought of as the speed at which the stars separate as the orbit approaches $t = 0$. For $-1 \ll t \ll 1$ position and velocity can be described by $x \approx A_x \tilde{t}^{-1/3}$ and $\dot{x} \approx -A_x \tilde{t}^{-4/3}/3$. A small value of A_x means that the separation of binary partners at T_{min} is also small, although it does theoretically still become

infinite at $t = 0$ before returning in positive times. A change in signature of A_x means that the direction that the primary star travels at T_{min} also changes signature. At $A_x = 0$ the binary does not separate at all, as all other terms in the free solution tend to zero when $A_x = 0$, and the binary collapses in on itself, with the stars travelling through each other. A change in the direction of binary separation is unmistakably linked to the survival of binaries although it is unclear whether it is directly causal or if both are dependent on a third condition. While both boundaries have an associated drop in ejection energy, as the energy always drops to zero before reaching the surviving range, the $A_x = 0$ boundary has a much sharper drop than the $B_x = 0$ boundary which as I will explain given the energy's dependency on B_x suggests that a sudden change like the direction of separation would be an explanation for the boundary.

The simplest explanation for the $B_x = 0$ boundary is considering it as an analogue for energy. Since a change in signature of energy is analogous to a star becoming bound instead of being ejected and I know that within a disruption range the signature of ejection energy does not change, it logically follows that when the energy changes signature the disruption range ends. This is reflected in the gradual increase in ejection energy from the B_x boundary as opposed to the A_x boundary. Unlike the A_x boundary the B_x boundary is not an exact match to the $B_x = 0$ point for all orientations.

Fig. 3.14 shows how the boundaries of the surviving region (the black dot-dashed lines) and the initial binary phases at which $A_x = 0$ (the blue solid line) or $B_x = 0$ (the red solid line) depend on the binary inclination angle θ . At a large inclination angle (e.g. $\theta = \pi/2$), binaries survive the tidal encounter for a wide range of ϕ . As a smaller inclination angle is assumed, the surviving region becomes narrower, and there are practically no survivors for $\theta < 0.15\pi$ (or $\theta > 0.85\pi$). In the figure, the $A_x = 0$ line is identical to one of the boundaries of the surviving region (the lower branch). Although the $B_x = 0$ (or equivalently $E = 0$) line is similar to the other boundary (the upper branch) of the surviving region, they are slightly different. I notice that the value of B_x evolves slightly even at $t > 0$ around the boundary, because the binary members do not separate quickly in this region and they weakly interact with each other. The real $E = 0$ line is expected to be identical to the upper branch of the boundaries or slightly

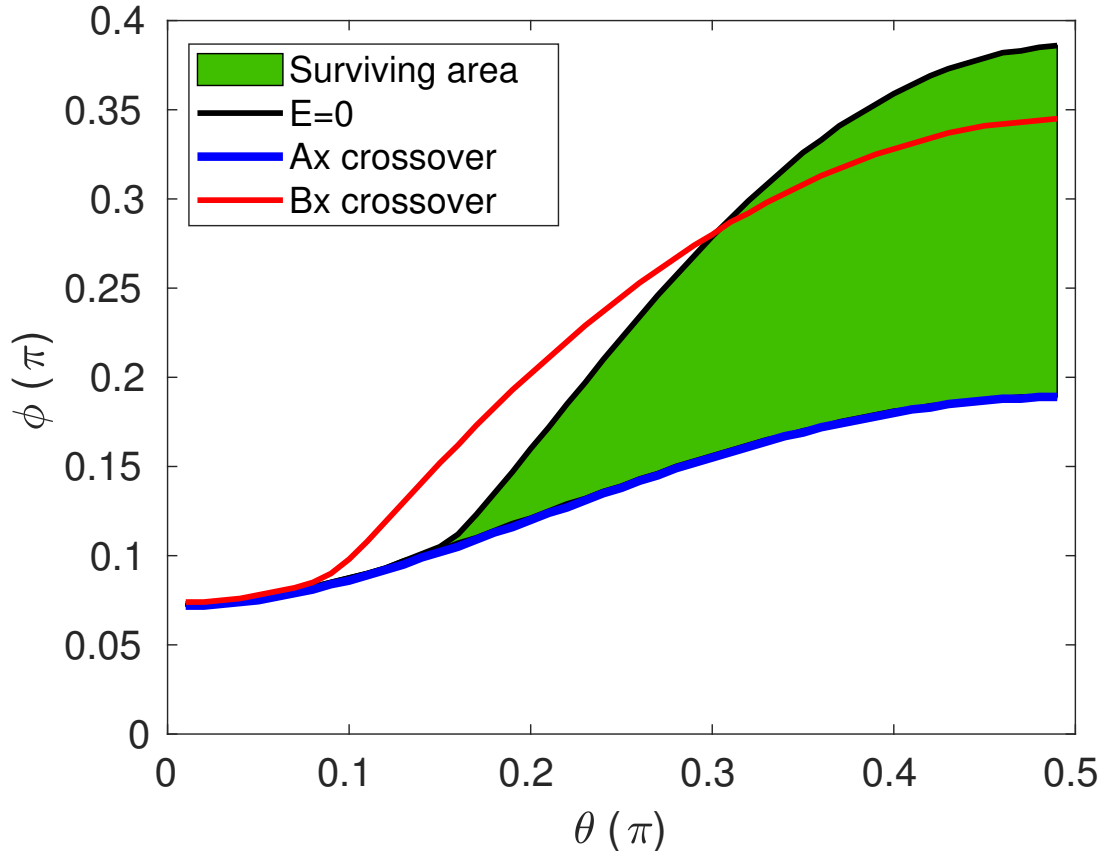


Figure 3.14: The loci of positions in the parameter space for which the coefficients of the free solution A_x (blue solid) and B_x (red solid) are equal to zero, the energy of binary stars ejected from disrupted binaries goes to zero (black solid), and the range of binary phase for which binaries survive the deep tidal encounter (green area). The lower boundary of $E = 0$ and the A_x lines overlap.

inside the surviving region. Otherwise, it means that some binaries are disrupted even if the energy gain or loss at the tidal encounter is zero ($E = 0$). If the binary inclination angle θ is zero or π (i.e. the binary rotation axis is exactly oriented toward the BH or it is in the opposite direction), then from the symmetry of the system, the three-body interaction does not depend on the binary phase ϕ and I obtain $A_x = B_x = 0$ for any ϕ .

I have attempted to link the disruption criteria to the energy and specific angular momentum of the primary star during the periaapsis of their orbit. By observing the evolution of these variables for individual cases with binary phase close to the surviving boundaries I find that there is no significant difference in the behaviour of specific angular momentum at the periaapsis between surviving binaries and disrupted binaries.

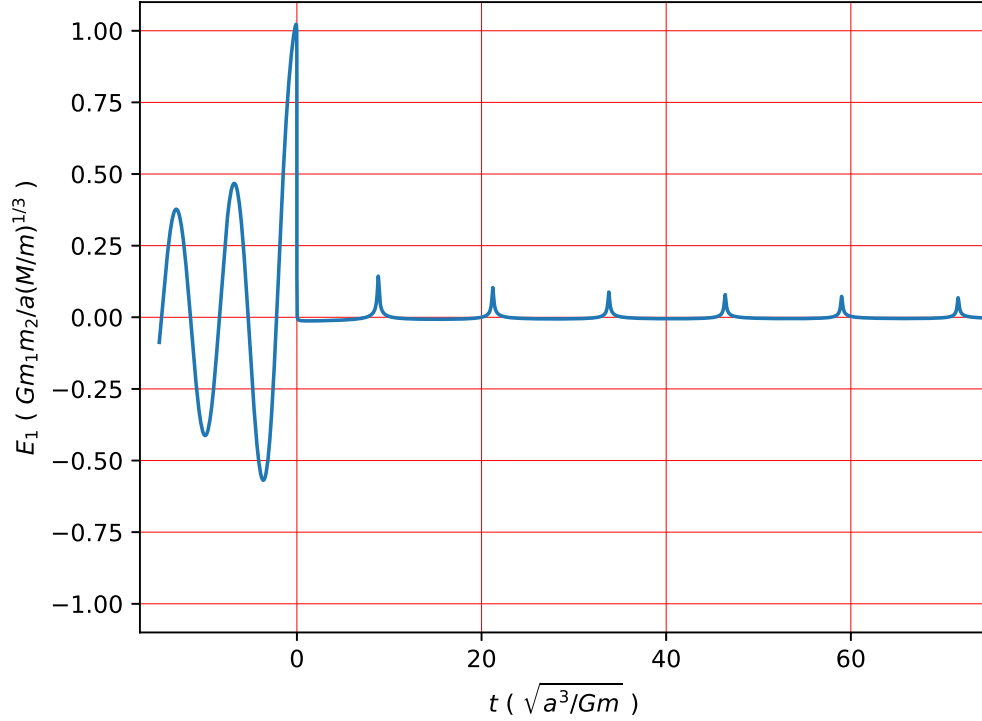


Figure 3.15: The evolution of primary star energy with time for a binary on a radial orbit with $\theta = 0.3\pi$, and binary phase at periapsis of 0.17π . These initial conditions are on the surviving side of the A_x boundary in Fig. 3.14

At the B_x boundary the evolution of energy around the periapsis does not behave any differently with the obvious exception that at $B_x = 0$ the energy at periapsis is also zero; this is expected from what is known about relationship between B_x and energy. I find something significant when considering the evolution of the primary stars' energy around the periapsis at the A_x boundary as shown in Fig. 3.15. In orbits close to the A_x boundary orbital energy sharply drops at the periapsis; this behaviour is present for all inclinations, even ones where disruption does not occur. This behaviour is similar to what is seen in Fig. 3.13 as ejection energy and B_x both drop at the A_x boundary. I still can not make a direct causal link between this drop in energy and the survival of binaries. Despite a thorough exploration of the behavior of binaries in the surviving region and around the boundaries I can not make a solid conclusion as to the cause of the surviving 10% of binaries in the radial case.

As I have just shown, for a given penetration depth and binary orientation, the fate

of binaries (disrupted or not) is determined by the initial binary phase ϕ . If ϕ is in a narrow surviving region, the binary survives the tidal encounter. It means that I can determine the probability of disruption accurately by resolving the narrow region with high resolution grid points. The advantage of my method is that I can analytically handle some of the system parameters (e.g. masses of the binary members, initial binary separation, binary-to-BH mass ratio). The number of essential parameters is smaller than that for the full 3-body calculations. This allows me to set up high resolution grid points in the parameter space, reducing the error on the disruption probability to merely the resolution of my sample.

3.1.5 Disruption probability and energy with binary eccentricity

I now consider the tidal disruption of coplanar, eccentric binaries. As I have discussed in the previous section, I sample ϖ uniformly between 0 and π . Since eccentric binaries spend a larger fraction of their time near the apoapsis, the binary phase $0 < \phi < 2\pi$ is sampled with unequally spaced grids such that the binary rotates from one grid point to the next with a constant time step. The time-averaged binary separation is given by $\bar{a} = a(1 + e^2/2)$ where a is the semi-major axis.

Fig. 3.16 shows the disruption probability of eccentric binaries as a function of D . All cases give $\sim 80\%$ disruption probability for $D \ll 1$. However, for shallow penetrators, the disruption probability strongly depends on the eccentricity and the direction of the binary rotation. For higher eccentricity, binaries are disrupted at a larger value of D , and the peak is shifted to a larger D . In eccentric binaries the time-averaged separation \bar{a} is larger than the semi-major axis of the binary by a factor of $(1 + e^2/2)$, as the penetration depth is defined as $D \propto a^{-1}$ this larger average separation could be considered as an explanation for the shift in peak and maximum penetration depth. Although this qualitatively explains the shifts, even if penetration depth is considered in terms of the time-averaged separation, eccentric binaries are still more vulnerable than circular ones at shallow penetrations. For prograde orbits (the solid lines), as higher eccentricity is used, the peak is shifted at a larger D , and the largest penetration factor

D_{max} for which there is disruption also becomes larger. D_{max} is ~ 2.1 for $e = 0$, ~ 2.8 for $e = 0.3$ and ~ 3.2 for $e = 0.6$ and 0.9 . While the peak disruption probability for $e = 0$ is ~ 1 it is marginally smaller in larger eccentricities. There is little difference between prograde binaries with eccentricity 0.6 and 0.9 . For retrograde orbits (the dashed lines), the eccentricity more significantly affects the probability distribution at shallow encounters. While in the prograde orbits there was little change between larger eccentricities, in the retrograde case it is the low eccentricities between $e = 0$ and 0.3 that are similar. The probability distributions for $e = 0.6$ and 0.9 are similar to the circular binary case for deep penetrations but have a peak structure around $D = 1$, and D_{max} is much larger than the circular case ($D = 0.44$ for $e = 0$), becoming comparable to the values for the corresponding prograde orbits. This suggests that in highly eccentric binaries the significance of the direction of the binary spin on disruption rate for coplanar binaries is less significant.

I plot the ejection energy averaged over the binary phase ϕ and orientation ϖ in the top panel of Fig. 3.17. The energy has been rescaled by $(Gm_1m_2/a)(M/m)^{1/3}$. For prograde orbits (the solid lines), as binary eccentricity increases, the energy function becomes flatter. The peak structure around $D = 0.1 - 1$ which is significant for circular binaries ($e = 0$; the black solid line) disappears and the energy of the prograde orbits is closer to its asymptotic value for shallow orbits. In retrograde orbits, for higher eccentricity, the function extends to larger D because of a larger D_{max} , and the ejection energy becomes similar to that of the prograde binaries in the same way as can be seen in the disruption probability function. In the deep penetration limit $D \ll 1$, the prograde and retrograde orbit cases approach the same ejection energy as expected. Interestingly, the asymptotic energy is not a monotonic function of the eccentricity; the largest value is given by $e = 0.3$ (the blue lines).

I have plotted the characteristic maximum energy of eccentric binaries in the bottom panel of Fig. 3.17. The maximum energies of prograde orbits have a similar function to the mean energy, with the function becoming flatter for higher eccentricities. However, in retrograde orbits the maximum energy behaves in a very different way. For binaries with $e = 0.6$, not only is there a peak in the maximum energy that is not seen in less

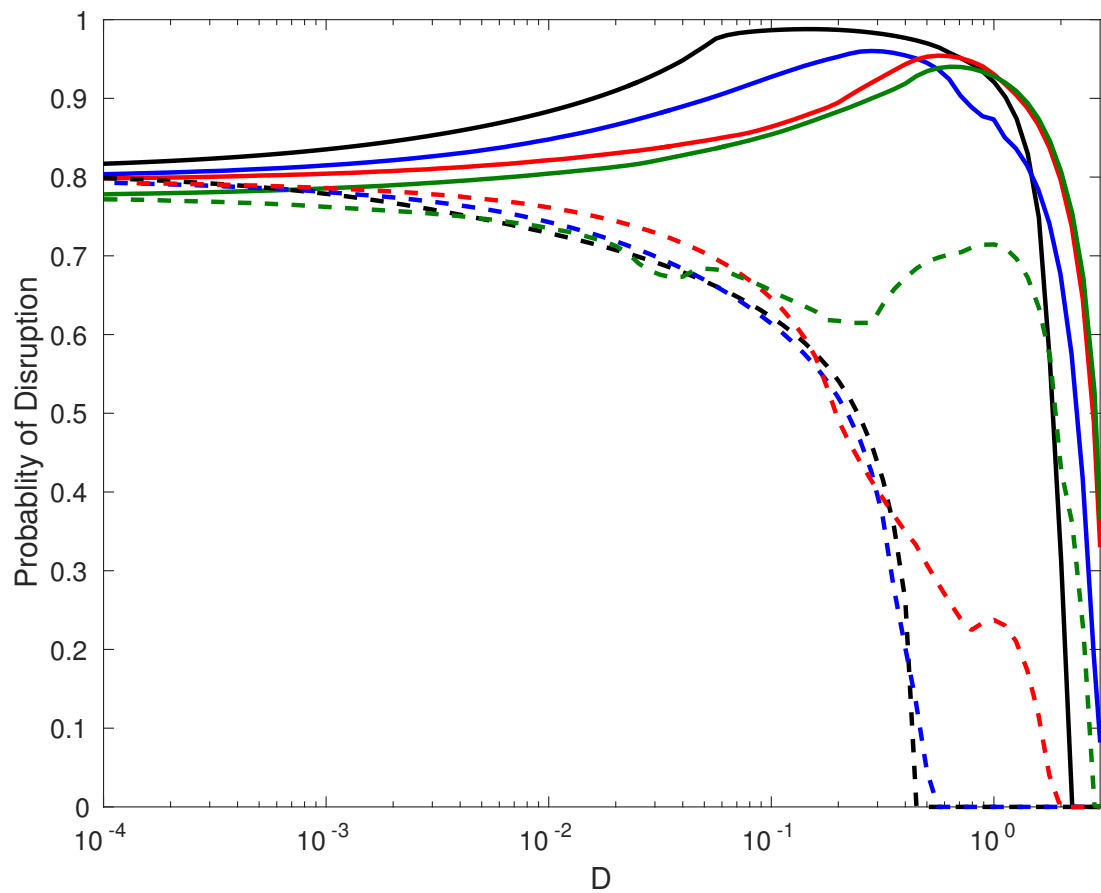


Figure 3.16: Probability of disruption of eccentric binaries with respect to penetration depth for coplanar prograde (solid) and retrograde (dashed) orbits with $e = 0, 0.3, 0.6, \& 0.9$ (black, blue, red, & green, respectively).

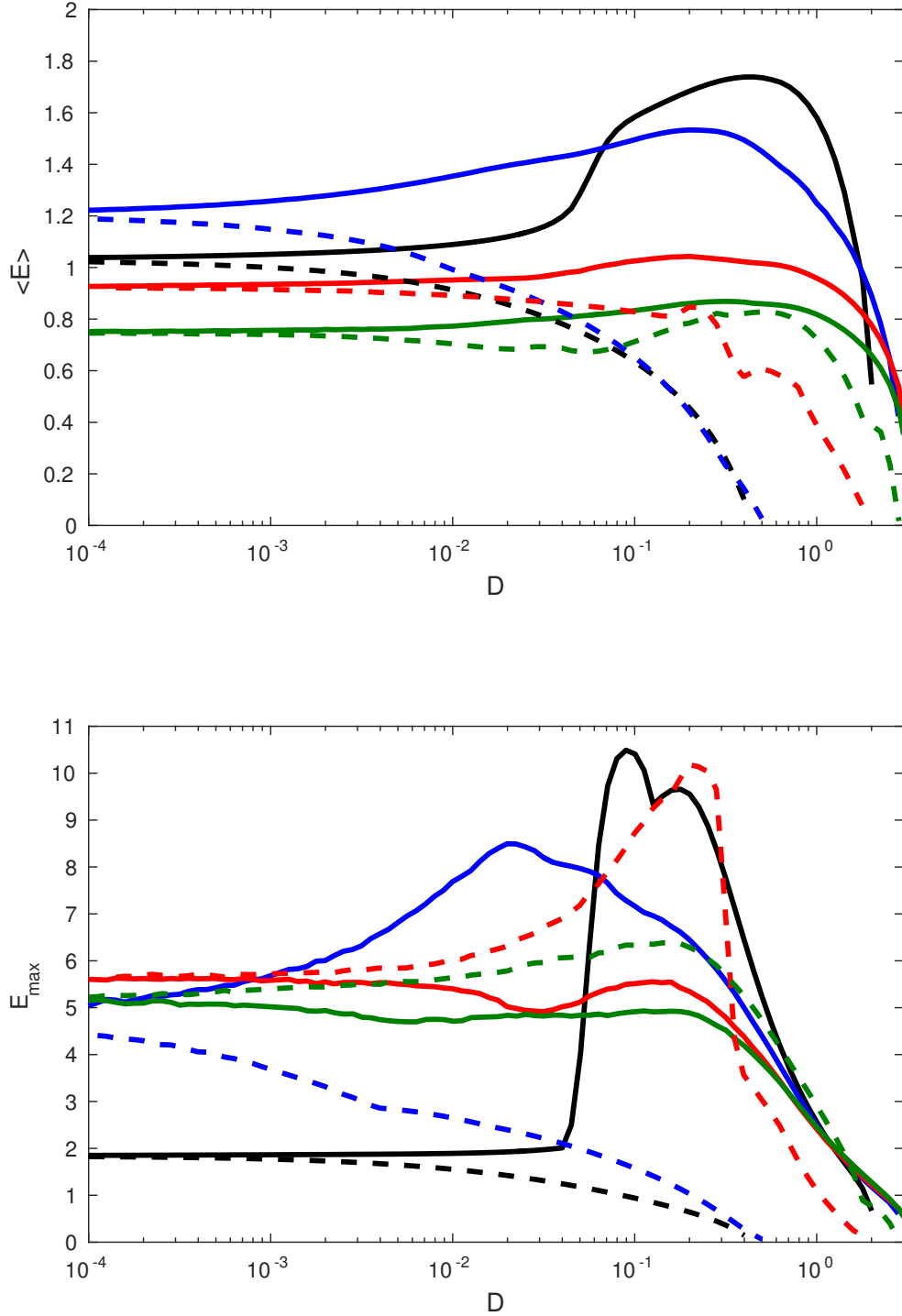


Figure 3.17: Top panel: Ejection energy averaged over binary phase and the orientation of the semi-major axis. Bottom panel: Characteristic maximum ejection energy. These quantities are plotted as a function of the penetration factor D for coplanar prograde (solid) and retrograde (dashed) orbits with $e = 0, 0.3, 0.6$ & 0.9 (black, blue, red & green, respectively). The average and characteristic maximum energies are in units of $(Gm_1m_2/a)(M/m)^{1/3}$, and they are evaluated for the absolute value of the energy $|E|$.

eccentric retrograde orbits, but the maximum energy in the retrograde case actually becomes larger than that for prograde orbits despite the mean energy being lower. The retrograde maximum energy for $e = 0.9$ is also larger than that for the prograde binaries. This reverse continues into the near radial case $D \ll 1$ where the prograde and retrograde orbits approach the asymptote from the opposite directions.

The asymptotic values at $D \ll 1$ are also estimated by using the radial approximation. Although the disruption probability at $D \ll 1$ is less sensitive to the eccentricity (see the top panel of Fig. 3.18), there is a small dip around $e = 0.5$. The average ejection energy has been scaled by $(Gm_1m_2/a)(M/m)^{1/3}$. Since the effective binary separation \bar{a} is larger than the semi-major axis, the disruption of a wider binary should result in an ejection energy smaller by a factor of $(1 + e^2/2)$. The numerical results show a smaller energy for $e = 0.9$, compared to the circular case with $e = 0$ (see the middle panel of Fig. 3.18), and the number is roughly consistent: $1/(1 + e^2/2) \sim 0.7$. However, the numerical energy peaks at around $e = 0.35$. The eccentricity more drastically affects E_{max} (see the bottom panel). The values for $e > 0.4$ are much larger than that for the circular case, and there is a significant peak around $e = 0.35$.

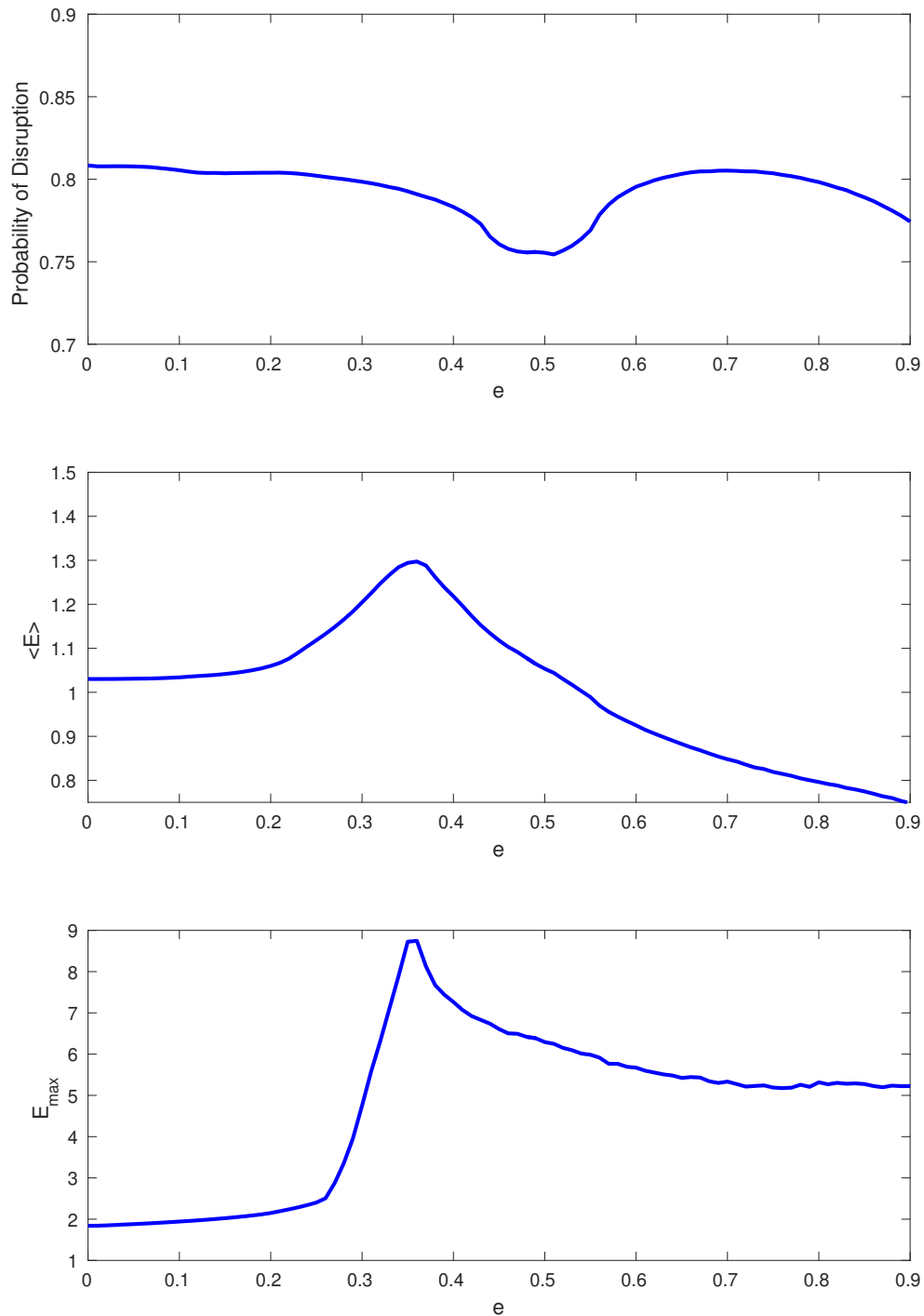


Figure 3.18: Radial approximation results for the inclination angle $\theta = \pi/2$. Top panel: Probability of disruption as a function of eccentricity. Middle panel: Ejection energy averaged over binary phase and the direction of the semi-major axis as a function of eccentricity. Bottom panel: Characteristic maximum ejection energy as a function of eccentricity. The average and characteristic maximum energy are in units of $(Gm_1m_2/a)(M/m)^{1/3}$, and they are evaluated for the absolute value of the energy $|E|$.

3.2 Bound Stars and the conditions of S-Stars

In the previous section I discussed the disruption probability and energy but with a focus on the ejected HVS while ignoring the star that remains bound to the black hole. As I have shown previously the eccentricity of the bound star is given by $1 - e \sim 2(m_2/m)D(m/M)^{1/3}|\bar{E}|$ where in this case m_2 is the mass of the ejected star and \tilde{E} is the energy change rescaled by $(Gm_1m_2/a)(M/m)^{1/3}$; within this section I consider the result only for equal mass binaries. Using the typical mass ratio for binaries in our galaxy $M/m = 10^6$, the mean eccentricity difference $1 - \langle e \rangle$ and the characteristic maximum difference $1 - e_{min}$ are shown as a function of D in Fig. 3.19.

If I consider deep penetrators where $D < (m/M)^{2/3}$ the eccentricity of the bound star can no longer be taken as a linear relation with penetration depth and energy as the angular momentum of the binary centre of mass L_m becomes comparable to the angular momentum change due to the internal angular momentum of the binary ΔL_1 . However since the energy converges with $\langle \tilde{E} \rangle \sim 1$ and $\tilde{E}_{max} \sim 2$ for $D \ll 1$ (see Fig. 3.4), and the angular momentum L_1 becomes constant as ΔL_1 dominates over L_m , the average and characteristic maximum eccentricity becomes constant for deepest penetrations:

$$\langle e \rangle \approx 1 + \left(\frac{m_2}{m}\right)^3 \frac{m}{M} \quad (3.3)$$

$$e_{min} \approx 1 + 2 \left(\frac{m_2}{m}\right)^3 \frac{m}{M}. \quad (3.4)$$

If I compare the eccentricity I would get by evaluating it using the shallow penetration approximation I find that although the shallow penetration approximation produces a value significantly lower than the true value, the eccentricities at these penetrations are so close to unity in both results ($\langle e \rangle - 1 \leq 10^{-6}$) that they can be thought to be parabolic. I can therefore limit my exploration of eccentricity of bound stars to the shallow penetrations which is more relevant to the context of hyper-velocity stars.

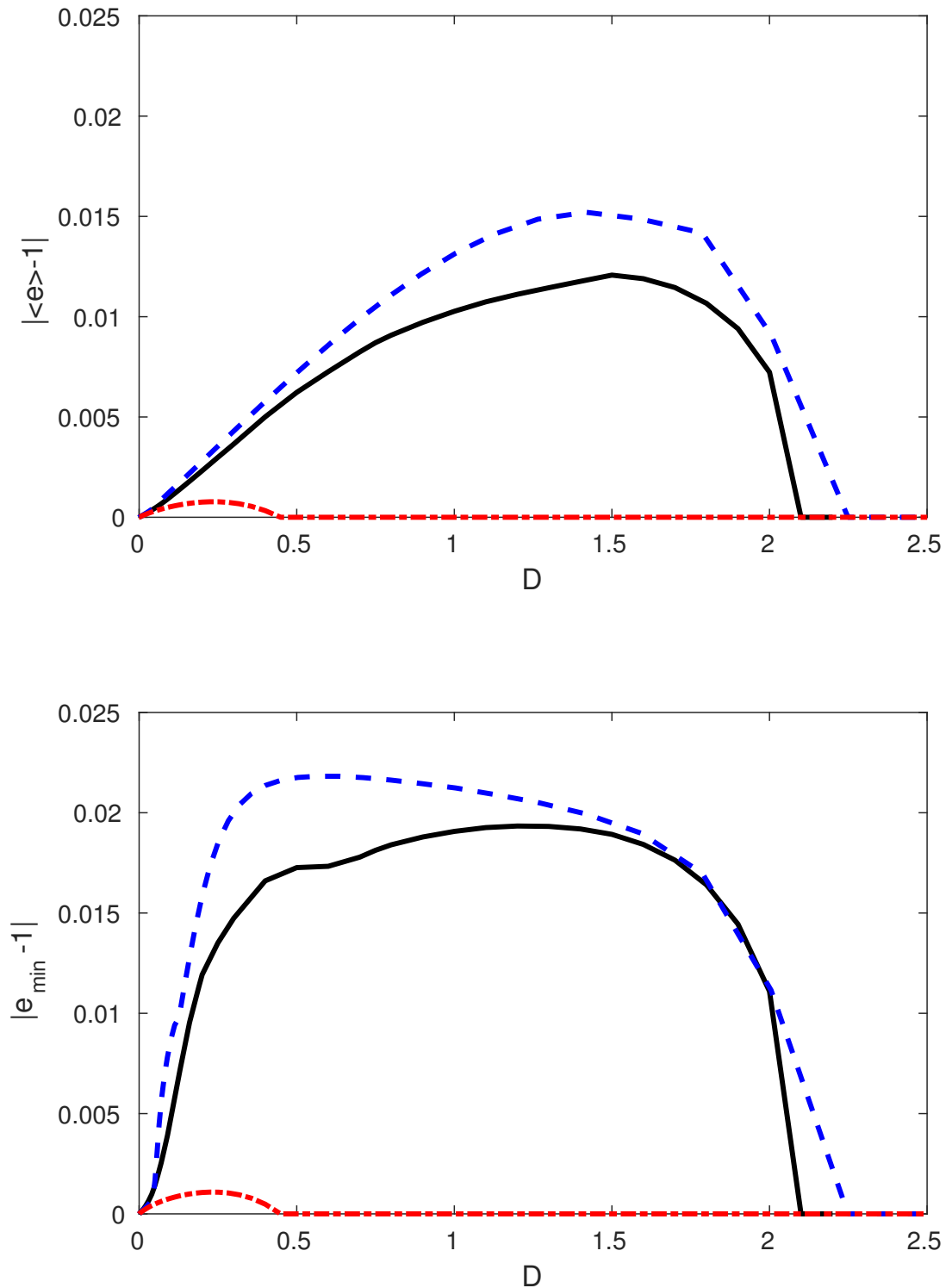


Figure 3.19: Top panel: Mean eccentricity difference from a parabolic orbit in bound stars as a function of D . Bottom panel: Maximum eccentricity difference from a parabolic orbit in bound stars as a function of D , where the bottom 1% have eccentricity lower than the characteristic minimum eccentricity e_{\min} . Lines shown correspond to the general binary orientation (black solid), coplanar prograde orbits (blue dashed), and coplanar retrograde orbits (red dot-dashed). $m_1 = m_2$ and $M/m = 10^6$ are assumed.

The bound eccentricity as a function of penetration depth is plotted in Fig. 3.19. With the dependency of penetration depth on eccentricity, the lowest eccentricities of bound stars come from orbits with shallow penetration depths with a peak at $D = 1.5$ of $e = 0.988$. In orbits shallower than this, the bound eccentricity rises to unity as the mean energy change drops to zero.

Although shallow penetrators $D \sim 1$ give lower eccentricities, they are still very high $e \sim 0.98 - 0.99$, far from the range of eccentricities that have been seen in observations made of S-stars orbiting Sgr A* in the Galactic centre $0.3 \lesssim e \lesssim 0.95$ (Gillessen et al., 2009; Ghez et al., 2008). This suggests that post-capture relaxation is the significant factor in determining S-star eccentricities (Perets et al., 2009; Alexander, 2017).

Since the eccentricity differences $1 - e$ of bound orbits are proportional to their orbital energy, the effect of rotation of binary phase or binary orientation on eccentricity for a given penetration depth is the same as that of energy. However, as I have discussed, the eccentricities of the S-stars are determined by post-capture relaxation processes.

3.3 Surviving binaries

As previously shown, for all penetration depths there is a significant population of binaries that are able to survive their orbit around the massive black hole. As a result of the tidal forces during their orbit these binaries can have radically changed orbital parameters, with high eccentricity and semi-major axis changed significantly from the initial separation.

In Fig. 3.20 I have plotted the distribution of final semi-major axis of the surviving binary, in terms of the initial binary separation, as a function of penetration depth. I focus on the shallow penetration events here as they are more relevant to real astrophysical scenarios. In penetration depths $D > 1.75$ the surviving semi-major axis is not significantly different to the initial separation with a median of $a = 0.975^{+0.025}_{-0.125}a_0$ where 70% of surviving binaries are within the upper and lower boundaries. As binaries penetrate deeper the upper boundary and median of the distribution (red and black lines in Fig. 3.20 respectively) increases while the lower boundary (blue line in Fig. 3.20) remains constant. These trends drop off at certain penetration depths with the distribution range dropping before converging to the radial case with $a = 0.805^{+1.81}_{-0.442}a_0$.

In Fig. 3.21 I have plotted the distribution of the final eccentricities of the surviving binaries, in terms of the initial binary separation, as a function of penetration depth. The distribution of final eccentricities is far wider than that of the semi-major axis, with median value of $0.246^{+0.321}_{-0.203}$ at the shallowest penetration I sample. In these shallow penetration depths the extreme changes in eccentricity occur with very little change in semi-major axis as seen in Fig. 3.20. This leaves the orbital energy unchanged meaning that the eccentricity change comes from changes in angular momentum. This leads to a change in orientation in the same fashion as the Kozai-Lidov mechanism (Naoz, 2016).

The change in orbital parameters extends outside the range of penetration depths where disruption can occur. My data do not extend far beyond this range, limiting my ability to comment on the distribution for $D > 2.2$. However it can be seen that as penetration depth grows and the binary-black hole dynamical time-scale grows relative to the

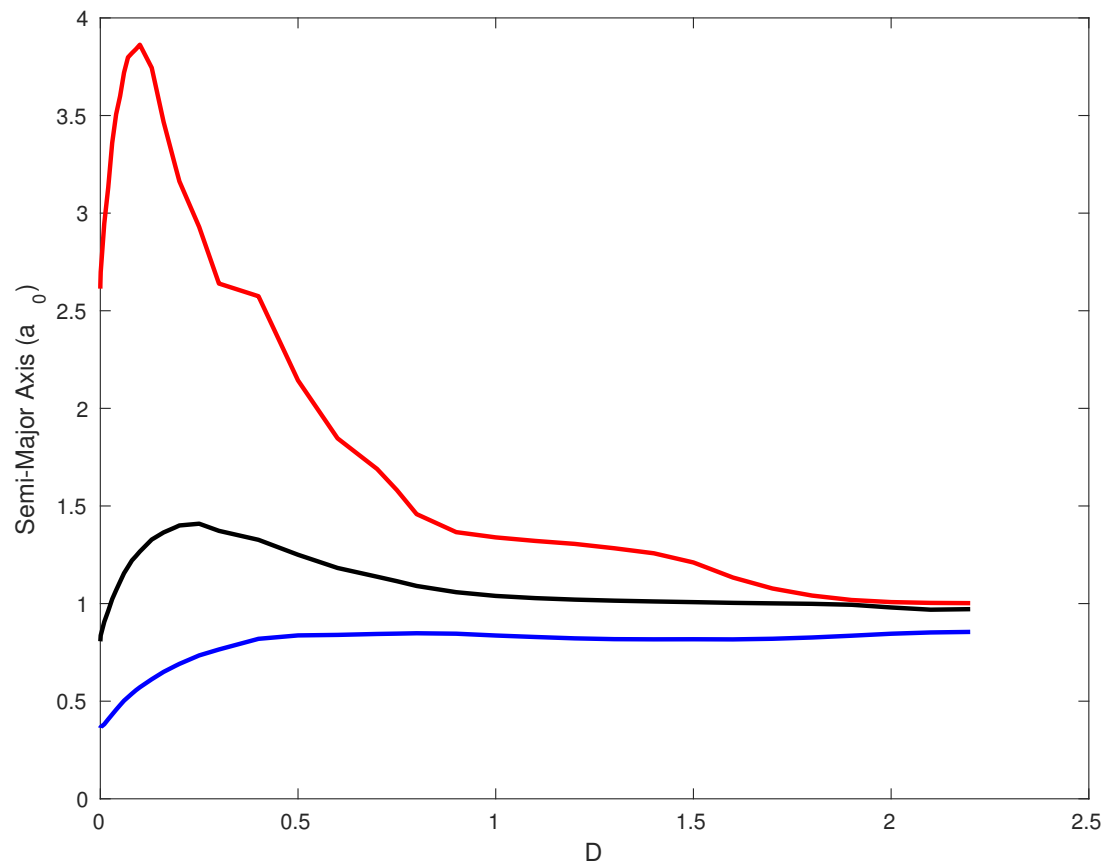


Figure 3.20: Distribution of final semi-major axis of the surviving binary, in terms of the initial binary separation, as a function of penetration depth. The median semi-major axis is shown as the black line. The largest 15% of final semi-major axis values lie above the red line, while the smallest 15% are below the blue line.

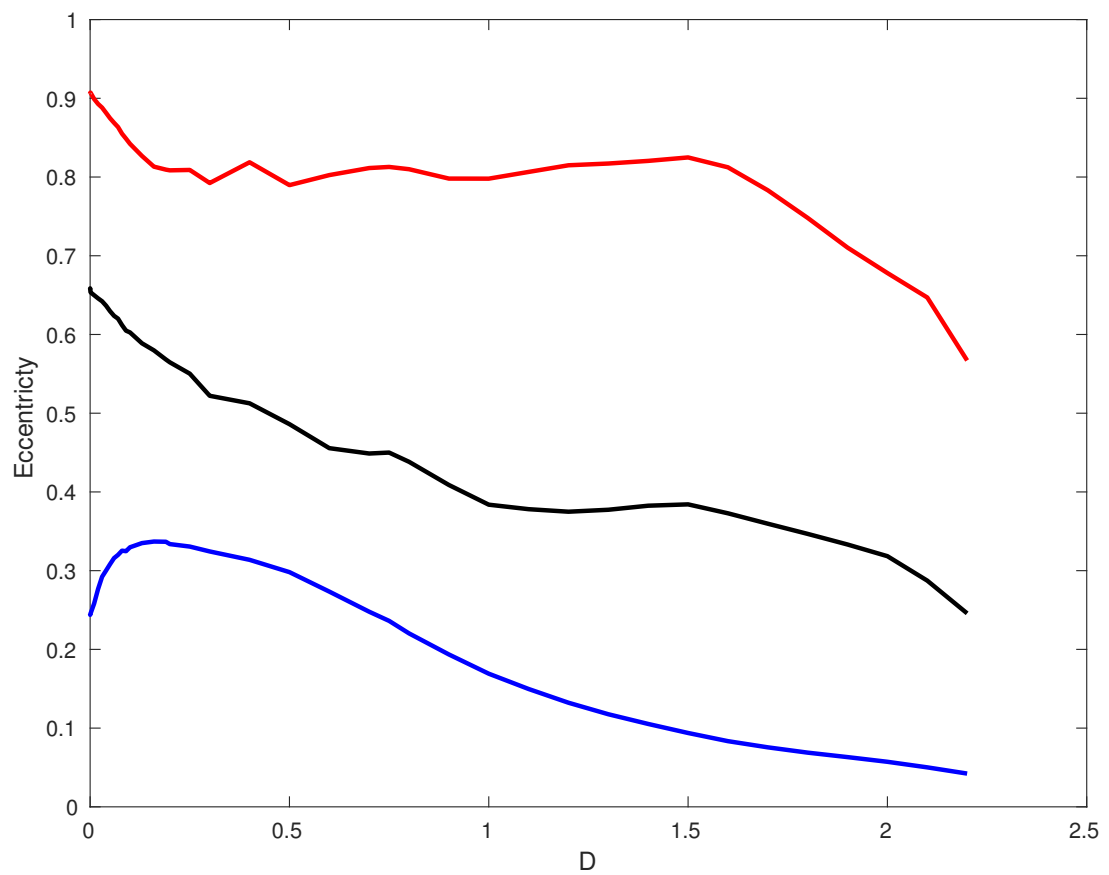


Figure 3.21: Distribution of final eccentricities of the surviving binary as a function of penetration depth. The median eccentricity is shown as the black line, the largest 15% of final eccentricities lie above the red line, while the smallest 15% are below the blue line.

binary orbital period the change in orbital parameters can be ascribed entirely to the Kozai-Lidov mechanism.

These surviving binaries have an interesting significance to the field of gravitational wave astronomy. The gravitational wave detection GW150914 reported by Abbott et al. (2016b) was a merger by two black holes of masses $36_{-4}^{+5}M_{\odot}$ and $29_{-4}^{+4}M_{\odot}$. This detection was followed up by GW151226 (Abbott et al., 2016a), GW170104 (Abbott et al., 2017a), GW170608 (Abbott et al., 2017b), GW170814 (Abbott et al., 2017c), and most recently GW170817 (Abbott et al., 2017d). With the exception of GW170817, the merger of two neutron stars, all confirmed mergers to date have been between binary black hole systems.

The inspiral time of a binary due to gravitational wave emission is given approximately by Peters (1964) as:

$$T_{GW} \approx 150\text{Myr} \left(\frac{m}{M_{\odot}} \right)^{-3} \left(\frac{a}{R_{\odot}} \right)^4 (1 - e)^{\frac{7}{2}}, \quad (3.5)$$

This strong dependence on semi-major axis and eccentricity means that perturbation by a massive black hole could act to accelerate the merger of compact binaries. To this end I have calculated the ratio of merger timescales post-orbit and pre-orbit (Fig. 3.22). As in this case I am only discussing circular binaries with $e = 0$, the inspiral time ratio is given by $T_{post}/T_{pre} = (a/a_0)^4(1 - e)^{7/2}$. The inspiral time of over 10% binaries post orbit have been reduced to less than 1% of their initial inspiral time. In shallow penetrations all binaries have their inspiral time reduced with almost zero binaries having their inspiral time unchanged or made longer than their initial inspiral time. In deeper penetrations the inspiral time is decreased even further, with 10% of $D = 10^{-2}$ binaries having inspiral times less than 0.001% of the original value, however in deeper penetrations there is potential that a surviving binary could have a larger semi-major axis than it started with resulting in a longer inspiral time. These increased inspiral time binaries are in the minority with only 6% of binaries having their inspiral time increased to more than ten times the original value.

The relevance of this method for shortening inspiral times is dependant on the preva-

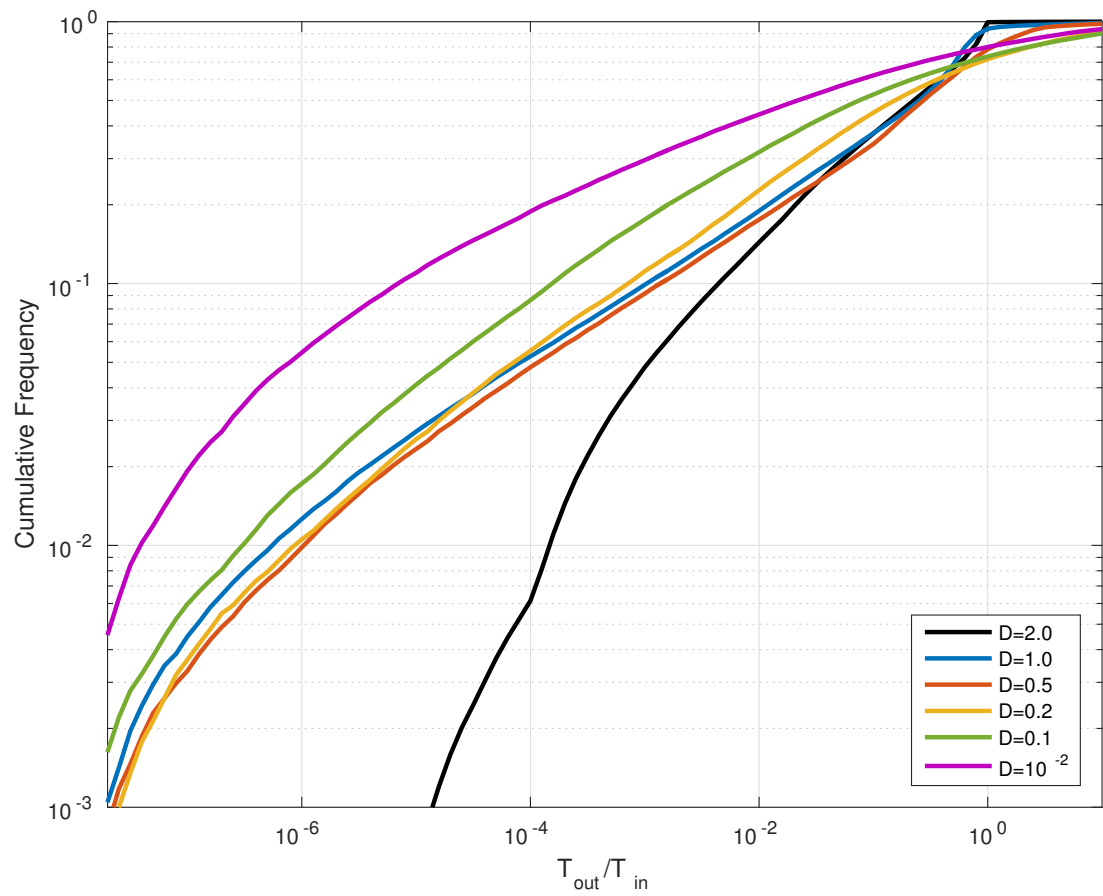


Figure 3.22: The cumulative frequency of binary merger timescales post massive black hole orbit in terms of their pre-orbit timescale for varying penetration depths. $D = 2$ (black), $D = 1$ (blue), $D = 0.5$ (red), $D = 0.2$ (yellow), $D = 0.1$ (green), $D = 10^{-2}$ (magenta).

lence of compact object binaries in the Galactic centre. If these binaries do exist in large numbers within the black hole's sphere of influence they can expect to interact with the massive black hole at a rate proportional to that of regular stars, and with the same distribution of penetration depths. These compact objects are able to penetrate deeper within the tidal radius than normal stars as the Roche limit for neutron stars is far smaller than that of main sequence stars. A stellar mass BH binary should be well described as two point particles. However, if the periapsis is close to the event horizon scale R_g of the central MBH, the Newtonian formulation would break down. Relativistic effects are negligible for $D \gg (m/M)^{1/3} R_g/a \sim 8 \times 10^{-4} (a/1\text{AU})^{-1} (m/4M_\odot)^{1/3} (M/4 \times 10^6 M_\odot)^{2/3}$.

Although these results are promising at deep penetration depths the periapsis of the binary's orbit may approach the event horizon scale of the black hole, and close to this scale general relativistic effects could become significant (Fernández and Kobayashi, 2019). As the restricted 3-body approximation does not consider any general relativistic effects it may not be reliable at these depths. Fortunately the depth at which general relativistic effects become significant is very small:

$$D_{GR} = 0.005 \left(\frac{a}{0.1\text{AU}} \right)^{-1} \left(\frac{m}{2m_\odot} \right)^{\frac{1}{3}} \left(\frac{M}{4 \times 10^6 m_\odot} \right)^{\frac{2}{3}}. \quad (3.6)$$

Assuming a linear distribution in penetration depth only a small proportion of binaries will have orbits with penetration depths smaller than this unless the super-massive black hole is significantly more massive ($10^9 M_\odot$) than our own Sgr A*.

Chapter 4

Conclusions and Discussion

Within this thesis I have presented the results of extensive investigation into the dynamics of binary tidal disruption in order to better understand the parameters that cause a binary to survive or be disrupted by a close encounter and the range of post encounter parameters for the application to hyper-velocity stars.

I have discussed how binary tidal disruption depends on the inclination, orientation, and penetration depth. Due to the large mass ratio I was able to use the restricted three-body approximation to explore this parameter space efficiently. For circular binaries, we have show that, with random orientations, about 12% of them survive even if they approach the massive BH very closely: $D \ll 1$. In these deep penetrations the binary members separate as they approach periapsis even in the surviving cases but then approach each other after the periapsis passage. The dependence on the orientation of the binary changes from shallow to deep penetrations. In shallow penetrations the disruption probability is a decreasing function of inclination from prograde orbits and as D approaches the maximal value that a binary can be disrupted at (~ 2.2) disruption is only found in exactly prograde orbits. In the deep penetrations almost all binaries are disrupted when oriented directly towards or away from the black hole ($\theta \lesssim 0.15\pi$ or $\theta \gtrsim 0.85\pi$). This area of total disruption may be connected to the orientation dependence on the semi-major axis of surviving binaries found by Addison et al. (2015) where binaries with these orientations survive with wider separations than they began

with. The energy of ejected binaries is only weakly dependent on orientation in deep penetrations, with the energy for $\theta = \pi/2$ being higher by a factor of 1.4 – 1.7 than that for $\theta = 0$. In shallow penetrations the energy follows a similar function to that of the disruption probability with orientations with low disruption probability having a low average ejection energy.

In prograde binaries the disruption rate is insensitive to the eccentricity of binaries but with eccentric binaries able to be disrupted at shallow penetrations and the position of the peak disruption rate shifted to larger D values. Retrograde binary orbits with $D < 0.2$ have a disruption rate that is weakly dependent on eccentricity. Outside of this range more eccentric binaries can be disrupted well outside of the penetration depth range typical of retrograde binaries. This can be partially explained by an effectively wider binary separation for more eccentric binaries but that alone is insufficient to fully explain this behavior. However, the energy is not a monotonic function of the eccentricity, and it peaks at $e \sim 0.35$. My simulations of eccentric binaries are limited to co-planar binaries due to the increased parameter space introduced by the orientation of the eccentricity vector. To fully explore the effect of eccentricity on binaries future work would need to sample over all binary orientations.

A factor that is not considered in this work is that of the radius of the binary members. In treating stars as point particles I do not explore the potential for stellar disruption. For $D \ll 1$, the pericentre distance to the central MBH becomes comparable to the tidal radius of the individual stars that compose the binary system. If the binary members are solar-type stars with initial separation $a \sim 1$ AU, they are tidally disrupted for $D \lesssim 5 \times 10^{-3}$. Such double tidal disruption events have been discussed by Mandel and Levin (2015). To achieve a deeper penetration without the disruption of the binary members, binaries need to have a wide initial separation, or they should consist of compact objects.

I have explored tidal disruption in the context of compact binary mergers. By considering the case of surviving binaries I have found that close encounters between massive black holes and compact binaries can accelerate their merger by several orders of magnitude. At small penetration depths, where the periapsis of the binary orbit

is on the event horizon scale, the restricted 3-body approximation may not be suitable for describing the orbits of binaries around a black hole. The depth where this occurs however is very small and the number of binaries orbiting that close to a massive black hole is not statistically significant. It is still unclear to what extent this method of accelerating mergers will affect the predicted merger rate. The distribution of compact object binaries in the centre of galaxies is still unknown but based on estimates of encounter rates from Fernández and Kobayashi (2019) there is an expected merger rate due to tidal encounter of $0.6 \text{Gpc}^{-3} \text{yr}^{-1}$. Based on this estimate post tidal encounter binaries are unlikely to be the dominant contributor to the gravitational wave detection rate, which is expected to be $12 - 213 \text{Gpc}^{-3} \text{yr}^{-1}$ (Abbott et al., 2017b).

Another possible implication of our results is the study of irregular satellites around giant planets, which are observed to follow distant, inclined, and often eccentric and retrograde orbit. One of the leading mechanisms to produce such satellites is the three-body tidal encounter between planets and planetesimal binaries (Agnor and Hamilton, 2006; Kobayashi et al., 2012).

I do not account for the possibility of stellar collisions during the tidal encounter. However, such collisions and the resultant mergers could have interesting consequences (Bradnick et al., 2017). The collision rate can be approximated in shallow binaries by using the parabolic restricted three-body approximation. Although the energy and disruption probability are accurately evaluated in this approximation, the separations of the binary members are overestimated for a short period around the peripasis passage $|t| < (m/M)^{1/3} \sqrt{a^3/Gm}$ for $D < (m/M)^{1/3}$ (Sari et al., 2010).

If the mass ratio M/m is not very large, we might underestimate the collision rate in deep penetrations. However, by selecting close binaries with $a = 10R_{\odot}$ the limiting penetration depth comes from the tidal radius of the individual stars. For such binaries, I have evaluated the collision probability during a binary's orbit about the black hole as a function of D averaged over phase and orientation. If the minimum separation of binary members becomes less than two stellar radii during the evolution (or equivalently if it becomes less than $1/5$ of the initial separation), we regard it as a collision case. The collision probability at the deepest possible penetration for $1M_{\odot}$ main sequence

stars ($D = 0.126$) is 4%, and slightly increases for shallow encounters. It peaks around $D = 1.6$ at a value of $\sim 14\%$. Even if collisions are taken into account, the disruption probability is very similar as the majority of collision cases occur in binaries that would have survived their orbit otherwise if treated as point particles. Compared to the point particle results, the fractional difference $\Delta P_{dis}/P_{dis}$ is a few percent for $D < 0.126$, and it peaks around $D = 1$ with $\Delta P_{dis}/P_{dis} \sim 5\%$. $\Delta P_{survive}/P_{survive}$ is about 45% for $D < 3 \times 10^{-2}$ (i.e. for deep penetrators, the surviving probability becomes about half of the point particle value). $\Delta P_{survive}/P_{survive}$ gradually decreases for larger D and it is about 20% for $D \sim 1$.

Bibliography

Abbott, B. P., Abbott, R., Abbott, T. D., Abernathy, M. R., Acernese, F., Ackley, K., Adams, C., Adams, T., Addesso, P., Adhikari, R. X., and et al. (2016a). GW151226: Observation of Gravitational Waves from a 22-Solar-Mass Binary Black Hole Coalescence. *Physical Review Letters*, 116(24):241103.

Abbott, B. P., Abbott, R., Abbott, T. D., Abernathy, M. R., Acernese, F., Ackley, K., Adams, C., Adams, T., Addesso, P., Adhikari, R. X., and et al. (2016b). Observation of Gravitational Waves from a Binary Black Hole Merger. *Physical Review Letters*, 116(6):061102.

Abbott, B. P., Abbott, R., Abbott, T. D., Acernese, F., Ackley, K., Adams, C., Adams, T., Addesso, P., Adhikari, R. X., Adya, V. B., and et al. (2017a). GW170104: Observation of a 50-Solar-Mass Binary Black Hole Coalescence at Redshift 0.2. *Physical Review Letters*, 118(22):221101.

Abbott, B. P., Abbott, R., Abbott, T. D., Acernese, F., Ackley, K., Adams, C., Adams, T., Addesso, P., Adhikari, R. X., Adya, V. B., and et al. (2017b). GW170608: Observation of a 19 Solar-mass Binary Black Hole Coalescence. *ApJL*, 851:L35.

Abbott, B. P., Abbott, R., Abbott, T. D., Acernese, F., Ackley, K., Adams, C., Adams, T., Addesso, P., Adhikari, R. X., Adya, V. B., and et al. (2017c). GW170814: A Three-Detector Observation of Gravitational Waves from a Binary Black Hole Coalescence. *Physical Review Letters*, 119(14):141101.

Abbott, B. P., Abbott, R., Abbott, T. D., Acernese, F., Ackley, K., Adams, C., Adams, T., Addesso, P., Adhikari, R. X., Adya, V. B., and et al. (2017d). GW170817:

- Observation of Gravitational Waves from a Binary Neutron Star Inspiral. *Physical Review Letters*, 119(16):161101.
- Addison, E., Laguna, P., and Larson, S. (2015). Busting Up Binaries: Encounters Between Compact Binaries and a Supermassive Black Hole. *ArXiv e-prints*.
- Agnor, C. B. and Hamilton, D. P. (2006). Neptune's capture of its moon Triton in a binary-planet gravitational encounter. *Nature*, 441:192–194.
- Alexander, T. (2017). Stellar Dynamics and Stellar Phenomena Near a Massive Black Hole. *ARA&A*, 55:17–57.
- Balick, B. and Brown, R. L. (1974). Intense sub-arcsecond structure in the galactic center. *ApJ*, 194:265–270.
- Bartko, H., Martins, F., Fritz, T. K., Genzel, R., Levin, Y., Perets, H. B., Paumard, T., Nayakshin, S., Gerhard, O., Alexander, T., Dodds-Eden, K., Eisenhauer, F., Gillessen, S., Mascetti, L., Ott, T., Perrin, G., Pfuhl, O., Reid, M. J., Rouan, D., Sternberg, A., and Trippe, S. (2009). Evidence for Warped Disks of Young Stars in the Galactic Center. *ApJ*, 697:1741–1763.
- Bradnick, B., Mandel, I., and Levin, Y. (2017). Stellar binaries in galactic nuclei: tidally stimulated mergers followed by tidal disruptions. *MNRAS*, 469:2042–2048.
- Bromley, B. C., Kenyon, S. J., Geller, M. J., Barcikowski, E., Brown, W. R., and Kurtz, M. J. (2006). Hypervelocity Stars: Predicting the Spectrum of Ejection Velocities. *ApJ*, 653:1194–1202.
- Brown, H., Kobayashi, S., Rossi, E. M., and Sari, R. (2018a). Tidal disruption of inclined or eccentric binaries by massive black holes. *MNRAS*, 477:5682–5691.
- Brown, R. L. (1982). Precessing jets in Sagittarius A - Gas dynamics in the central parsec of the galaxy. *ApJ*, 262:110–119.
- Brown, W. R., Anderson, J., Gnedin, O. Y., Bond, H. E., Geller, M. J., Kenyon, S. J., and Livio, M. (2010). A Galactic Origin for HE 0437-5439, The Hypervelocity Star Near the Large Magellanic Cloud. *ApJL*, 719:L23–L27.

- Brown, W. R., Geller, M. J., and Kenyon, S. J. (2009). MMT Hypervelocity Star Survey. *ApJ*, 690:1639–1647.
- Brown, W. R., Geller, M. J., and Kenyon, S. J. (2012). MMT Hypervelocity Star Survey. II. Five New Unbound Stars. *ApJ*, 751:55.
- Brown, W. R., Geller, M. J., and Kenyon, S. J. (2014). MMT Hypervelocity Star Survey. III. The Complete Survey. *ApJ*, 787:89.
- Brown, W. R., Geller, M. J., Kenyon, S. J., and Kurtz, M. J. (2005). Discovery of an Unbound Hypervelocity Star in the Milky Way Halo. *ApJL*, 622:L33–L36.
- Brown, W. R., Geller, M. J., Kenyon, S. J., and Kurtz, M. J. (2006a). A Successful Targeted Search for Hypervelocity Stars. *ApJL*, 640:L35–L38.
- Brown, W. R., Geller, M. J., Kenyon, S. J., and Kurtz, M. J. (2006b). Hypervelocity Stars. I. The Spectroscopic Survey. *ApJ*, 647:303–311.
- Brown, W. R., Geller, M. J., Kenyon, S. J., Kurtz, M. J., and Bromley, B. C. (2007a). Hypervelocity Stars. II. The Bound Population. *ApJ*, 660:311–318.
- Brown, W. R., Geller, M. J., Kenyon, S. J., Kurtz, M. J., and Bromley, B. C. (2007b). Hypervelocity Stars. III. The Space Density and Ejection History of Main-Sequence Stars from the Galactic Center. *ApJ*, 671:1708–1716.
- Brown, W. R., Lattanzi, M. G., Kenyon, S. J., and Geller, M. J. (2018b). Gaia and the Galactic Center Origin of Hypervelocity Stars. *ApJ*, 866:39.
- Chatterjee, S., Rasio, F. A., Sills, A., and Glebbeek, E. (2013). Stellar Collisions and Blue Straggler Stars in Dense Globular Clusters. In *American Astronomical Society Meeting Abstracts*, volume 222 of *American Astronomical Society Meeting Abstracts*, page 403.01.
- Deserno, M. (2004). How to generate equidistributed points on the surface of a sphere.
- Duquennoy, A. and Mayor, M. (1991). Multiplicity among solar-type stars in the solar neighbourhood. II - Distribution of the orbital elements in an unbiased sample. *A&A*, 248:485–524.

- Edelmann, H., Napiwotzki, R., Heber, U., Christlieb, N., and Reimers, D. (2005). HE 0437-5439: An Unbound Hypervelocity Main-Sequence B-Type Star. *ApJL*, 634:L181–L184.
- Eisenhauer, F., Genzel, R., Alexander, T., Abuter, R., Paumard, T., Ott, T., Gilbert, A., Gillessen, S., Horrobin, M., Trippe, S., Bonnet, H., Dumas, C., Hubin, N., Kaufer, A., Kissler-Patig, M., Monnet, G., Ströbele, S., Szeifert, T., Eckart, A., Schödel, R., and Zucker, S. (2005). SINFONI in the Galactic Center: Young Stars and Infrared Flares in the Central Light-Month. *ApJ*, 628:246–259.
- Fernàndez, J. J. and Kobayashi, S. (2019). Black Hole Mergers Induced by Tidal Encounters with a Galactic Centre Black Hole. *Monthly Notices of the Royal Astronomical Society*.
- Geier, S., Fürst, F., Ziegerer, E., Kupfer, T., Heber, U., Irrgang, A., Wang, B., Liu, Z., Han, Z., Sesar, B., Levitan, D., Kotak, R., Magnier, E., Smith, K., Burgett, W. S., Chambers, K., Flewelling, H., Kaiser, N., Wainscoat, R., and Waters, C. (2015). The fastest unbound star in our Galaxy ejected by a thermonuclear supernova. *Science*, 347:1126–1128.
- Genzel, R., Eisenhauer, F., and Gillessen, S. (2010). The Galactic Center massive black hole and nuclear star cluster. *Reviews of Modern Physics*, 82:3121–3195.
- Ghez, A. M., Klein, B. L., Morris, M., and Becklin, E. E. (1998). High Proper-Motion Stars in the Vicinity of Sagittarius A*: Evidence for a Supermassive Black Hole at the Center of Our Galaxy. *ApJ*, 509:678–686.
- Ghez, A. M., Salim, S., Weinberg, N. N., Lu, J. R., Do, T., Dunn, J. K., Matthews, K., Morris, M. R., Yelda, S., Becklin, E. E., Kremenek, T., Milosavljevic, M., and Naiman, J. (2008). Measuring Distance and Properties of the Milky Way’s Central Supermassive Black Hole with Stellar Orbits. *ApJ*, 689:1044–1062.
- Gillessen, S., Eisenhauer, F., Trippe, S., Alexander, T., Genzel, R., Martins, F., and Ott, T. (2009). Monitoring Stellar Orbits Around the Massive Black Hole in the Galactic Center. *ApJ*, 692:1075–1109.

- Ginsburg, I. and Loeb, A. (2006). The fate of former companions to hypervelocity stars originating at the Galactic Centre. *MNRAS*, 368:221–225.
- Gnedin, O. Y., Brown, W. R., Geller, M. J., and Kenyon, S. J. (2010). The Mass Profile of the Galaxy to 80 kpc. *ApJL*, 720:L108–L112.
- Gould, A. and Quillen, A. C. (2003). Sagittarius A* Companion S0-2: A Probe of Very High Mass Star Formation. *ApJ*, 592:935–940.
- Gualandris, A., Portegies Zwart, S., and Sipior, M. S. (2005). Three-body encounters in the Galactic Centre: the origin of the hypervelocity star SDSS J090745.0+024507. *MNRAS*, 363:223–228.
- Habibi, M., Gillessen, S., Martins, F., Eisenhauer, F., Plewa, P. M., Pfuhl, O., George, E., Dexter, J., Waisberg, I., Ott, T., von Fellenberg, S., Bauböck, M., Jimenez-Rosales, A., and Genzel, R. (2017). Twelve Years of Spectroscopic Monitoring in the Galactic Center: The Closest Look at S-stars near the Black Hole. *ApJ*, 847:120.
- Heggie, D. C. and Rasio, F. A. (1996). The Effect of Encounters on the Eccentricity of Binaries in Clusters. *MNRAS*, 282:1064–1084.
- Hills, J. G. (1975). Possible power source of Seyfert galaxies and QSOs. *Nature*, 254:295–298.
- Hills, J. G. (1988). Hyper-velocity and tidal stars from binaries disrupted by a massive Galactic black hole. *Nature*, 331:687–689.
- Hills, J. G. (1991). Computer simulations of encounters between massive black holes and binaries. *AJ*, 102:704–715.
- Hirsch, H. A., Heber, U., O’Toole, S. J., and Bresolin, F. (2005). US 708 - an unbound hyper-velocity subluminescent O star. *A&A*, 444:L61–L64.
- Huang, Y., Liu, X.-W., Zhang, H.-W., Chen, B.-Q., Xiang, M.-S., Wang, C., Yuan, H.-B., Tian, Z.-J., Li, Y.-B., and Wang, B. (2017). Discovery of Two New Hypervelocity Stars from the LAMOST Spectroscopic Surveys. *ApJL*, 847:L9.

- Irrgang, A., Wilcox, B., Tucker, E., and Schiefelbein, L. (2013). Milky Way mass models for orbit calculations. *A&A*, 549:A137.
- Kiminki, D. C. and Kobulnicky, H. A. (2012). An Updated Look at Binary Characteristics of Massive Stars in the Cygnus OB2 Association. *ApJ*, 751:4.
- Kobayashi, S., Hainick, Y., Sari, R., and Rossi, E. M. (2012). Ejection and Capture Dynamics in Restricted Three-body Encounters. *ApJ*, 748:105.
- Kozai, Y. (1962). Secular perturbations of asteroids with high inclination and eccentricity. *AJ*, 67:591.
- Laycock, S., Grindlay, J., van den Berg, M., Zhao, P., Hong, J., Koenig, X., Schlegel, E. M., and Persson, S. E. (2005). Constraining the Nature of the Galactic Center X-Ray Source Population. *ApJL*, 634:L53–L56.
- Levin, Y. and Beloborodov, A. M. (2003). Stellar Disk in the Galactic Center: A Remnant of a Dense Accretion Disk? *ApJL*, 590:L33–L36.
- Lidov, M. L. (1962). The evolution of orbits of artificial satellites of planets under the action of gravitational perturbations of external bodies. *Planet. Space Sci.*, 9:719–759.
- Lu, J. R., Ghez, A. M., Hornstein, S. D., Morris, M. R., Becklin, E. E., and Matthews, K. (2009). A Disk of Young Stars at the Galactic Center as Determined by Individual Stellar Orbits. *ApJ*, 690:1463–1487.
- Lu, Y., Zhang, F., and Yu, Q. (2010). On The Spatial Distribution and the Origin of Hypervelocity Stars. *ApJ*, 709:1356–1361.
- Lynden-Bell, D. (1969). Galactic Nuclei as Collapsed Old Quasars. *Nature*, 223:690–694.
- Lynden-Bell, D. and Rees, M. J. (1971). On quasars, dust and the galactic centre. *MNRAS*, 152:461.

- Mandel, I. and Levin, Y. (2015). Double Tidal Disruptions in Galactic Nuclei. *ApJL*, 805:L4.
- Matthews, T. A. and Sandage, A. R. (1963). Optical Identification of 3C 48, 3C 196, and 3C 286 with Stellar Objects. *ApJ*, 138:30.
- Miller, M. C., Freitag, M., Hamilton, D. P., and Lauburg, V. M. (2005). Binary Encounters with Supermassive Black Holes: Zero-Eccentricity LISA Events. *ApJL*, 631:L117–L120.
- Muno, M. P., Pfahl, E., Baganoff, F. K., Brandt, W. N., Ghez, A., Lu, J., and Morris, M. R. (2005). An Overabundance of Transient X-Ray Binaries within 1 Parsec of the Galactic Center. *ApJL*, 622:L113–L116.
- Naoz, S. (2016). The Eccentric Kozai-Lidov Effect and Its Applications. *ARA&A*, 54:441–489.
- Paumard, T., Genzel, R., Martins, F., Nayakshin, S., Beloborodov, A. M., Levin, Y., Trippe, S., Eisenhauer, F., Ott, T., Gillessen, S., Abuter, R., Cuadra, J., Alexander, T., and Sternberg, A. (2006). The Two Young Star Disks in the Central Parsec of the Galaxy: Properties, Dynamics, and Formation. *ApJ*, 643:1011–1035.
- Perets, H. B., Gualandris, A., Kupi, G., Merritt, D., and Alexander, T. (2009). Dynamical Evolution of the Young Stars in the Galactic Center: N-body Simulations of the S-Stars. *ApJ*, 702:884–889.
- Peters, P. C. (1964). Gravitational radiation and the motion of two point masses. *Phys. Rev.*, 136:B1224–B1232.
- Rees, M. J. (1988). Tidal disruption of stars by black holes of 10 to the 6th-10 to the 8th solar masses in nearby galaxies. *Nature*, 333:523–528.
- Rossi, E. M., Kobayashi, S., and Sari, R. (2014). The Velocity Distribution of Hypervelocity Stars. *ApJ*, 795:125.

- Rossi, E. M., Marchetti, T., Cacciato, M., Kuiack, M., and Sari, R. (2017). Joint constraints on the Galactic dark matter halo and Galactic Centre from hypervelocity stars. *MNRAS*, 467:1844–1856.
- Sari, R., Kobayashi, S., and Rossi, E. M. (2010). Hypervelocity Stars and the Restricted Parabolic Three-Body Problem. *ApJ*, 708:605–614.
- Schmidt, M. (1963). 3C 273 : A Star-Like Object with Large Red-Shift. *Nature*, 197:1040.
- Schödel, R., Ott, T., Genzel, R., Eckart, A., Mouawad, N., and Alexander, T. (2003). Stellar Dynamics in the Central Arcsecond of Our Galaxy. *ApJ*, 596:1015–1034.
- Schödel, R., Ott, T., Genzel, R., Hofmann, R., Lehnert, M., Eckart, A., Mouawad, N., Alexander, T., Reid, M. J., Lenzen, R., Hartung, M., Lacombe, F., Rouan, D., Gendron, E., Rousset, G., Lagrange, A.-M., Brandner, W., Ageorges, N., Lidman, C., Moorwood, A. F. M., Spyromilio, J., Hubin, N., and Menten, K. M. (2002). A star in a 15.2-year orbit around the supermassive black hole at the centre of the Milky Way. *Nature*, 419:694–696.
- Sesana, A., Haardt, F., and Madau, P. (2007). Hypervelocity stars and the environment of Sgr A*. *MNRAS*, 379:L45–L49.
- Šubr, L. and Haas, J. (2016). The Properties of Hypervelocity Stars and S-stars Originating from an Eccentric Disk around a Supermassive Black Hole. *ApJ*, 828:1.
- Weissbein, A. and Sari, R. (2017). How empty is an empty loss cone? *MNRAS*, 468:1760–1768.
- Yu, Q. and Tremaine, S. (2003). Ejection of Hypervelocity Stars by the (Binary) Black Hole in the Galactic Center. *ApJ*, 599:1129–1138.
- Zhang, F., Lu, Y., and Yu, Q. (2013). The Galactic Center S-stars and the Hypervelocity Stars in the Galactic Halo: Two Faces of the Tidal Breakup of Stellar Binaries by the Central Massive Black Hole? *ApJ*, 768:153.

Zheng, Z., Carlin, J. L., Beers, T. C., Deng, L., Grillmair, C. J., Guhathakurta, P., Lépine, S., Newberg, H. J., Yanny, B., Zhang, H., Liu, C., Jin, G., and Zhang, Y. (2014). The First Hypervelocity Star from the LAMOST Survey. *ApJL*, 785:L23.